Fall 2019

MICROSTUCTURAL ANALYSIS OF ADDITIVELY MANUFACTURED 308L STAINLESS STEEL PRODUCED BY PLASMA ARC WELDING

Ryan Foley

MICROSTUCTURAL ANALYSIS OF ADDITIVELY MANUFACTURED 308L STAINLESS STEEL PRODUCED BY PLASMA ARC WELDING

by

Ryan P. Foley

A thesis submitted in partial fulfillment of the
requirements for the degree of

Master of Science in Materials Science and Engineering

Montana Tech

2019

Abstract

Additive Manufacturing (AM) is a technique to produce special products by depositing layers of material in a specific pattern. Wire and arc additive manufacturing (WAAM) is an AM technique that uses welding equipment that has been modified and automated to deposit layers of welding wire. Characterization of specimens produced by WAAM method is required to optimize the process parameters. This research focuses on the microstructure characterization of 308L stainless steel samples produced by a novel WAAM technique known as Plasma Arc Weld Print 3D (PP3D). PP3D consists of multiple plasma arc torches that can deposit material in two modes of deposition: a more conventional continuous deposition seen commonly in other WAAM techniques, and a “dabber” deposition mode that places small, overlapping weld beads. The PP3D technique and specially the “dabber” mode was developed with the intention to (1) reduce directional sensitivity of deposition and (2) refine microstructure to reduce the occurrence of large columnar grain structures. Characterization of the specimens produced by these two modes was carried out by metallographic imaging, micro- and macro-indentation testing, and fractography of the fractured sample surfaces from tensile testing. Dabber mode sub-grain features were considerably finer in size while being highly variable in orientation and morphology. This is in comparison to continuous mode samples which were coarser and more consistent in orientation. At the macro level, features of the dabber mode are consistently coarser with frequent columnar grain features when compared to the continuous deposition mode. Failure surface features are highly consistent with a ductile failure mode with many dimples with few inclusions. Further refinement of the deposition conditions and settings is likely to produce results more in line with the PP3D system’s objectives.

Keywords: microstructure analysis, plasma arc welding, stainless steel, additive manufacturing

Dedication

I first wish to dedicate this work to my mother, Karen Faulkner and my father, Daniel Foley as their constant love and support gave me the ability to succeed in this endeavor and accomplish even more in the future. Additionally, I also wish to dedicate this work to Auva Speiser, for keeping me sane day-to-day with her kindness and unparalleled wit.

Acknowledgements

I first wish to thank the Army Research laboratory for providing the financial support necessary to complete this research under the Cooperative Agreement W911NF-15-0020.

I would also like to thank my committee members: Dr. Lee Richards, Dr. Bruce Madigan, and Dr. Brahmananda Pramanik for their time and technical advice. I especially wish to thank my advisor and committee chair, Dr. Sudhakar Vadiraja, for guiding me through the whole process to get this research completed in a timely and professional manner.

I would also like to graciously thank Dr. Nathan Huft for creating the samples used in this work in addition to his technical guidance and direction for processing the samples.

Additionally, I would like to thank:
Daisy Margrave for operating the scanning electron microscope for my failure analysis imaging and thank you to Gary Weiss for allowing us time on the instrument.
Additionally, I would like to thank Steven Keckler, Benjamin Suslavich and Avery Flanik for their assistance on sample preparation and microstructure analysis during the summer of 2018.

Table of Contents

List of Tables

List of Figures

List of Equations

Equation

Glossary of Terms

Term	Definition
Heat-Affected Zone (HAZ)	Non-melted metal that underwent microstructural changes during welding.
Austenite	Stable phase of iron at room temperature in stainless steels that is relatively soft and ductile and dissolves a relatively high level of carbon, increasing corrosion resistance.
Ferrite	Magnetic phase of iron that dissolves carbon poorly and has poor corrosion resistance.
Solidification Types:	A - Primary austenite structures. AF - Primary austenite with ferrite forming at the solidification grain boundaries late into solidification. FA - Primary ferrite solidification with austenite formation occurring late in solidification by a solid-state phase transformation.

1. Introduction

Additive Manufacturing (AM) is a process defined by ASTM International as, “a process of joining materials to make objects from 3D model data, usually layer-upon-layer, as opposed to subtractive manufacturing methodologies:”[1]. Additive manufacturing has roots in rapidly prototyping models using photosensitive polymer resins or laser beam melting of plastic and metal powders that would build in layers to form a finished prototype in fraction of the time and significantly reduce cost on smaller parts [2-3].

1.1. 308L Stainless Steel

The material chosen for analysis in this study was 308L stainless steel. 308L is an austenitic stainless steel that is prevalent amongst other stainless alloys (such as 316L) in welding applications due to the lower levels of carbon present naturally when compared to other grades of stainless steel. Lower levels of carbon help prevent carbide precipitation during welding as both nickel and nitrogen in the atmosphere are powerful austentizers. Additionally, welding wires typically contain lower levels of sulfur and phosphorus than conventional alloys of the same type; as both sulfur and phosphorus when segregated during cooling act as major causes of hot cracking during a weld [4-6].

1.2. Wire and Arc Additive Manufacturing

Wire and arc additive manufacturing (WAAM) is a process of metal additive manufacturing that introduces an electric arc as a heat source and wire as a feedstock. The technology has been explored for additive manufacturing since the 1990s and is gaining popularity [3]. The primary benefit of using various forms of WAAM is the process uses primarily standard, off-the-shelf products already available in the welding industry. To simplify the logistics of conversion, essentially the additions of either a robotic control systems or a

computer numerical controlled (CNC) gantry system are required to convert the welding equipment into an additive manufacturing system. Following conversion, the limitations of size are only limited by the motion system and materials that can be welded using the converted welding equipment. [3]. Figure 1 below is a representation of two different types of WAAM robotics and machinery using robotics designed for multi-axis movement welds. The system on the left is very expensive to buy outright in comparison to the right image, which is a former friction stir welder retrofitted to perform WAAM. A conversion is done either due to lack of need for the friction stir welder, or the machine has been reverse engineered to be capable of both [3].

Figure 1: (a) six-axis ABB Welding robot, (b) WAAM Deposition system retrofitted onto a friction stir welding machine [3]

WAAM-based technologies overall tend to have high rates of deposition that are well suited to high volume parts that are not geometrically complex. Several works have explored the use of WAAM-based technologies on stainless steels and especially Ti-6Al-4V alloys due to their popularity in the aerospace industry [2], [7-13].

1.2.1. Plasma Arc Welding

Plasma arc welding (PAW) is a welding process that uses electric arcs to melt a base metal and filler metal (if present) to fuse parts together, otherwise known as coalescence. PAW uses a non-consumable tungsten electrode to produce the arcs while an orifice in the nozzle of the welder can converge inert gases and constrict the arc, providing higher power input control, higher heat content, improvements in arc stability, ability to provide deeper weld penetration, and higher weld speeds. Specimens investigated for this research were produced using PAW due to the balance of power density, capital expense, and ability to aim the constricted areas of the arc [14-15].

2. Background

2.1. Plasma Arc Weld Print 3D

Plasma Arc Weld Print 3D (PP3D) is an additive manufacturing process developed for the purposes of improving plasma arc based WAAM. The process uses three PAW torches on a CNC gantry that can operate in a continuous arc mode or in a pulsed arc mode known as the "dabber" mode. Spacing the three torches at 120º from the other torches and feeding the feed wire into the middle of the pool produced by the three torches. The objectives proposed for the development of the PP3D process are to solve the following two problems [14]:

i. Eliminating travel direction sensitivity relative to the position of the torch and wire orientations during welding.
ii. Introduce a "dabber" mode welding pattern that refines microstructure compared to previous PAW methods.

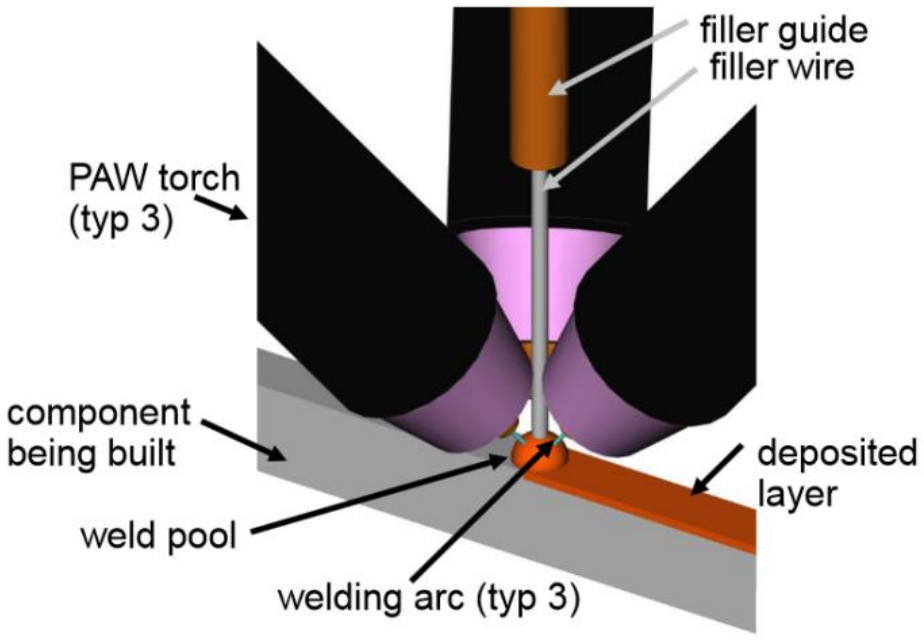

Figure 2: The PP3D Torch and Wire Assembly as Designed [14]

2.1.1. Eliminating Travel Direction Sensitivity

For WAAM, using one torch to deposit a weld bead requires choosing how to orient the torch and wire feed direction relative to travel directions. Depending on orientation, the wire feeding direction can be front-feeding, back-feeding, or side-feeding, all of which offer significant differences in the ease of welding and affect final microstructure. Typically in PAW, front feeding producing the smoothest results with the most even depositing layers. In previous PAW methods, the directional sensitivity can be reduced using complex robotics that reorient the wire and torch to be always front-feeding regardless of travel direction, but the complexity of programming often tends to be cost and developmentally prohibitive as the software is not well equipped to handle the maneuvers when compared to 3-axis systems [3], [14], [16]. Figure 3 below is a schematic rendition of the three types of possible wire feeding directions.

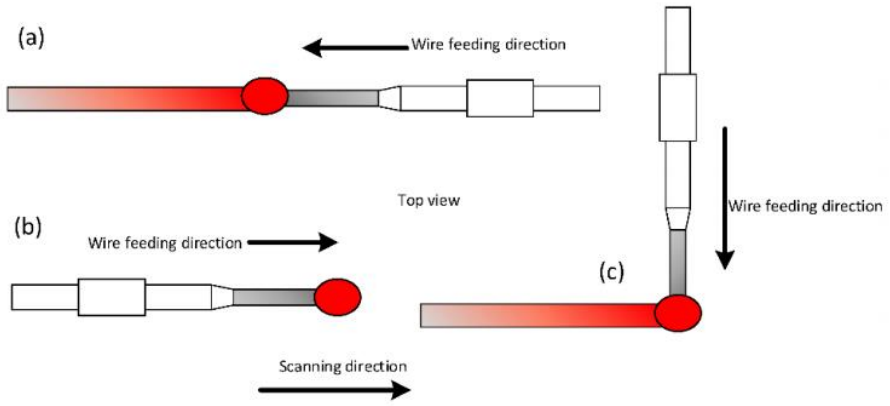

Figure 3: Wire Feeding directions where (a) is front feeding, (b) is back feeding, and (c) is side feeding [17]

The PP3D system converges the arcs of three separate PAW torches on a center point where a wire feeds directly into the center of the weld pool rather than at the edge of the pool[14]. This technique reduces directional effects and makes adjusting torch orientation unnecessary. A schematic rendition of the PP3D's arcs and wire feeding is shown below in figure 4 where the three arcs meet is in the dark blue while the slightly lighter blue is overlap of two arcs while the pale blue are areas only one arc reaches.

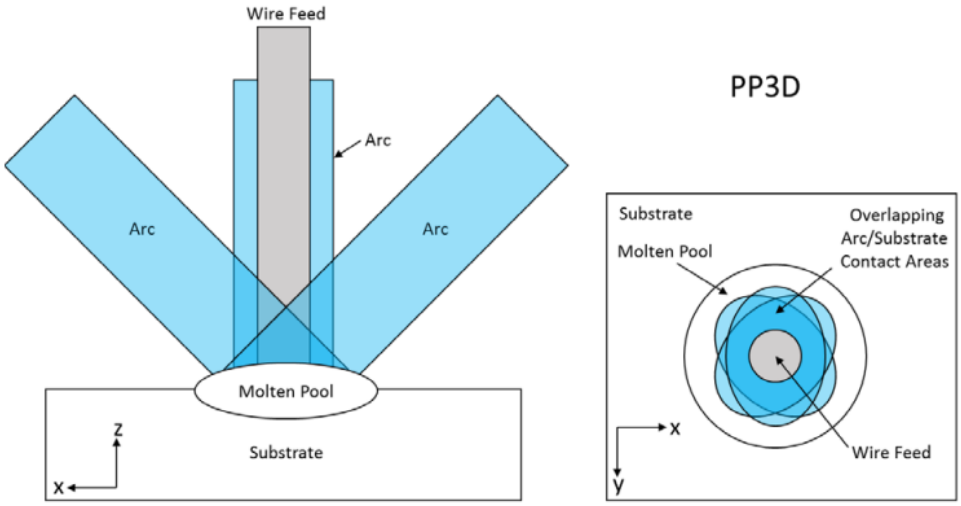

Figure 4: Schematic diagram of the PP3D system's arc and wire feed systems. The wire enters the centroid of the weld pool produced by the multiple arcs. [14]

The use of multiple arcs is not a new concept on a research or commercial scale, but use has been primarily in submerged arc welding (SAW) and no works could be found for the use of multiple arcs in regards to plasma arc welding [18]. Due to the lack of literature applicable to the PP3D system, the microstructure work presented in this product will act as a baseline for comparison for optimization attempts using the parameters used originally in the development of the PP3D system [14].

2.1.2. Dabber Mode and Grain Refinement of As-Deposited Welds

Fusion weld processes solidification is dominated by competitive grain growth and is non-conducive to equiaxed grain growth besides a relatively small amount that occurs along fusion boundaries [15]. For most applications, fine, equiaxed features are preferable as they result in higher strengths, toughness, and corrosion resistance to the weld than other features [19]. However, in WAAM, the occurrence of large, multi-layer columnar grain features in as-deposited microstructures are a vastly more common occurrence that are a result of the competitive grain growth. This can cause anisotropy in the final product [15], [20]. Additionally, some materials such as carbon steels can be refined by solid-state heat treatments such as

annealing, but austenitic stainless steels primary phases are largely controlled by conditions during and immediately following solidification. As a result, austenitic stainless steels do not undergo solid-state phase transformations to the extent of carbon steels and reduce viability of post-solidification heat treatments [20]. Figure 5 below is an illustrated example of competitive grain growth where solidified base metal begins growing in the semi-solid fusion zone of a weld pool, showing the preferred directional growth.

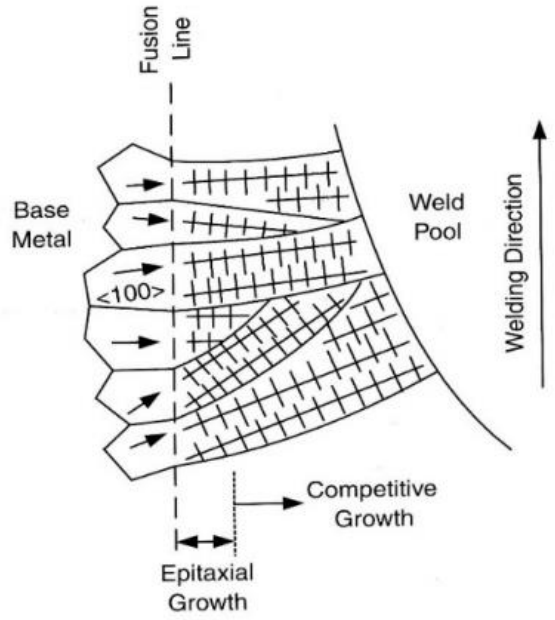

Figure 5: Illustrated Diagram of competitive grain growth towards the weld pool starting with epitaxial growth [20]**.**

To combat large, columnar grains for the PP3D technique, the proposed method is the "dabber" mode. The intended mechanism of the dabber mode is to place individual, spherical "dabs" of metal and let the dab solidify completely rather than lay down a continuous layer of wire in one layer. Each weld bead would have a curved surface and varying the microstructures. Varying the directions of growth within each bead would then theoretically limit the ability of large grains to grow between layers of weld beads, improving solidification conditions and thus

improving microstructure [14]. Figure 6 below illustrates the concept of the dabber mode with the overlapping weld beads and predicted grain growth directions.

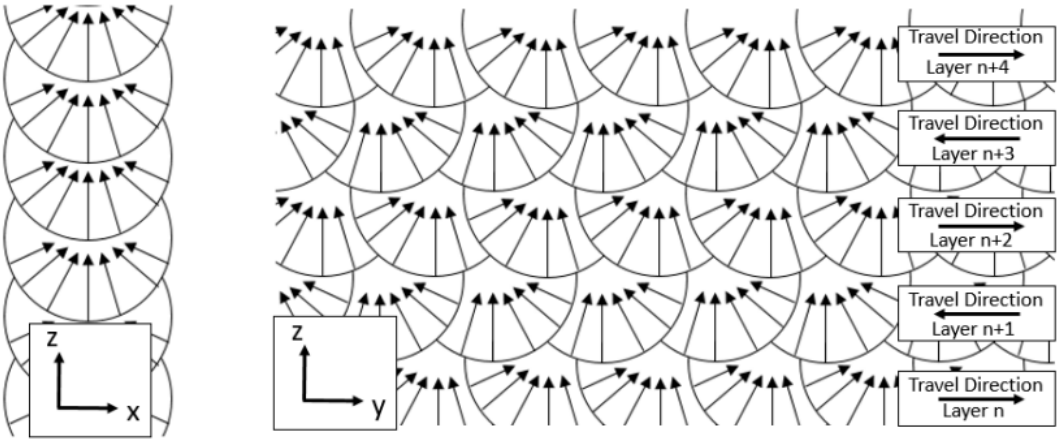

Figure 6: "Dabber" mode displaying the predicted growth directions of the weld pool microstructure features indicated by arrows [14]**.**

2.2. Metallurgy of Welds

The use of PAW techniques in an additive manufacturing setting is still an exercise of a fusion welding process. As a result, aspects of metallurgy such as studying the morphology of structures, the size of the features and grains, and the orientation in which the crystal structure grew can be applied to predict dominant microstructure and resulting mechanical properties. The state of the final morphology can change during reheating and in the case of additive manufacturing, when further layers are deposited above previous layers, melting or heating the metal enough to possibly experience solid-state phase transformations [15], [20]. The final microstructure, based on parameters explained above, in addition to any changes of material composition, parameters associated with the welding equipment, or atmospheric conditions (when applicable) during welding can have drastic effects on a welding microstructure.

Figure 7 below illustrates the general zones seen during a weld process and relates that to a simple binary component phase diagram. The first two zones are the mixed and unmixed liquid and are known as the fusion zone, which has no solid components and is above the overall

alloy's liquidus temperature. Within the fusion zone, buoyancy forces, surface tension, shear stresses, and the electromagnetic Lorentz force act on the pool, homogenizing much of the liquid besides the liquid near the partially melted zone (PMZ), where forces do not act as strongly and create an unmixed liquid zone [20]. The PMZ is an area with temperatures ranging between the liquidus and solidus temperatures where the solid grains growing in this zone act as nucleation sites during further solidification [20]. The last two zones are the heat effected zone (HAZ) and unaffected base metal. The HAZ sees temperatures that raise the temperature of the metal high enough not to reach a liquid or semi-liquid state, but the elevated temperatures can cause solid-state phase transformations seen during heat treatments such as tempering, grain recovery, or even recrystallization [20]. The unaffected base metal remains at temperatures low enough to not experience any of the phenomena experienced by the other zones and retains the previous microstructural features.

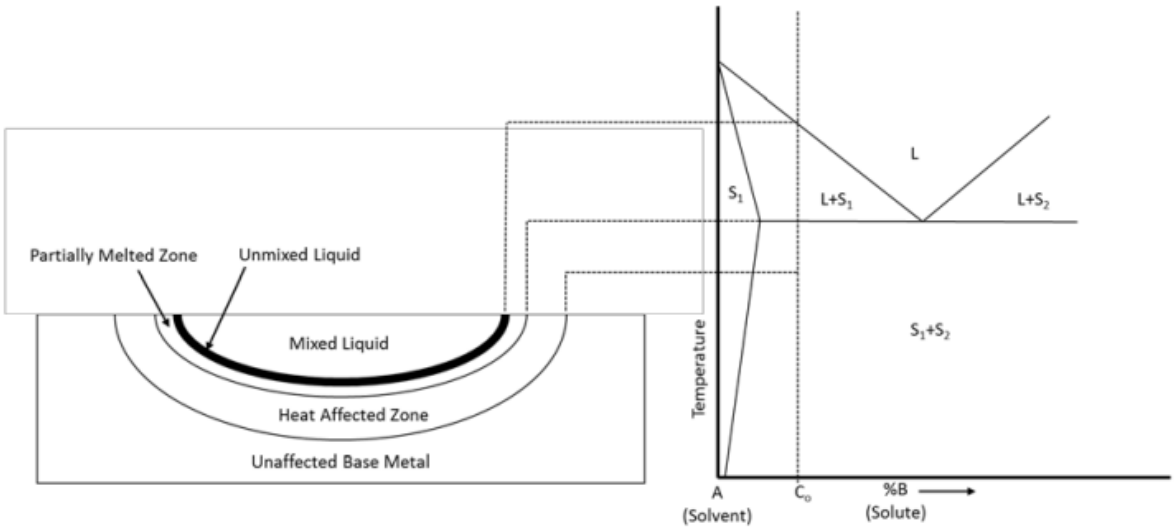

Figure 7: Diagram of the major phases within a weld pool for an alloy with composition C_o [20].

2.2.1. Equilibrium solidification

For equilibrium solidification to occur, the solidification rate must be low enough that diffusion can occur and eliminate compositional gradients within the solids and liquids. To

determine if a solidifying alloy system can achieve complete diffusion, the following two conditions must be true, otherwise complete diffusion will not occur and a level of nonequilibrium solidification will occur [20].

$$D_L t \gg l_L^2 \quad (1)$$

where D_L is the diffusion coefficient of a solute in a molten alloy, t is the time available for diffusion to occur, and l_L^2 is the initial length of the liquid.

$$D_S t \gg l_S^2 \quad (2)$$

where DL is the diffusion coefficient of a solute in a solid material, t is the time available for diffusion to occur, and l_L^2 is the initial length of the solid.

Solidification that meet the previous conditions is known as Case I solidification.

2.2.2. Nonequilibrium solidification

Solidification that does not meet the conditions for equilibrium solidification falls typically falls under one of the following two conditions [20]:

- Case II Nonequilibrium solidification – complete mixing and diffusion with negligible diffusion occurring in the solid
- Case III Nonequilibrium Solidification – limited diffusion in the liquid phase and negligible diffusion occurring in the solid.

Welding, by nature, is a multi-disciplinary field that requires a deep understanding of both kinetics and thermodynamics to develop accurate theories of final morphology [20]. Welding takes place at very high temperatures and cools at varying rates along the weld. As a result, both the gradient of temperatures in a weld pool and the cooling rate of that weld pool plays a vital role in determining the final morphology. Many of the final structures solidify at a rate that is simply too fast for proper diffusion to take place. Figure 8 below illustrates

graphically the features with respect to temperature gradients and the growth rate, or travel speed of the solid/liquid interface [20].

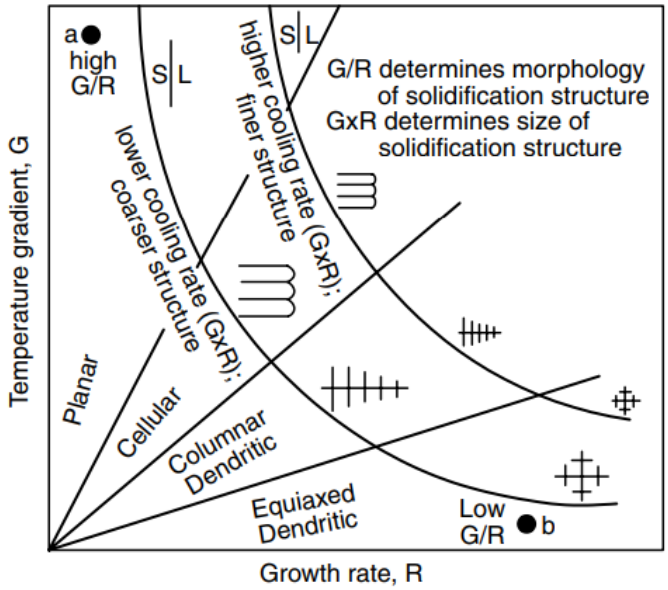

Figure 8: Illustration of the effects temperature gradient, G, and growth rate, R, have on morphology of weld solidification [20]

The planar features occur at areas of the where the temperature gradients are higher and/or the growth rates are very low so the ratio of temperature gradient to growth rate is generally very high (point a in figure 8). These areas in particular have the most time for the liquid to completely mix and diffuse, which usually occurs near the center line of a fast moving weld. This phenomena is illustrated below in figure 9 [20], [21]. Point b in figure 8 illustrates the opposite scenario where the weld pool has comparatively very low temperature gradients and a fast growth rate of the solid/liquid interface. At point b, limited to no diffusion occurs and the solidifying liquid is consequently unmixed, leading to higher concentrations of alloying elements. The equiaxed dendritic structures occur typically near the edge of a weld pool.

2.2.3. Metallurgy of Stainless Steel Welds

For the purposes of this research, while 304L stainless was used as a substrate, specimens were made using 308L stainless steel welding grade wire and will be the focus of phenomena

discussed. The topics discussed in regards to stainless steel metallurgy include the resulting morphology related to the solidification of the weld metal and effects of additive manufacturing techniques on previously deposited layers. With regards to stainless steel, the classification of the alloy is based on the balances of iron, nickel, and chrome, but overall classification is based off the chromium and nickel equivalents. The formulae to calculate both equivalents are listed below as equations 3 and 4 [22].

$$Cr_{eq} = Cr + Mo + 0.7Nb \quad (3)$$

where Cr_{eq} is the chromium equivalent and *Cr, Mo,* and *Nb* are the chromium, molybdenum, and niobium contents in weight percent.

$$Ni_{eq} = Ni + 35C + 20N + 0.25Cu \quad (4)$$

where Ni_{eq} is the nickel equivalent and *Ni, C, N,* and *Cu* are the nickel, carbon, nitrogen and copper contents in weight percent. Combining the two equations by dividing the Cr_{eq} by the Ni_{eq} gives a ratio of chromium and nickel that results in a number typically between 1.2 and 2.2. Generally, a ratio closer to 1.2 to 1.4 indicates that austenite will always be the dominant primary solidification phase. A ratio from 1.4 to 1.75 typically indicates ferrite as a dominant primary phase while a ratio above 1.75 generally indicates high levels of ferrite solidification. Austenitic stainless steels at slow solidification rates such as during in-furnace cooling or normalized (air) cooling tend to have primary austenite features with some ferritic features [23].

The solidification rate can affect this relationship significantly if solidification happens too quickly to allow proper diffusion of carbon and chromium specifically. Incomplete diffusion of these elements tends to shift the relationship towards higher ferrite formations. During welding this is a common occurrence where ferrite becomes the dominant primary phase during initial solidification. While typically useful for wrought stainless steel, the relationship defined below

as equation 5 can be combined with visual results of welded microstructure to qualitatively describes the likely solidification behaviors of stainless steels [22], [23].

$$\frac{Cr_{eq}}{Ni_{eq}} \tag{5}$$

Using equations 3, 4, and 5 above, most common forms of stainless steel have chromium contents between 15-20 wt.% and nickel contents between 10-14 wt.% various grades of stainless steels can have chromium contents ranging from 5-30 wt.% and nickel contents ranging from 2-30 wt.% with minor alloying agents such as manganese, molybdenum, carbon, and nitrogen with iron to balance [20-21]. Carbon content is kept very low in austenitic stainless steels and especially the "L" variants of the steel where for 308/308L designation stainless steels, carbon is kept to 0.08 wt.% and 0.03 wt.% at a maximum, respectively. Carbon content is kept that low as excess amounts of carbon allow for an overabundance of ferrite formation, which reduces corrosion resistance, ductility, and weldability to unusable levels [5], [6], [15], [18], [20], [24].

Figure 9 is a ternary phase diagram of stainless steels for both the liquidous surface and the solidus surface. Ternary phase diagrams for stainless steels are used to show the equilibrium cooling path. From the equilibrium conditions seen a ternary system, a pseudo-binary phase diagram can be obtained for a given range of composition of iron, chromium, and nickel, usually by setting the iron equal to the balancing weight percent for the desired stainless steel alloy composition [20].

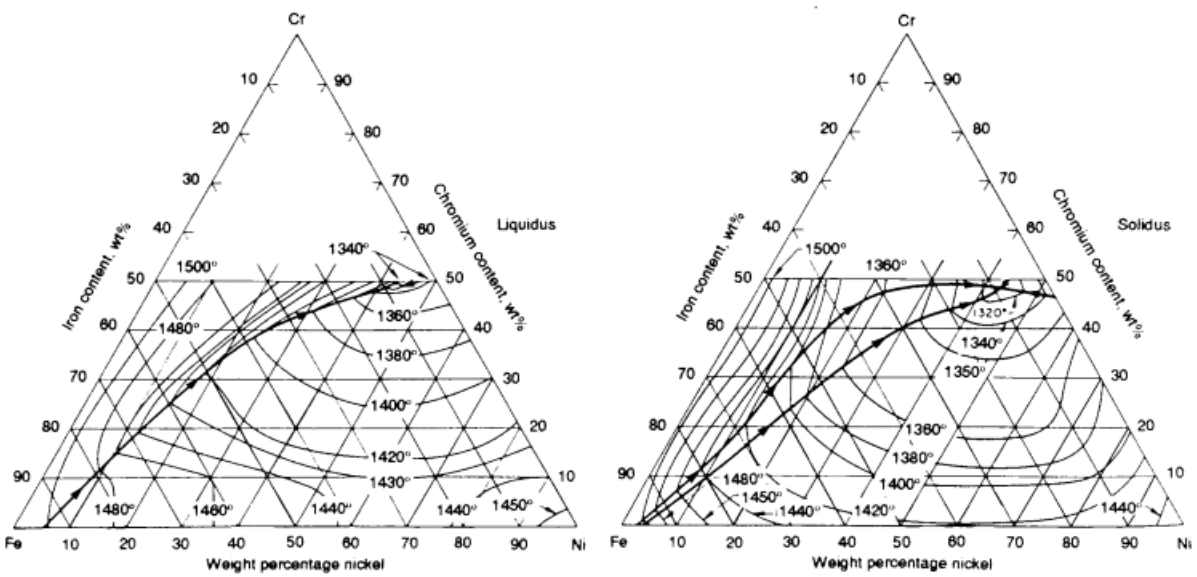

Figure 9: Fe-Cr-Ni ternary phase diagrams for the liquidous surface (a) and solidus surface (b) [20]

Figure 10 below is an example of a pseudo-binary phase diagram derived from figure 9 to relate morphology to the composition of an austenitic stainless steel for 70% iron and will serve as a guide for the discussion on the primary solidification types. The features shown correspond to a primary solidification method of either primary austenite (γ) or primary ferrite (δ). The features shown in figure 10 are examples of the as-solidified morphology [20].

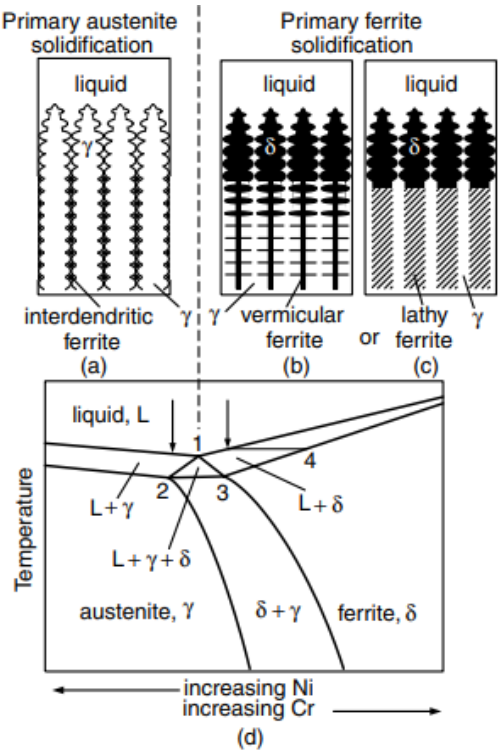

Figure 10: Schematic for a pseudo-binary phase diagram for an alloy with 70% Fe displaying final solidification microstructure in Fe-Cr-Ni Welds (shown as part (d)): interdendritic ferrite formations (a), vermicular or "skeletal" ferrite (b), lathy ferrite (c) [20]

2.2.3.1. Primary Austenite Solidification

Primary austenite solidification is a post-weld solidification type that becomes thermodynamically favored when the composition of the weld pool has a higher nickel equivalent from equation 5 and solidifies left of the triangular phase in figure 10 containing a mixture of solidified austenite and ferrite in a liquid matrix (the L+ γ+ δ phase field). When solidifying as primary austenite phases, the solidification morphology can either be Type A or type AF solidification [18], [20]. Both solidification modes are typically considered undesirable as both are more prone to solidification cracking than primary ferrite solidification modes [20], [22], [25].

2.2.3.1.1. Type A Solidification

Austenite formed during solidification is stable at room temperature, so if the composition falls far to the left of the L+ γ+ δ phase field where nickel is a more abundant alloying agent, austenite becomes the primary morphology present after solidification due to the nickel acting as a strong austenite stabilizer. The lower amounts of chromium do not cause large formations of ferrite phases to form unless the metal is heated significantly to allow possible formations of ferrite. Figure 11 below is an example of well-formed type A solidification morphology seen as cellular structures of differing shapes and sizes [22].

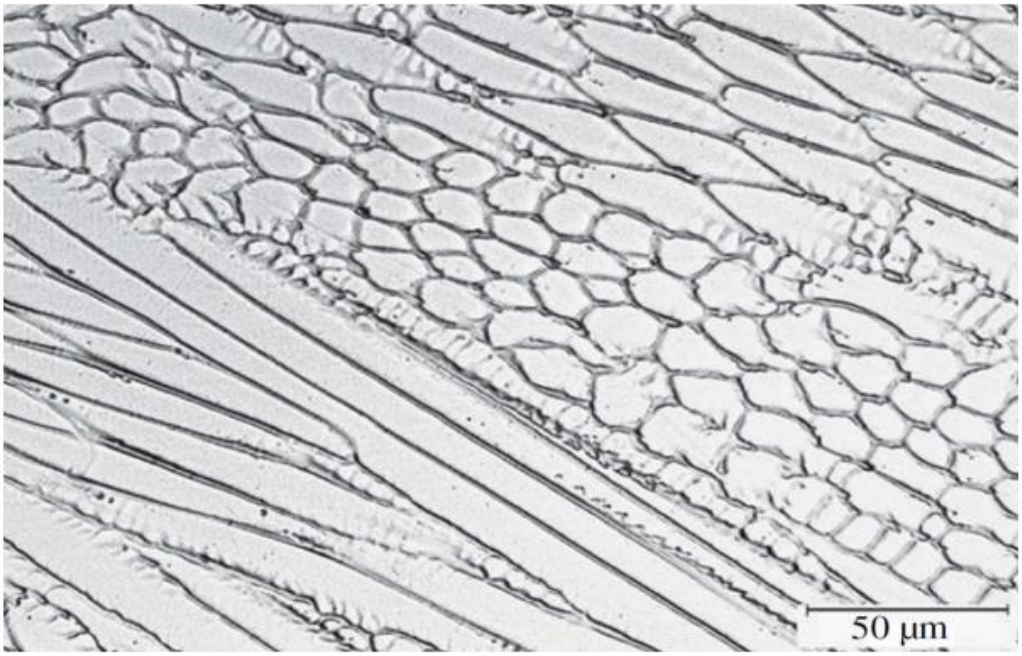

Figure 11: Prominent example of Type A solidification showing distinct cellular structures in an austenitic stainless steel [22]**.**

2.2.3.1.2. Type AF Solidification

When solidification composition falls between points 1 and 2 on figure 11, type AF is the dominant form of solidification morphology. Austenite forms first into crystal followed by ferrite forming in the solidification grain boundary (SGB) and solidification sub-grain boundaries (SSGB). As mentioned previously, austenite grains that form become stable at room temperature,

elements such as chromium that get rejected by the austenite gather in the grain and sub-grain boundaries. Chromium acts as ferrite stabilizer and thus portions of the ferrite that form with the chromium become stable to room temperature [22].

Figure 12 below is an example of type AF solidification where ferrite stabilizing agents, rejected by the stable austenite features allowed for room temperature-stable ferrite to form in the solidification sub-grain boundaries.

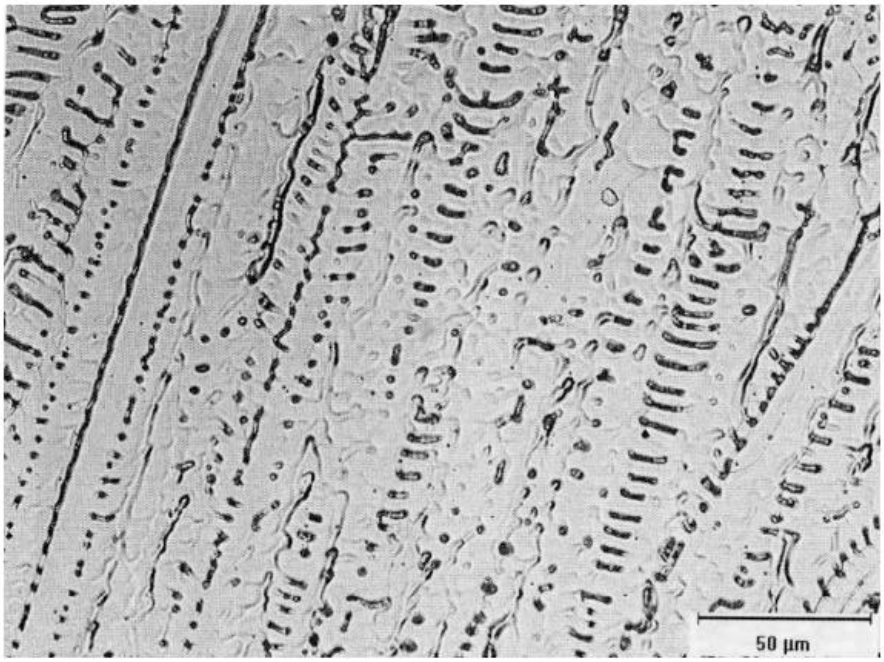

Figure 12: Type AF solidification where the light etching phase is austenitic structures and the dark phase is the formation of stable ferrite structures at the SSBGs [22]**.**

2.2.3.2. Primary Ferrite Solidification

In primary ferrite solidification, Chromium has become largely abundant causing the Cr_{eq}/Ni_{eq} composition to shift to the right of point 1 from figure 10 towards point 3, causing higher levels of ferrite stabilization. The two types of primary ferrite solidification are type FA and type F, but in austenitic stainless steel, type F is exceedingly rare [22].

2.2.3.2.1. Type FA Solidification

When the Cr_{eq}/Ni_{eq} balance falls to the between points 1 and 3 on figure 10, ferrite forms before austenite during solidification and forces austenite to the SGBs and SSGBs [22]. Further into the solidification, ferrite becomes less thermodynamically favored and austenite forms and grows, causing most of the ferrite to dissolve into the austenite via a solid-state phase transformation. Following the phase transformation, the remaining ferrite is highly enriched, leaving behind dendrite structures known as vermicular or "skeletal" dendrite or leaving behand lathy ferritic dendrites. These structures have a clear directionality from their growth direction [6], [20], [25].

Figures 13 and 14 below are examples of type FA solidification following solid-state phase transformation where ferrite enriched dendritic structures remain in the SGBs or SSGBs of an austenite matrix.

Figure 13: Type FA solidification with skeletal ferritic structures (dark etch phase) exist in an austenite matrix [22]**.**

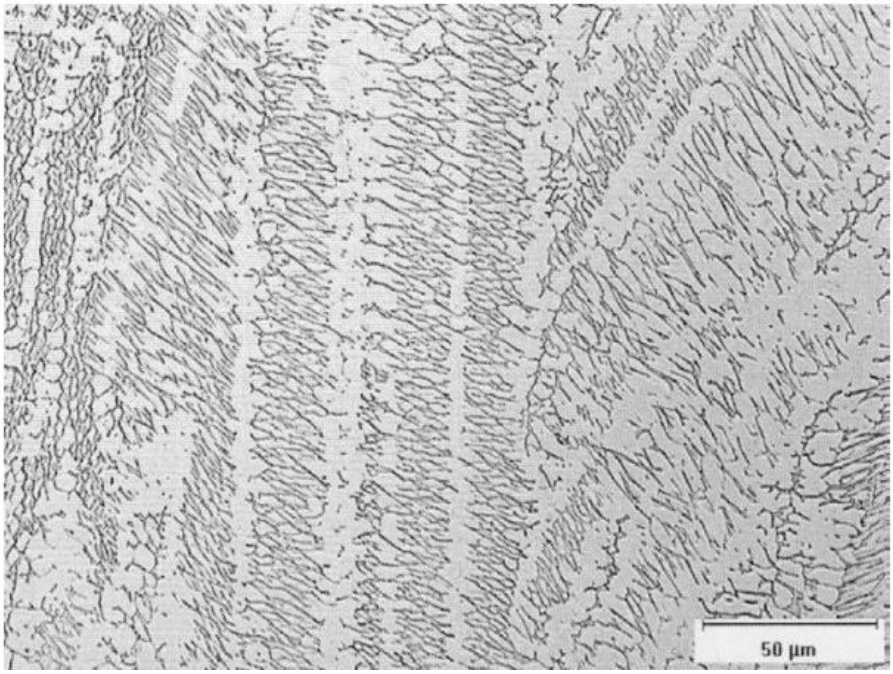

Figure 14: Type FA solidification with lathy ferritic structures (dark etch phase) exist in an austenite matrix [22].

2.2.4. Post-Solidification Phase Transformations and Phenomena Related to Reheating from Additive Manufacturing

Austenitic stainless steels, as the name suggests, typically have an overwhelmingly austenitic grain structure. From a thermodynamic view, all the grain structure would be austenite if the kinetics of solidification allowed for full diffusion. However, as previously discussed, the extremely high temperatures, variable cool rates of the weld pool, and fluctuating chemistry of the weld pool does not allow for the complete dissolution of ferrite into austenite, leaving some ferrite as previously discussed. Ferrite in small quantities does increase strength and reduces solidification cracking compared to a completely austenitic microstructure, but ferrite in any quantity reduces the overall toughness and corrosion resistance of the stainless steel by a significant amount [22].

WAAM involves welding of wire onto a substrate and layers of previously deposited material to create a finished part. During that process, some portion of the previous layer is

melted again into the weld pool while the metal below becomes a HAZ, and undergoes brief periods of solid-state phase transformations. The primary mechanism of these solid-state transformations are the further decomposition of ferrite. David [24], [26] found that more fine microstructures tend to convert ferrite to austenite upon reheating to 1000°C for various times, likely due to the shorter diffusion distances inherent with more fine microstructures.

Comparing figures 15 and 16, reheating the samples also changes microstructure features by a noticeable degree. When comparing the as-deposited microstructures seen in figure 15 to the samples reheat at 1050°C for 10 minutes seen in figure 16, the dark etched ferrite phases are less well-defined in their structure and sparser in their appearance.

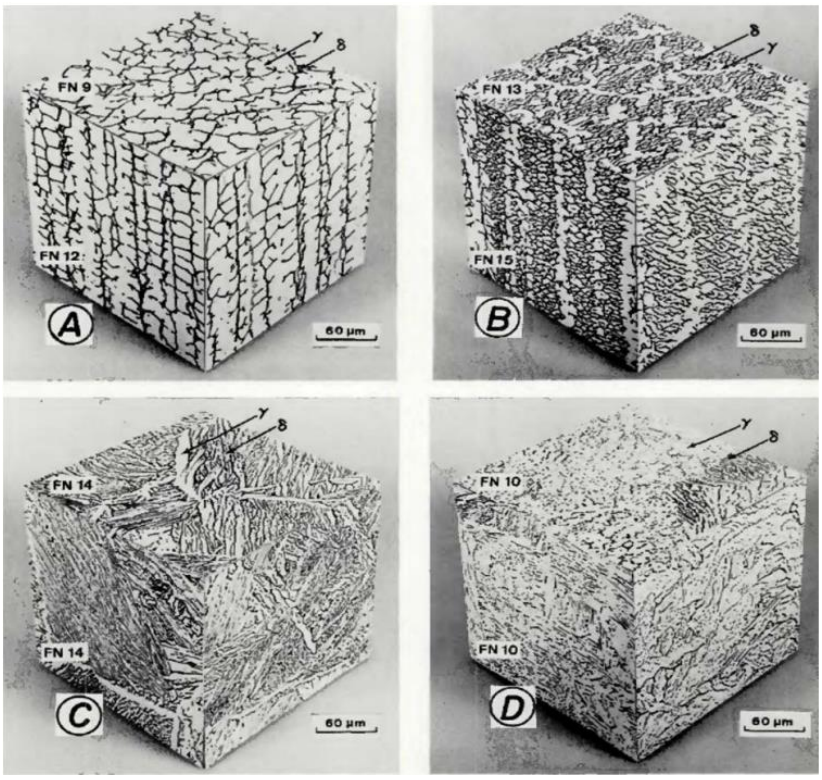

Figure 15: As-solidified morphologies of FA ferrite structures in an austenite matrix where (A) is skeletal, (B) is lathy, (C) is acicular, and (D) is globular [22]

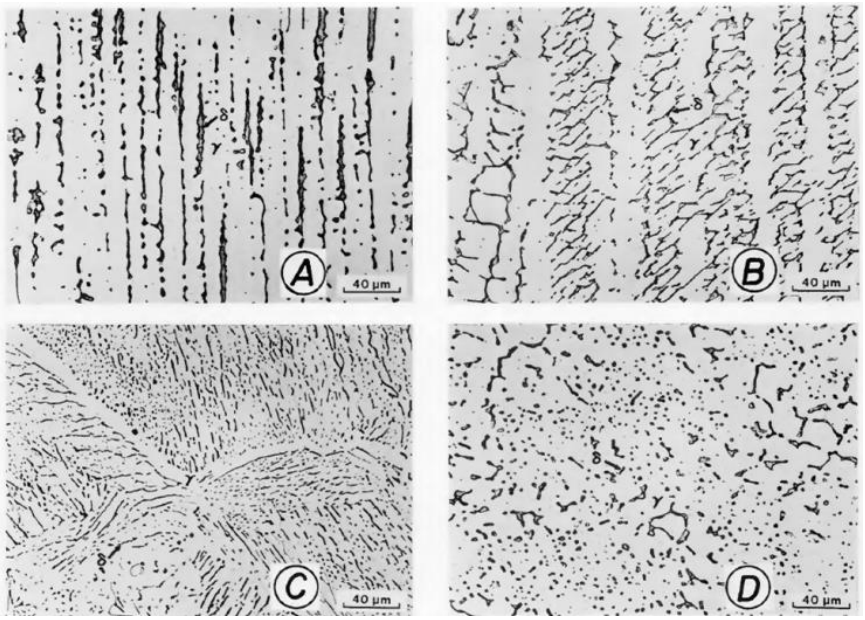

Figure 16: Reheated morphologies in 308 stainless castings after 10 minutes at 1050°C where (A) is skeletal, (B) is lathy, (C) is acicular, and (D) is globular [22]

2.3. Use of Hardness Testing

Hardness testing is the only method of mechanical testing performed on PP3D samples due to current limitations on the size of specimens produced by the PP3D system. As a direct result, the discussion of hardness testing will be without accompanying tensile results for comparison. That is not to say hardness testing cannot be useful, as hardness testing acts as an empirical indicator for tensile strength, ductility, toughness, and machinability. As part of the empirical nature, hardness testing is often used either in place of more quantitative testing or not at all. The primary benefit of using hardness testing are to settings such as quality control or in research and development where the hardness testing results can indicate if the material is meeting specified qualities quickly and potentially avoid more costly testing [26-27]. If empirical values are not met, then additional testing can be conducted to identify more specific issues with the mechanical properties.

Two types of hardness testing are reported in this work, microindentation and macroindentation. Microindentation's primary use is in reporting variance of hardness over a small distance due to either intentional or non-intentional variances of a local area and has a very small indenter with a low load (typically under 10 N). Due to the high levels of variance seen in both size and type of welding microstructures, microindentations are useful in exploring hardness changes across a welding microstructure. Macroindentation has a larger indenter and is more useful in determining bulk hardness of a larger sample [26-27]. Used in conjunction with microindentation, a more cohesive hardness profile for sections of a specimen produced by the PP3D system can be obtained to make empirical assumptions about the hardness of the welded samples.

3. Research Objectives

Metallographic analysis and failure analysis of the 308L stainless steel produced by the PP3D system was done to gain an understanding of the following:

1. Investigate 308L stainless steel microstructural features produced by PP3D in the “continuous” and “dabber” modes.
2. Examine the differences in microstructure features between the continuous and dabber modes under three levels of power input produced by the PP3D system.
3. Use fracture surface analysis and hardness data to correlate processing characteristics of dabber mode.
4. Compare the present results to microstructural features found in published works.

4. Experimental Procedure

4.1. Specimen Production

Samples were produced as to the specifications from Huft [14] with pertinent information presented in this work in relation to describing results and for use in the discussion of those results. 308L wire with a diameter of 1.14 mm was deposited on a 6.4 mm wide substrate, shown schematically below in figure 17. The intent for every sample was to deposit 25 layers of the 308L wire onto the substrate while reducing length of each layer slightly to mitigate effects of the torch starting and stopping at the end of each layer, deforming the piece.

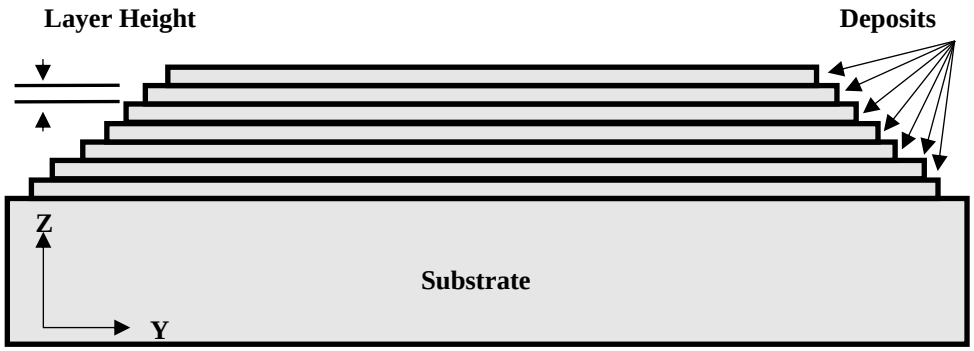

Figure 17: Schematic rendition of a sample produced by PP3D

Huft, while developing the system, wanted to explore the system's functionality at differing levels of power input pushed towards the sample by varying the background welding current until either an effective weld pool could not be formed, or issues such as surface oxidation, weld pool deformations, or "humping" in the welds occurred. Table 1 below summarizes the background welding current (in amperes) used for each parameter and the resulting gross linear heat input (in joules per millimeter). Table 1 also represents the baseline conditions of specimen creation when henceforth discussing samples produced using either a low, medium, or high-power input. Other conditions for specimen creation were kept as consistent as possible for all samples, varying conditions such as wire feed speed as needed to maintain stable welding conditions.

Table I. Background Welding Currents of Both Modes for the Three Power Inputs[14]

		Low-Power	Medium Power	High-Power
Background Weld Current (A)	Dabber Mode	10	15	20
	Continuous Mode	15	20	25
Gross Linear Heat Input (J/mm)	Dabber Mode	1570	1760	1740
	Continuous Mode	31.6	27	23.5

4.2. Cutting and Mounting Specimens

Metallography samples were cut from the completed specimens of all power inputs and deposition modes using an Allied Powercut 10 under heavy coolant and cut slowly to avoid overheating the stainless steel and releasing chromium radicals. Samples for XZ and YZ orientations were cut to around 2 cm in length to both maximize area examined per sample while minimize area lost during sectioning the samples. XY samples in contrast were cut to 1 cm or less to maximize number of individual layers seen. Figure 18 below is a representation for the orientations examined in this study using a cut specimen. The XY plane would be looking straight down from the top of figure 17, the YZ plane is the outer faces of the specimen, and the XZ plane is a cross section of the sample from the top to bottom.

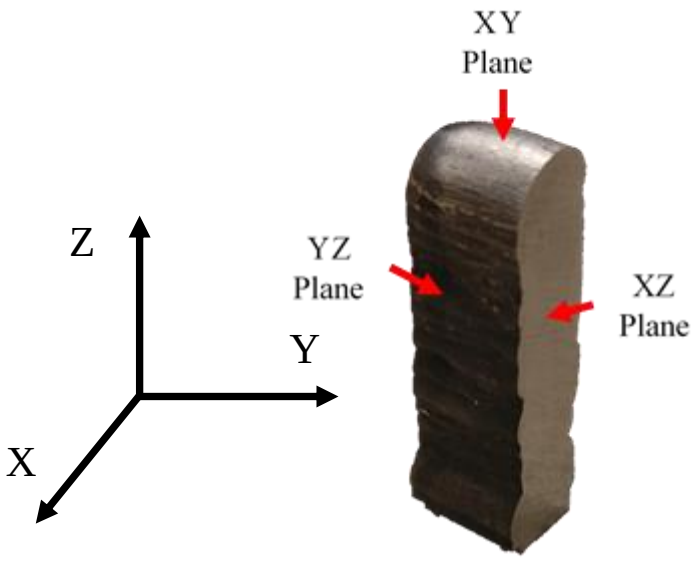

Figure 18: Diagram showing orientations examined for metallographic analysis from specimens produced in the fashion of figure 17.

Following cutting, a release agent was placed on a platform for a metallographic mounting press before placing a sample with the desired orientation face on the release agent. Bakelite phenolic resin powder was measured using the provided measuring cup to approximately three quarters of the provided measuring cup and was then poured overtop the sample. The mounting press was set to the appropriate number of samples and let run, which produced a finished puck for examination.

4.3. Polishing and Etching Specimens

Sample pucks were subjected to hand polishing on silicon carbide pads of grits 60, 120, 240, 400, and 600 with a rinse under deionized water followed by a quick dry using acetone in-between each grit. Rough polishing on each grit was done for approximately one minute with relatively hard pressure used on the polish.

Fine polishing was done on microfiber pads using 15-,5-, and1-micron alumina slurries with a rinse and dry procedure as described previously, but with the acetone in a glass beaker inside a sonication bath. Final polishing was done on a Chem pad with 0.25-micron diamond slurry with

an identical rinse and drying procedure as described above. Fine and final polishing was done with comparatively very light pressure and for only 30 to 60 seconds at most at each step. After the final polish, samples would be clear of most scratches visible to the naked eye and would have a shiny, mirror-like reflective surface.

Etching for microstructure images was accomplished using Vilella's reagent from Metlab. Vilella's reagent purchased from Metlab was mixed in the standard ratio of 1-gram picric acid, 5 mL Hydrochloric acid, and 100 mL of ethanol. The etch was performed by placing drops over the sample until the whole surface of the sample was covered (approximately 3-4 drops). The drops sat on the surface until the surface transitioned from the shiny mirror-like surface seen after polishing to a cloudy surface with larger grain features becoming visible to the naked eye (typically 30-90 seconds). Once the surface had achieved nearly equal levels of etching, the sample would be rinsed heavily under de-ionized water and placed in an acetone bath before being dried. The sample was then ready for examination under an optical microscope.

4.4. Microstructural Imaging

Following etching, the sample was placed under either a Leica DM750P with Leica DFC295 camera or a Leica DM750M with a Leica MC170 HD Camera. The samples were examined at approximately 100X, 200X, and 500X, but actual magnification was corrected for by the Leica Application Suite V4.8 software. The software correction is represented by the scale bars in the images. Approximately 40-70 plus images were taken along a large portion of the surface, photographing most of each sample.

Images were taken in a pattern of examining the right side from the top to bottom, moving the focus to the center of the sample and imaging from the bottom to the top, and finally

imaging the left side of the sample from the top to the bottom of the sample. Unless a sample area was particularly feature rich, the number of images and approximate location was kept relatively consistent for better counting or approximating the layers where features originated.

4.5. Dendrite Analysis

The Leica Application Suite V4.8 software included a feature called “Dendrite Expert” that examines the length of microstructural dendrite features and outputted an average dendrite spacing of the features measured. Analysis could have been done semi-autonomously or manually. Images in this report were measured manually as the semi-automatic mode presented instances of counts that were either significantly too high or too low to be considered within acceptable amounts of error.

Manual mode dendrite counting involved drawing lines through skeletal or lathy dendrites and entering the number of dendrites counted by the operator, repeating the process on as many separate instances of dendrites as possible. Most reports had at least 20 separate counts and an average of at least 33 counts. Dendrite Expert then generated a report on Microsoft Excel with a copy of the image that contained all the instances counted. The values reported included the total number of dendrite arms counted and added the length of all instances of dendrites to give a total arm length. The two variables were divided to generate the average secondary dendrite arm spacing of all counted features. The extremes and standard deviation were examined to provide insight to morphology size and aided in predicting mechanical properties.

4.6. Macrostructure Imaging

Macrostructure imaging underwent an identical preparation process to the microstructure samples but the polishing process ended after the 15-micron polishing step and the samples were etched using Marble’s reagent from Metlab, which was mixed in the standard ratio of 10 grams

of CuSO4, 50 mL of Hydrochloric acid, and 50 mL of water. The Marble's reagent better revealed the layer lines, weld beads, and larger grain features of the samples than Vilella's reagent, so Marble's reagent was selected. The etching process was identical to the microstructure imaging method, but the etchant was left on the sample longer until the layers/dabs became visible to the naked eye and relatively darkened.

Following etching, the sample were cleaned as described in section 3.3 above, and the sample was placed under a Leica S8APO microscope with a Leica DFC295 camera. Samples were imaged using a variable level of magnification, so scale bars were placed on all images because scale bars acted as a more accurate method of comparison of feature size rather than relative magnification.

4.7. Hardness Testing

Two types of hardness testing were performed for this research: microindentation and macro-indentation. The micro-indentation testing was performed using a Leco LM 300AT using a Vickers 10g diamond-shaped indenter. Measurements of hardness were taken by indenting the surface of the sample and measuring the diamond-shaped indication according to equation 6 below for expressing Vickers hardness in the grams-force scale.

$$HV = 1854.4 * \frac{P}{d^2} \tag{6}$$

where P is the force in grams-force, and d is the mean diagonal length of the indentation in microns.

The macroindentation was performed on XZ and YZ samples using a Tinius Olsen FH-1 series indenter and a Rockwell B scale (HRB) 100kg 1/16" ball, performing tests every few millimeters down the Z axis from the top of the sample into the base metal to maximize testing locations

4.8. Scanning Electron Microscopy

SEM imaging for the purposes of this report was performed on samples that previously underwent tensile testing in previous work. The tensile data reported was uncharacteristic of an austenitic stainless steel and had to be discarded from consideration on reporting mechanical properties in that work [14]. This work examined the failure surfaces to determine if the fracture features were like tensile failure surfaces of wrought samples of a similar alloy composition. If the samples had not displayed highly ductile fracture features seen as typical for austenitic stainless steels, then the PP3D system likely generated drastic changes in microstructure that would have caused premature failure. In the more likely case that features were typical for austenitic stainless steel, then the recommendation for future work would be to first re-examine tensile specimen creation, testing procedures using wrought samples followed by attempts at optimizing the system.

Preparation for making the samples viewable under SEM include cutting the fractured samples by carefully mounting the sample in the TechCut 10 slow cutting metallographic saw to achieve a final size of around 2 cm or less. Excess cutting fluid was then washed off the sample using reagent alcohol in an ultrasonic bath. The washed specimen was then mounted and imaged by a Tescan TIMA Scanning Electron Microscope in secondary electron mode. Additionally, energy dispersive analysis x-ray (EDAX) analysis was performed using both spot analysis on distinct features in addition to line analysis encompassing main features of each image.

5. Results

5.1. Microstructure Imaging

Images of the microstructure or micrographs are provided below for each power input level and orientation based on representative features seen across the sample.

5.1.1. Dabber Mode

Dabber mode images display feature sets that are very fine in size across all power inputs and orientations, though they displayed no strong tendencies in growth direction to favor a certain orientation. Dabber mode overall tended to favor FA type solidification grain structure features with some typical AF and type A solidification features near grain boundaries.

5.1.1.1. High Power Input

The high-power input samples overall had the second finest average dendrite feature sizes of the dabber power inputs, producing fine, skeletal and lathy dendrite features throughout the sample.

5.1.1.1.1. XZ Orientation

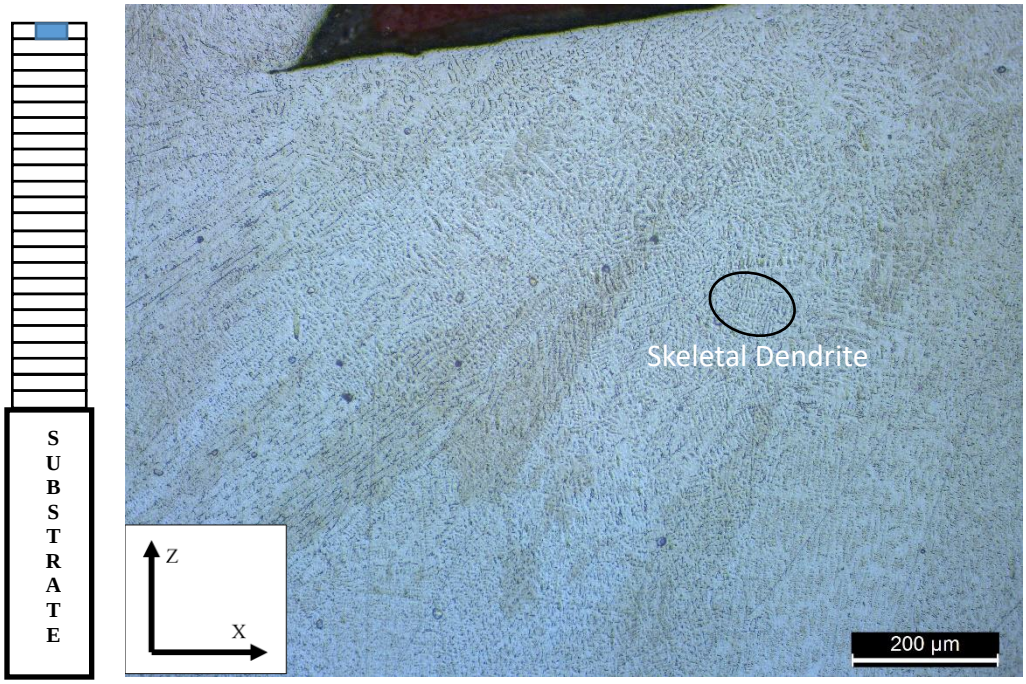

Figure 19: A high-power input sample containing primarily FA structures with lathy and skeletal dendrite formations

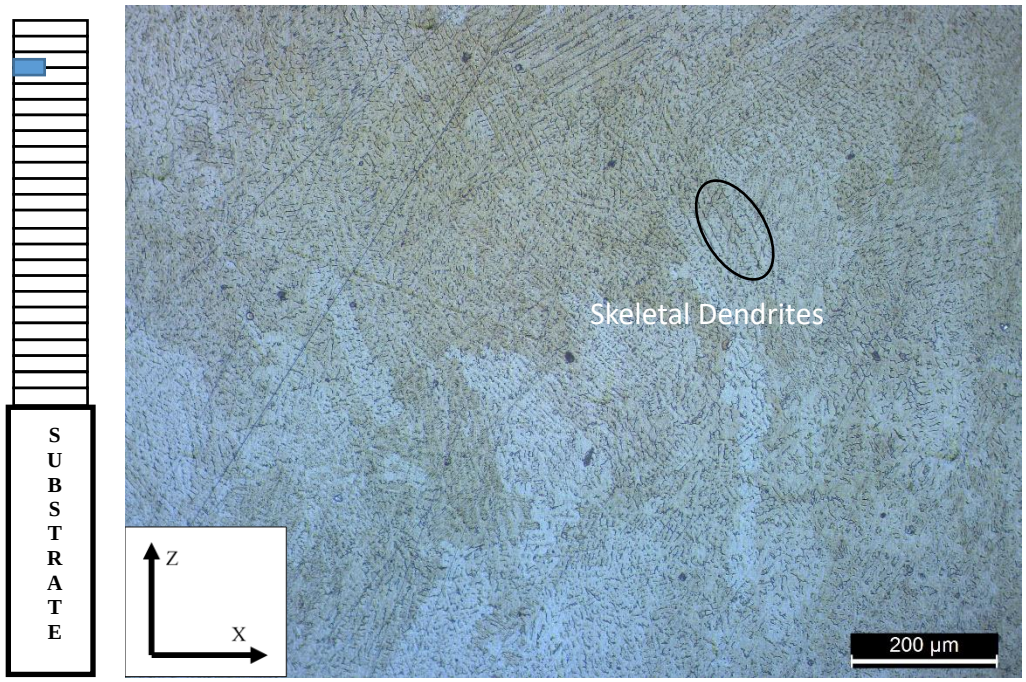

Figure 20: A high-power input sample containing a mixture of AF and FA solidification features and random orientations for the features.

5.1.1.1.2. YZ Orientation

The YZ orientation produced the coarser grain features compared to the XZ orientation. Like the XZ orientation, YZ samples contain predominant FA solidification structures with long dendrites with very fine secondary dendrite spacing at most locations, but with more type A and AF solidification structures such as planar and cellular structures located near a weld layer boundary. Figures 21 through 23 display representative features of the YZ dabber orientation.

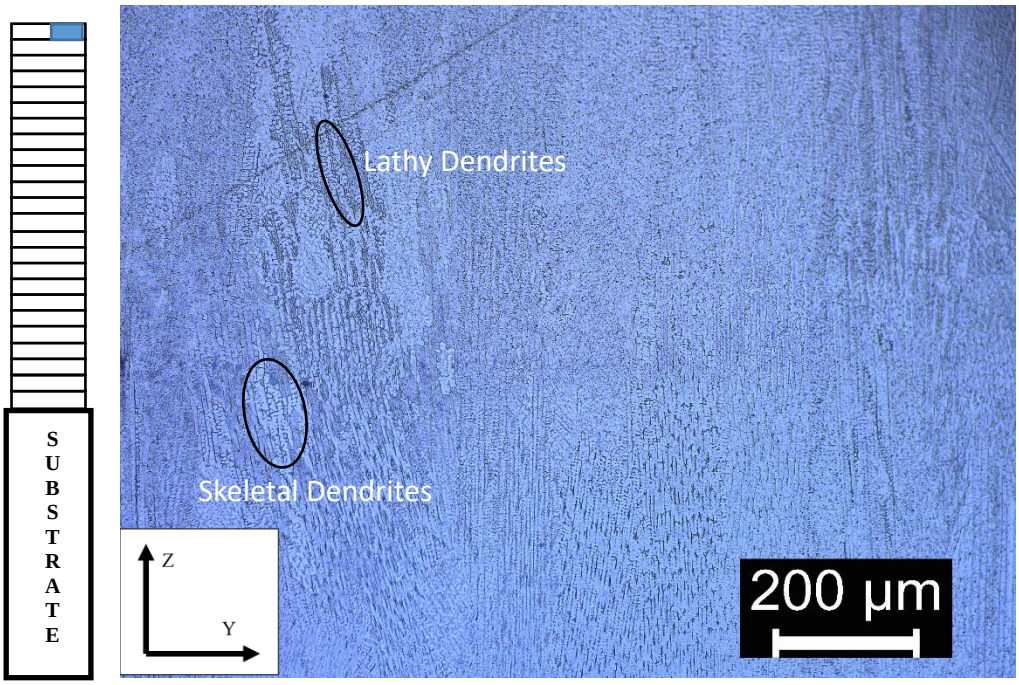

Figure 21: A high-power input sample containing primary FA solidification type features but has some scattered AF solidification and an area of type A solidification in the upper left corner (the featureless lighter colored area). Orientation of features trends upwards

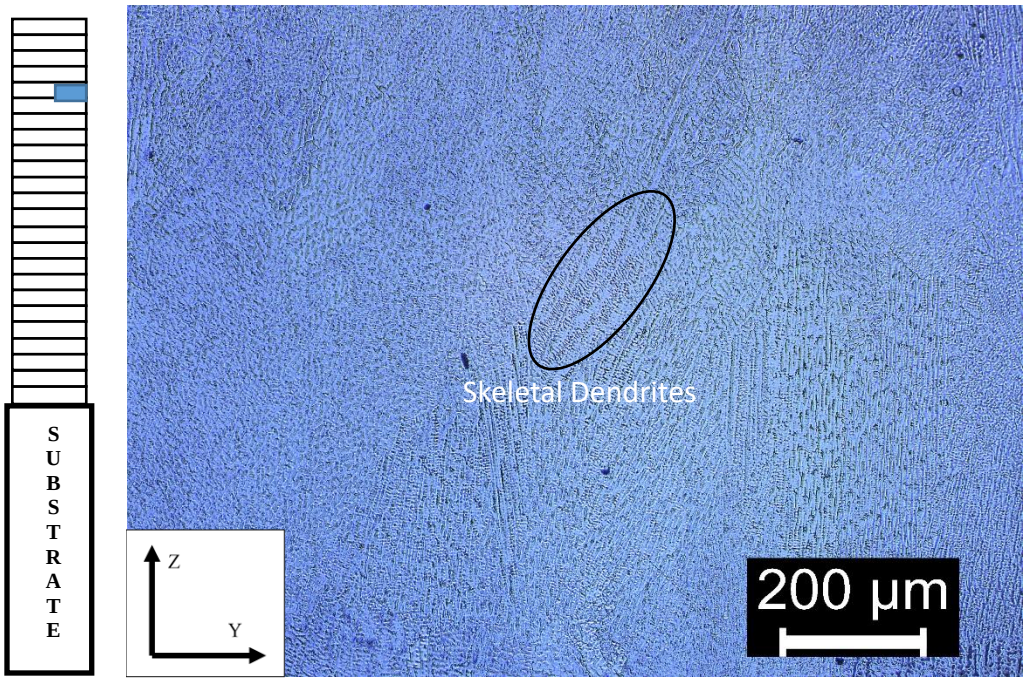

Figure 22: A high-power input sample containing primary FA solidification type features but has some scattered AF solidification. Orientation of features trends upwards

Figure 23: A high-power input sample containing primary FA solidification type features but has some scattered AF solidification in appearance. Orientation of features trends upwards and to the left towards center

5.1.1.1.3. XY Orientation

The XY orientation produced relatively fine grain features, containing FA solidification structures with long dendrites with very fine secondary dendrite spacing at most locations with little to no type AF or A solidification structures. This was likely due to the samples being examined close to the middle of a layer. Figure 24 is an example of the representative features typically seen in the XY orientation.

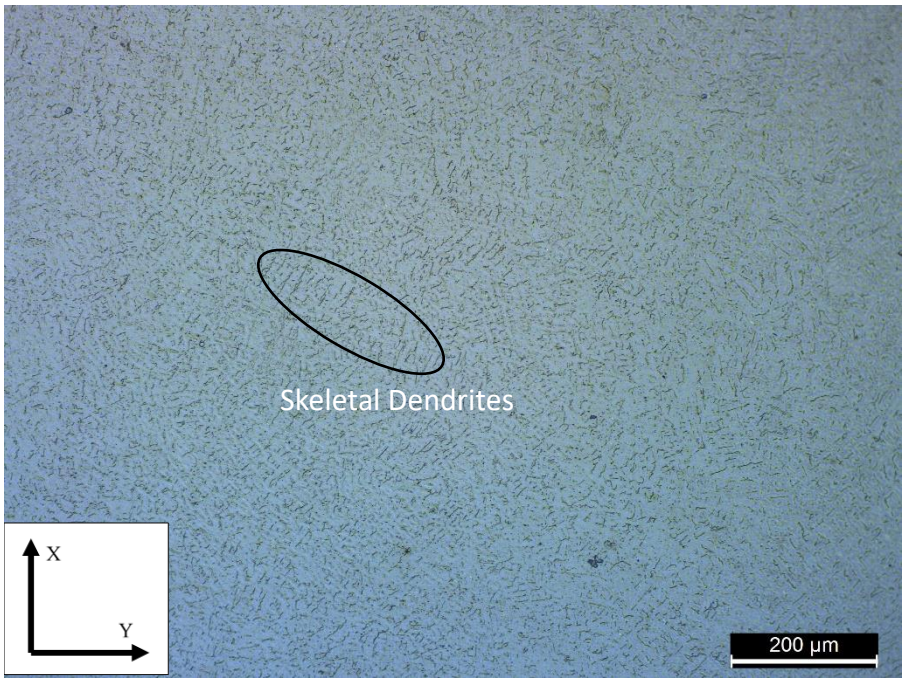

Figure 24: A high-power input sample containing primary AF solidification type features. Orientation of features have no predominant orientation

5.1.1.2. Medium Power Input

Medium power input samples overall had the finest average dendrite feature sizes of both the dabber and continuous power inputs, producing very fine, skeletal and lathy dendrite features throughout the sample.

5.1.1.2.1. XZ Orientation

The XZ orientation overall produced coarser dendrite feature sizes than the YZ orientation, containing predominant FA solidification structures at most locations, but with more

type A and AF solidification structures such as planar and cellular structures located near a weld layer boundary. Figures 25 through 27 below are representative samples for the XZ orientation.

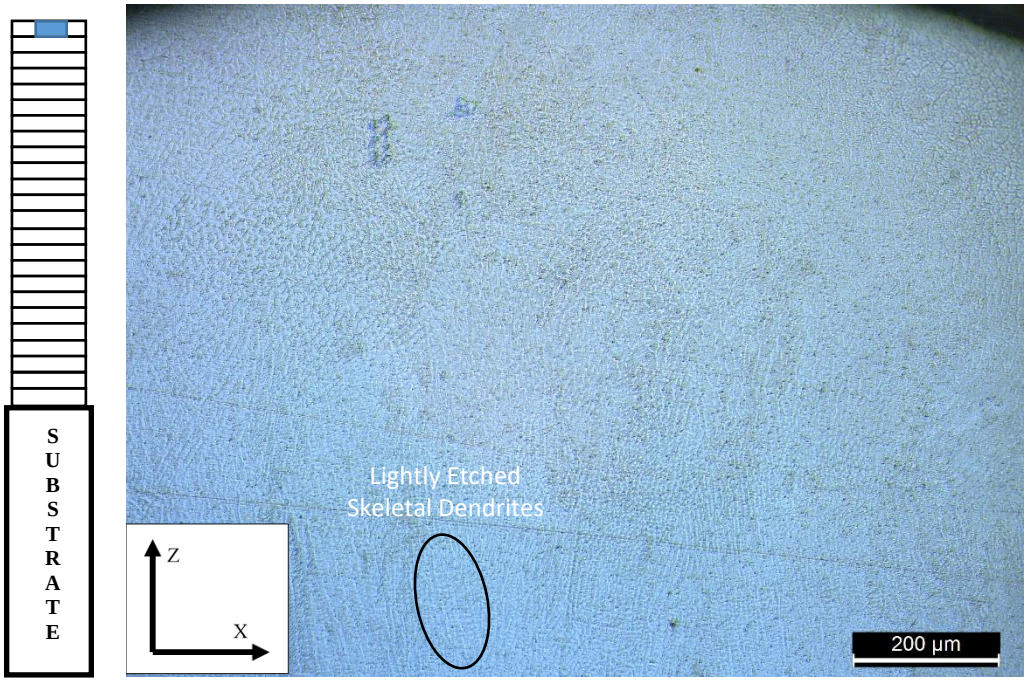

Figure 25: A medium power input sample containing primary AF solidification type features, including cellular structures at the top right of the sample. Some scattered FA solidification including lathy ferrite formations. Orientation of features trends generally upwards but no strong orientation

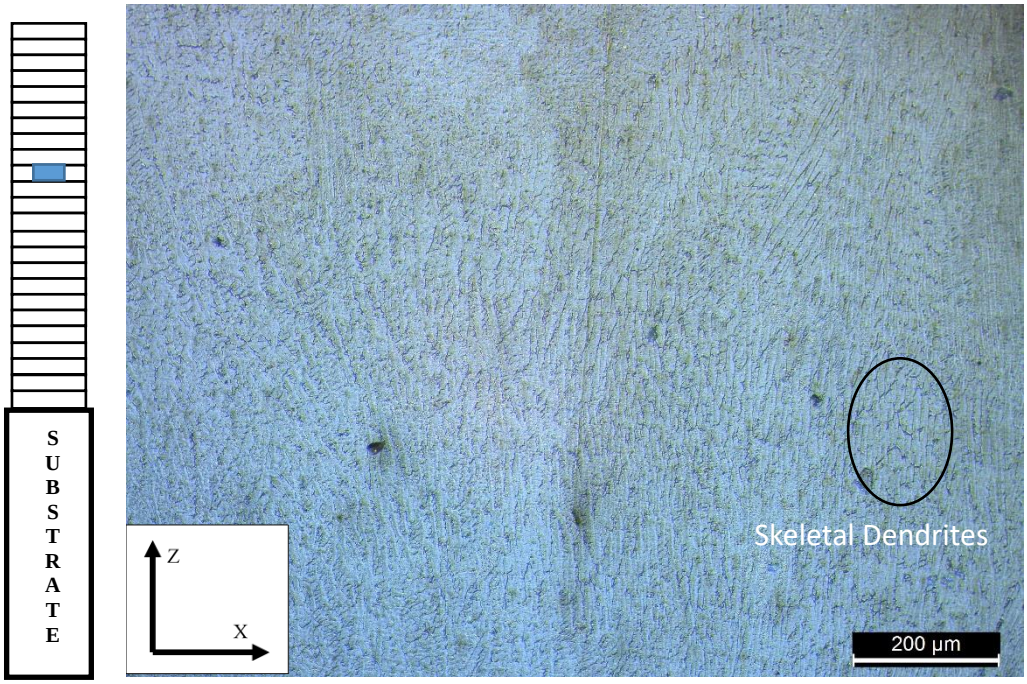

Figure 26: A medium power input sample containing primary AF solidification type features with limited FA solidification in the center of the image. Orientation of features trends generally upward

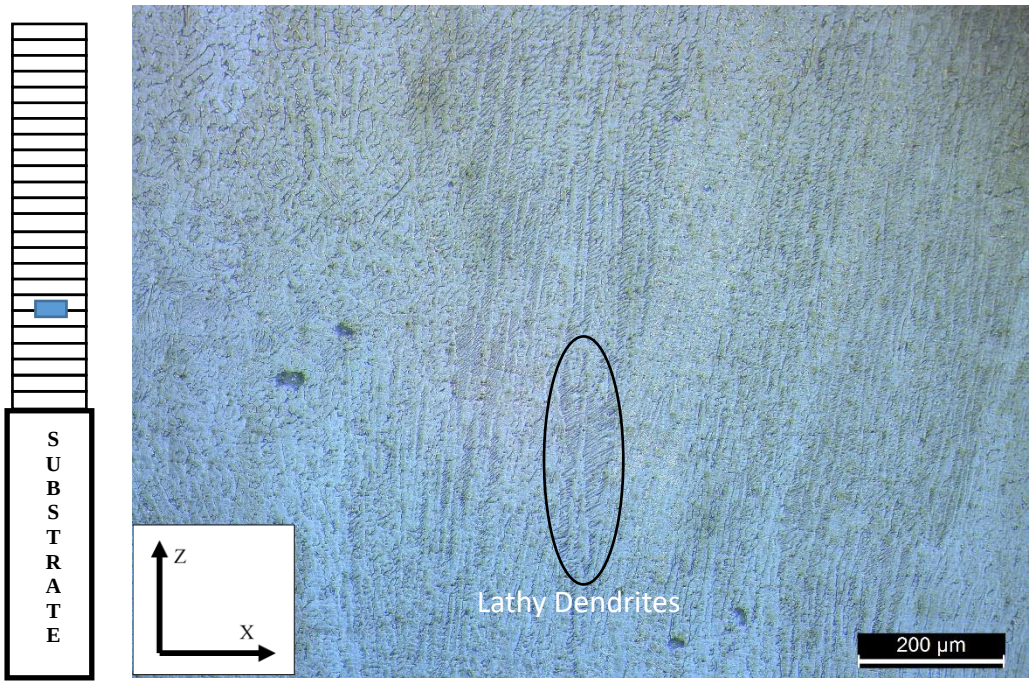

Figure 27: A medium power input sample containing primary AF solidification type features with lathy FA solidification in the center of the image. Orientation of features trends generally upward

5.1.1.2.2. YZ Orientation

The YZ orientation produced the finer grain features compared to the XZ orientation. Like the XZ orientation, YZ samples contain predominant FA solidification structures with a mixture of lathy ferrite and skeletal dendrites with varying lengths that have very fine secondary dendrite spacing at most locations. Some type A and AF solidification structures such as planar, cellular, and equiaxed structures were located near a weld layer boundary. Figures 28 through 30 display the representative features seen in the YZ orientation.

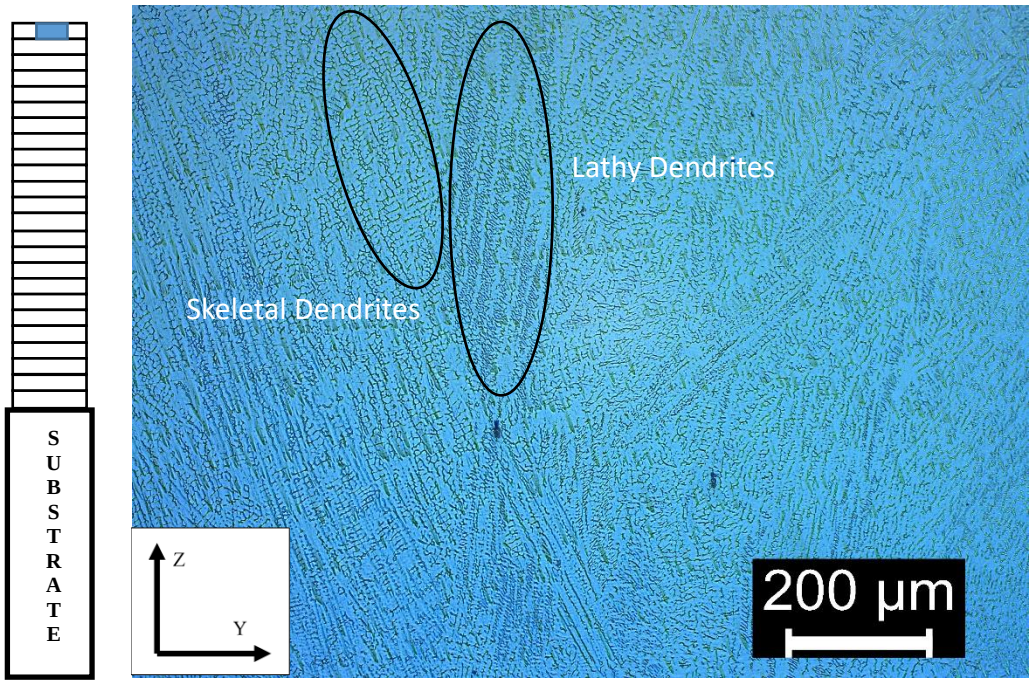

Figure 28: A medium power input sample containing primary FA solidification type features with significant amounts of relatively equiaxed skeletal dendrites and lathy ferrite. Orientation of features trends generally upward

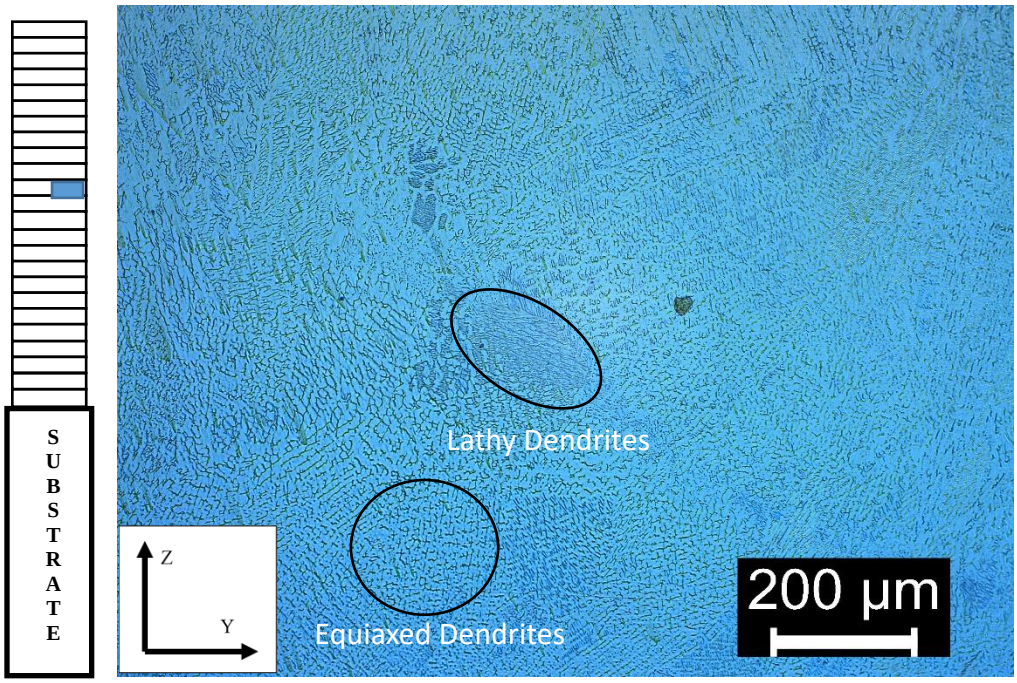

Figure 29: A medium power input sample containing primary FA solidification type features with significant amounts of small, unformed skeletal dendrites and patches of lathy ferrite. Orientation has no consistent tendencies.

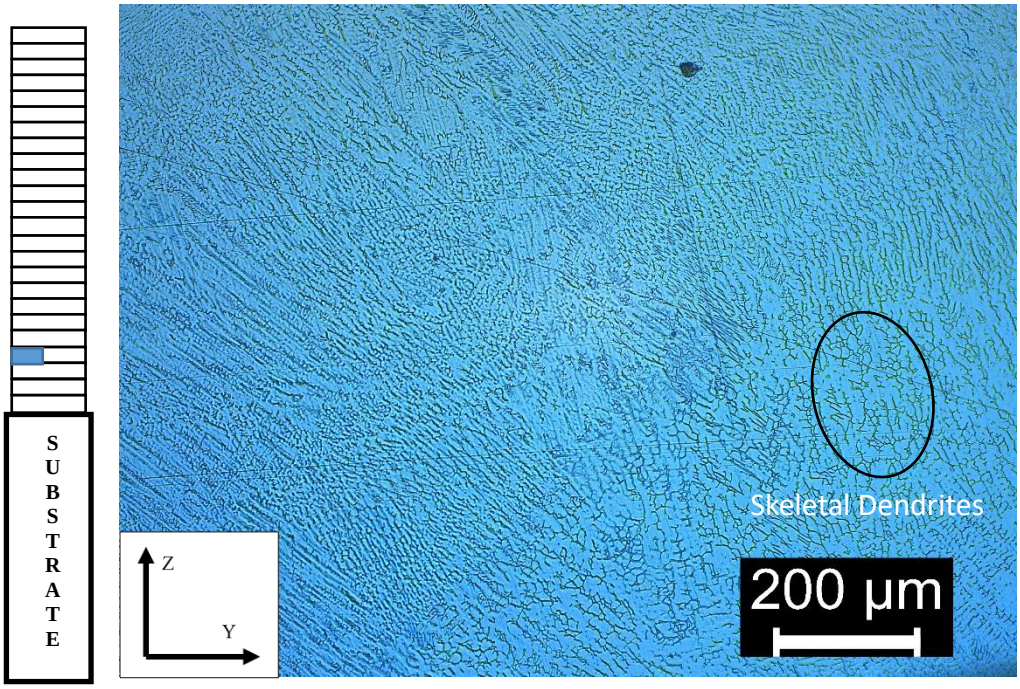

Figure 30: A medium power input sample containing primary AF solidification type features with some well-defined FA solidification skeletal dendrite features.

5.1.1.2.3. XY Orientation

The XY orientation produced relatively fine grain features, containing FA solidification structures with lathy and scattered skeletal dendrites with fine secondary dendrite spacing at most locations with little to no type AF or A solidification structures. This was likely due to the samples being examined close to the middle of a layer. Figure 31 is an example of the representative features typically seen in the XY orientation.

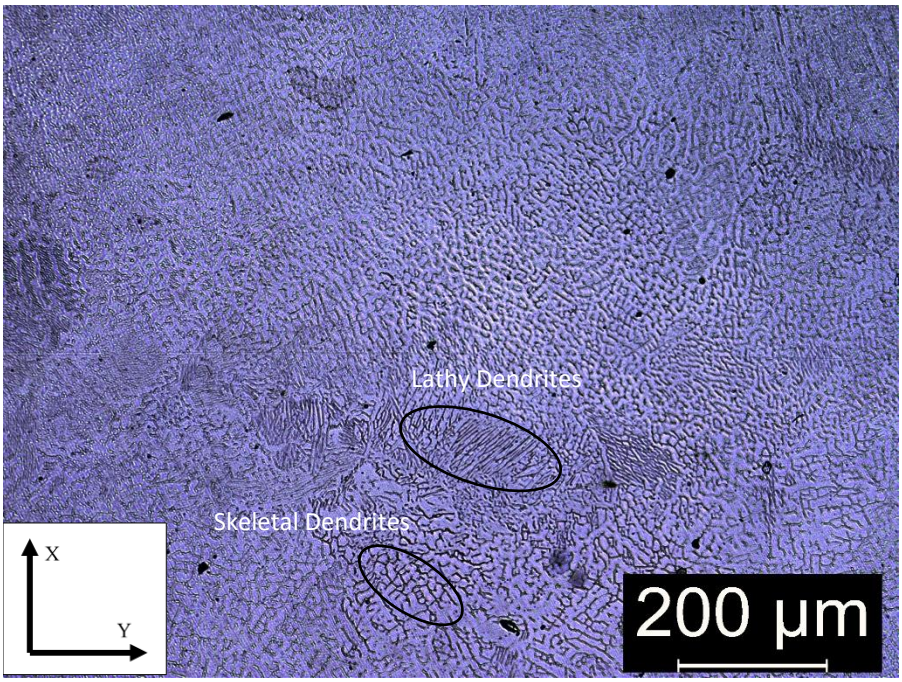

Figure 31: A high-power input sample containing primary AF solidification type features. Orientation of features have no predominant orientation

5.1.1.3. Low Power Input

Low power input samples overall had the coarsest average dendrite feature sizes of the dabber power inputs, producing a mixture of fine and coarse features in the specimens.

5.1.1.3.1. XZ Orientation

The XZ orientation overall produced considerably finer dendrite feature sizes than the YZ orientation, containing predominant FA solidification structures at most locations, but with more

type A and AF solidification structures such as planar and cellular structures located near a weld layer boundary. Figures 32 through 34 below are representative samples for the XZ orientation.

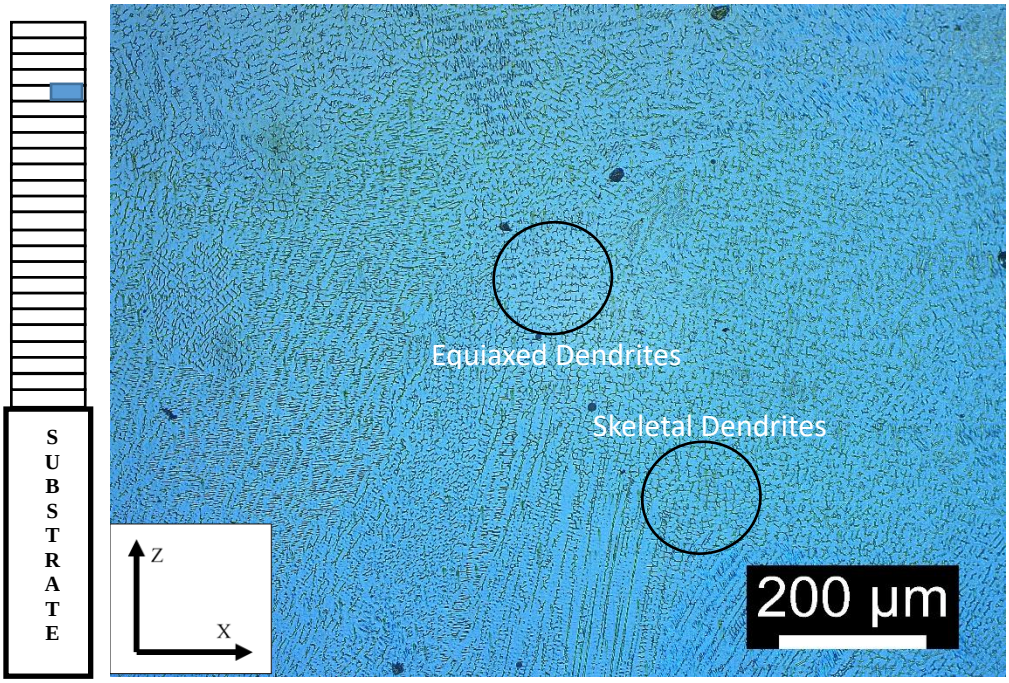

Figure 32: A low power input sample containing primary FA solidification type features with very fine features of equiaxed dendritic with some lathy and skeletal features. Some dominant directional growth upwards.

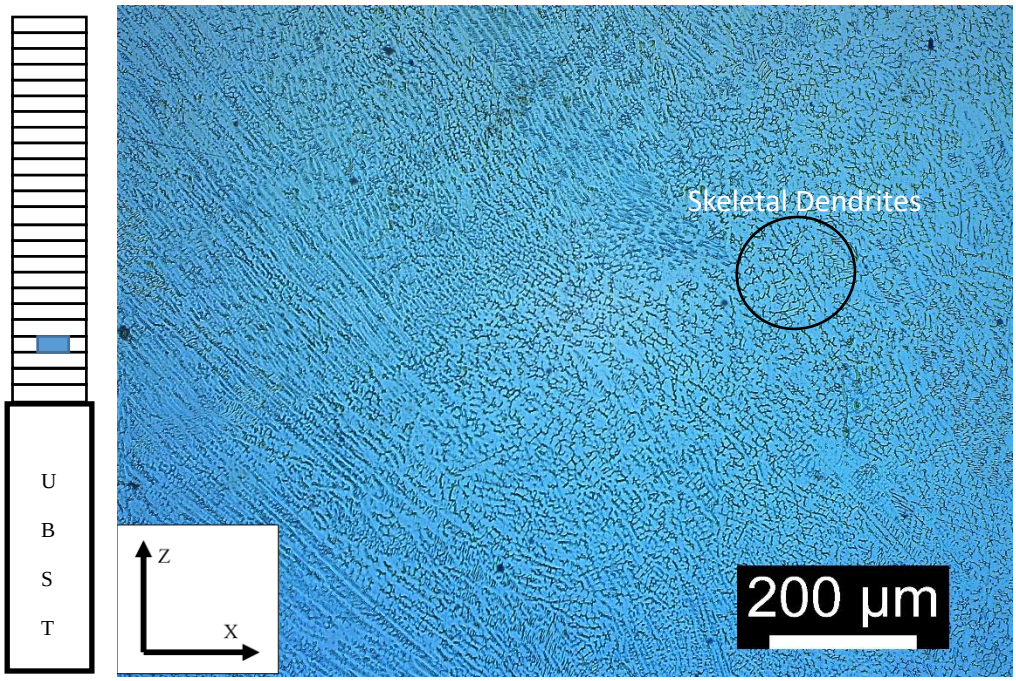

Figure 33: A low power input sample containing primary FA solidification type features with skeletal and some lathy features. At a boundary towards the center and bottom of the sample with dominant directional growth up and towards the left.

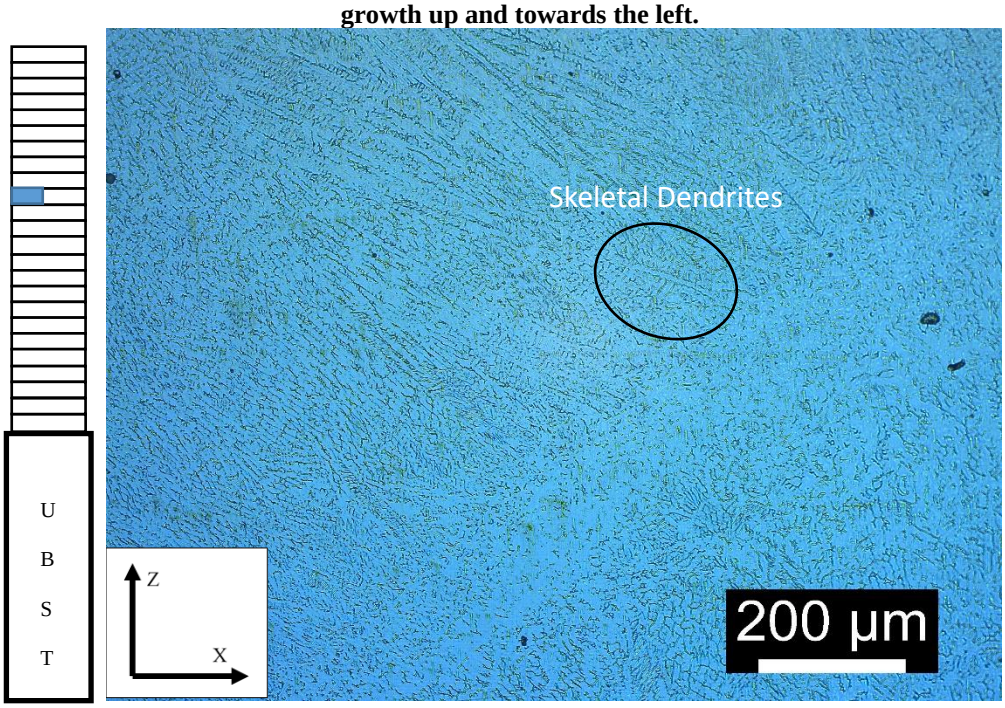

Figure 34: A low power input sample containing primary FA solidification type features at a boundary between layers with some AF solidification at the layer boundary.

5.1.1.3.2. YZ Orientation

The YZ orientation produced considerably coarser grain features compared to the XZ orientation. Like the XZ orientation, YZ samples contain predominant FA solidification structures with a mixture of lathy ferrite and skeletal dendrites with varying lengths that have fine and coarse secondary dendrite spacing. Some type A and AF solidification structures such as planar, cellular, and equiaxed structures located near a weld layer boundary. Figures 35 through 37 display the representative features seen in the YZ orientation.

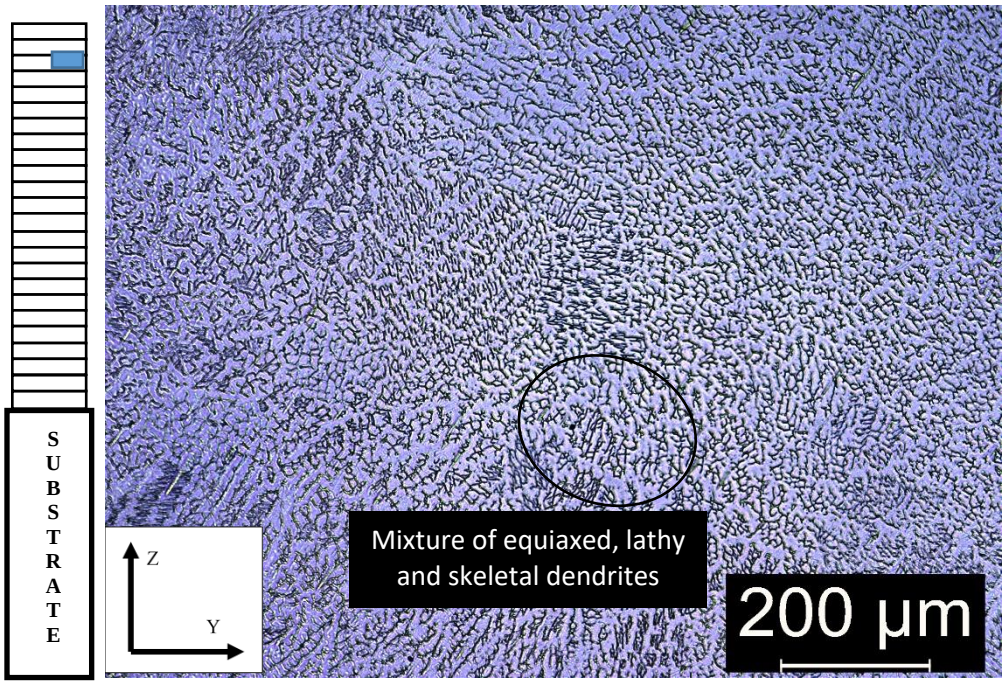

Figure 35: A low power input sample containing primary FA solidification type features with fine equiaxed dendrite structures

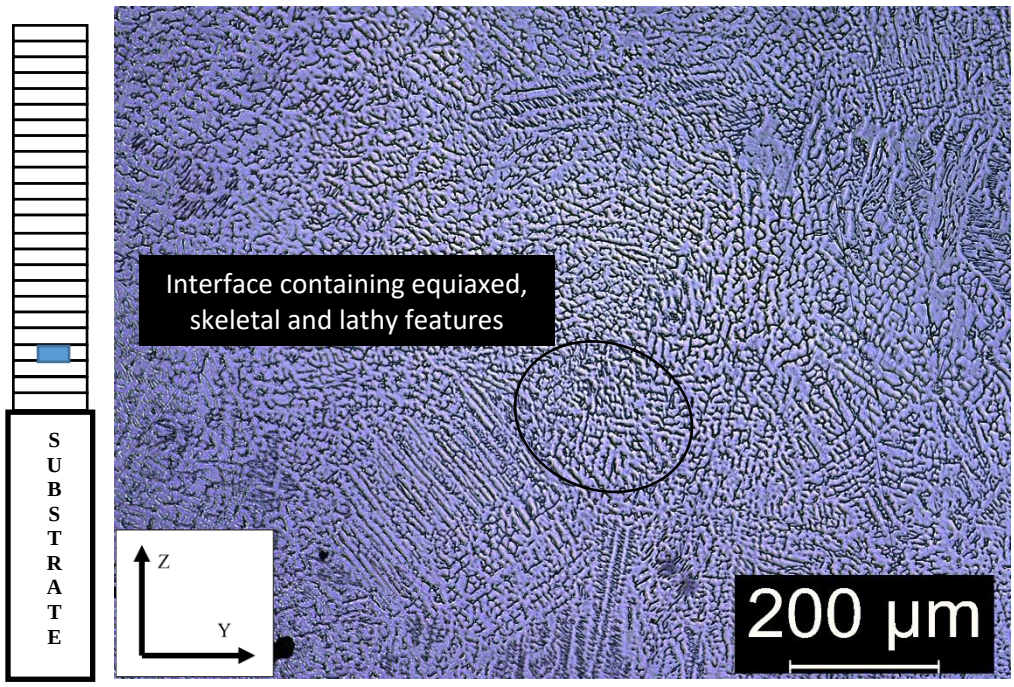

Figure 36: A low power input sample containing primary FA solidification type features with skeletal and some lathy features. At a boundary towards the center and bottom of the sample with dominant directional growth up and towards the left.

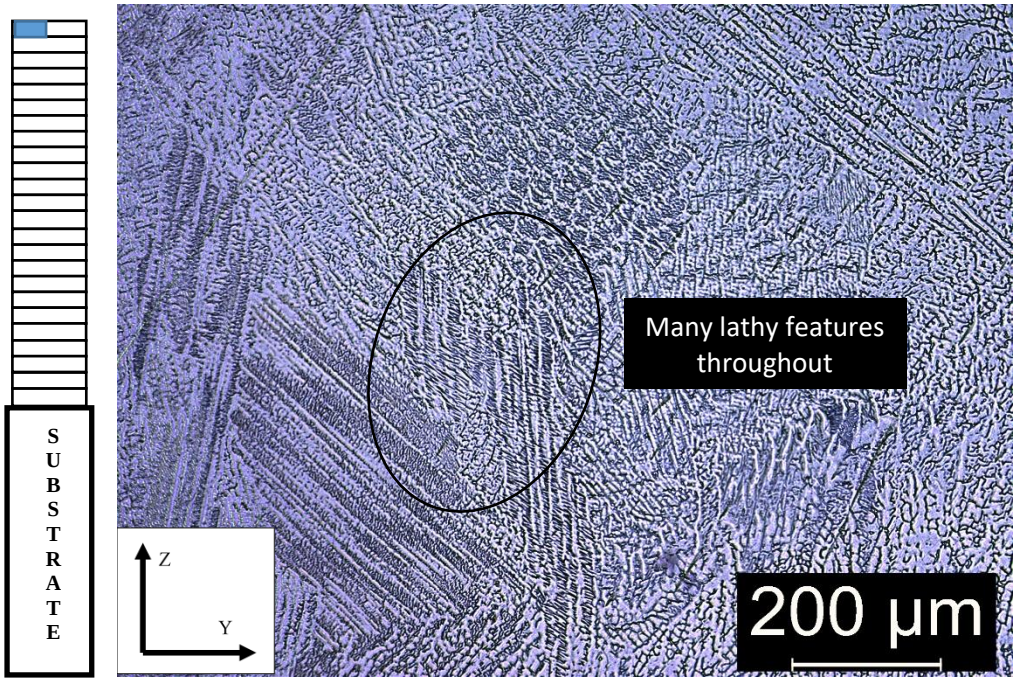

Figure 37: A low power input sample containing primary FA solidification type features at a boundary between layers with some AF solidification at the layer boundary.

5.1.1.3.3. XY Orientation

The XY orientation produced relatively fine grain features, containing FA solidification structures with lathy and scattered skeletal dendrites with fine secondary dendrite spacing at most locations with little to no type AF or A solidification structures as samples were examined close to the middle of a layer. Figure 38 is an example of the representative features typically seen in the XY orientation.

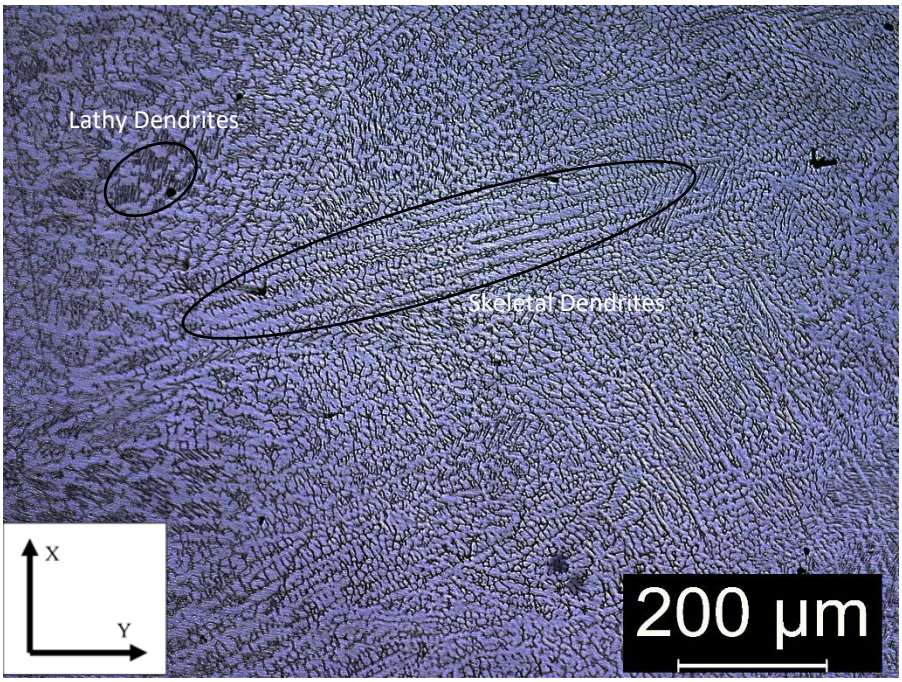

Figure 38: A low power input dabber XY sample with primary FA solidification with lathy ferrite and long skeletal dendrite features.

5.1.1.4. Dendrite Spacing

Dendrite spacing analysis was performed using the Leica Application Suite Dendrite Expert Analysis package. Figure 39 below is the result of analyzing at least 4 images that contained enough skeletal or lathy dendrite features to perform between 8 and 50 separate measurements per image using the software. The compiled tables for dendrite spacing can be found in Appendix A.

Dendrite spacing for the XZ orientation was similar with averages between 7.4 and 8 microns. The YZ orientation had a wider spread in values, ranging from 7.4 and 10.1 microns in length. The high and low power inputs also both had the XZ orientation as the orientation that produced finer structures while the XZ orientation was coarser in the medium power input.

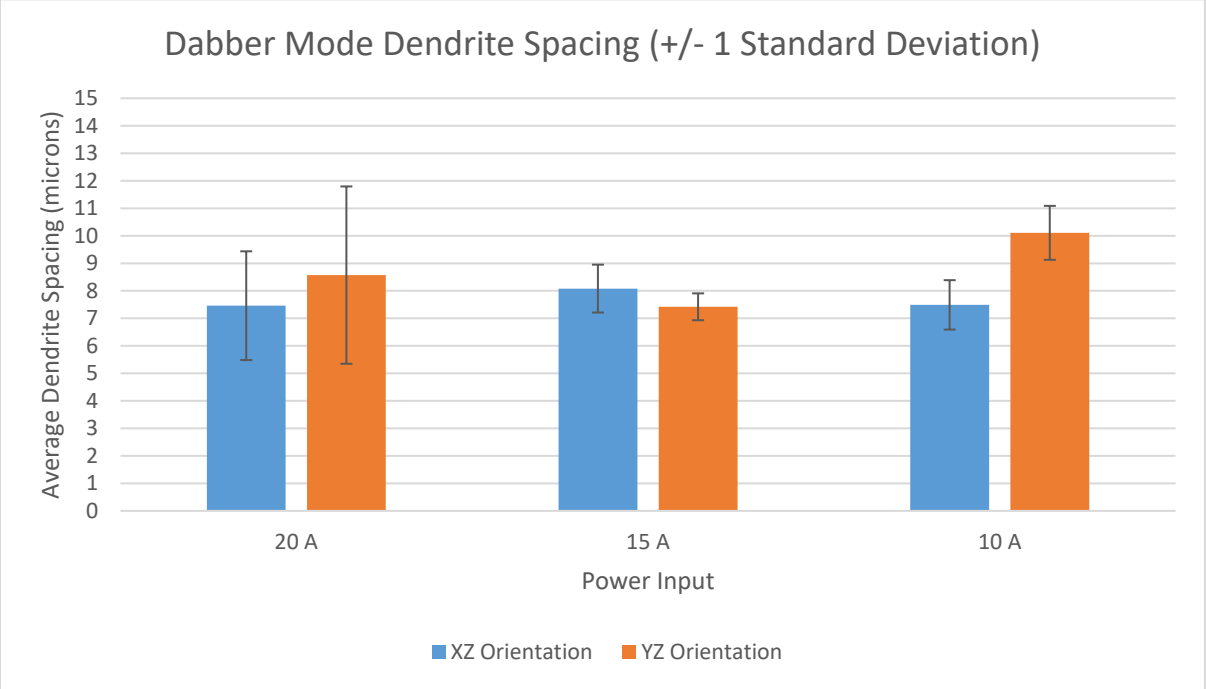

Figure 39: Average Dendrite Spacing for Dabber Mode XZ and YZ samples

5.1.2. Continuous Mode

Continuous mode images display feature sets that are relatively coarse in size across all power inputs and orientations, displayed distinct vertical tendencies in growth direction in the XZ and YZ orientations. Continuous mode overall tended to favor FA type solidification grain structure features with coarser, and more numerous skeletal dendrites.

5.1.2.1. High Power Input

High power input samples overall had the finest average dendrite feature sizes of the continuous power inputs, producing a mixture of coarse skeletal dendrite features in the specimens.

5.1.2.1.1. XZ Orientation

The XZ orientation overall produced considerably finer dendrite feature sizes than the YZ orientation, containing predominant FA solidification structures at most locations, but with more type A and AF solidification structures such as planar and cellular structures located near a weld layer boundary. Figures 40 through 42 below are representative samples for the XZ orientation.

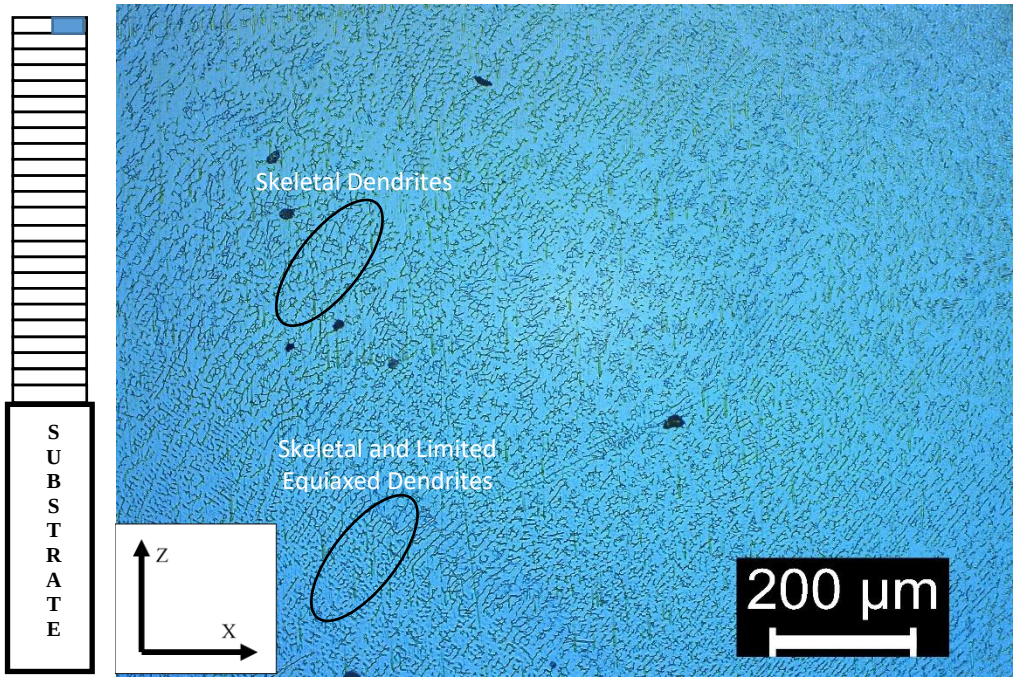

Figure 40: A high-power input sample containing primary FA solidification type features with varying lengths of skeletal dendrites and some limited AF solidification. Orientation trends up and to the right.

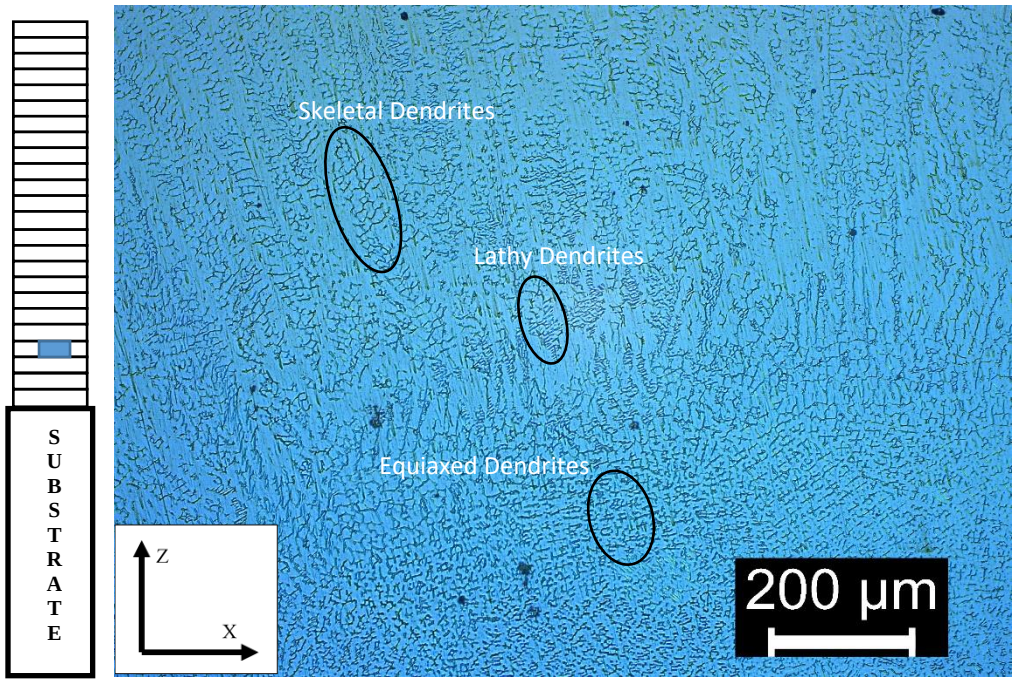

Figure 41: A high-power input sample containing primary FA solidification type features with varying lengths of skeletal dendrites and some limited AF solidification. Orientation trends up and slightly to the left above the layer deposit.

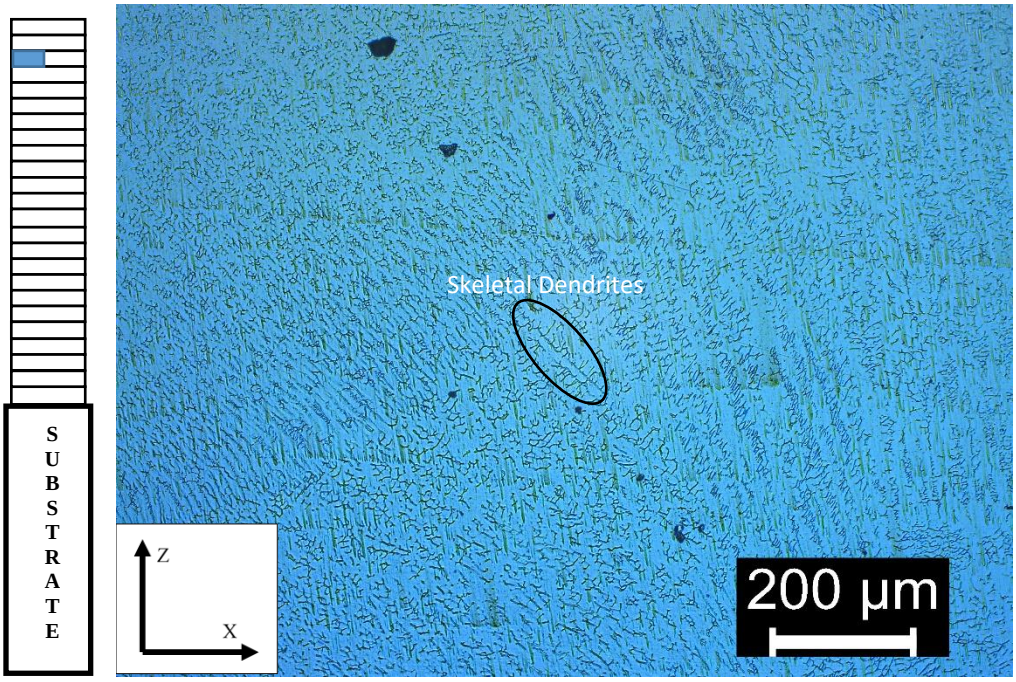

Figure 42: A high-power input sample containing primary FA solidification type features with fine skeletal dendrite structures. Some limited AF solidification. Orientation trends up and to the left.

5.1.2.1.2. YZ Orientation

The YZ orientation produced coarser grain features compared to the XZ orientation. Like the XZ orientation, YZ samples contain predominant FA solidification structures with primarily skeletal dendrites with varying lengths that have coarse secondary dendrite spacing. Some type A and AF solidification structures such as planar, cellular, and equiaxed structures located near a weld layer boundary. Figures 43 through 45 display the representative features seen in the YZ orientation.

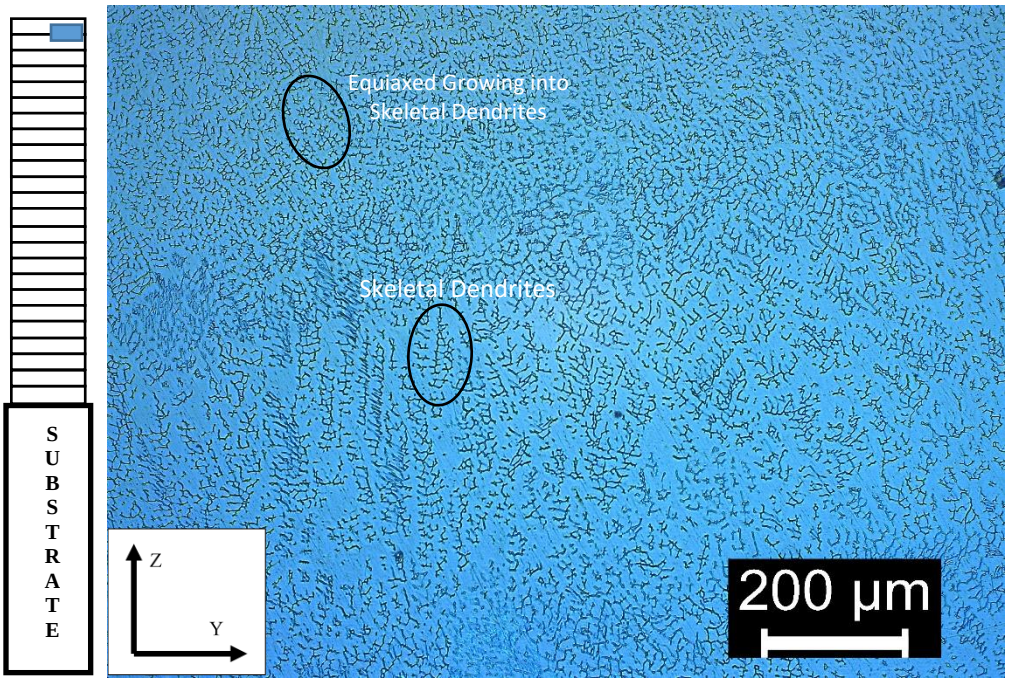

Figure 43: A high-power input sample containing primary FA solidification type at the first layer boundary. Mixture of small equiaxed features at top layer with more coarse skeletal dendrites in the layer deposit.

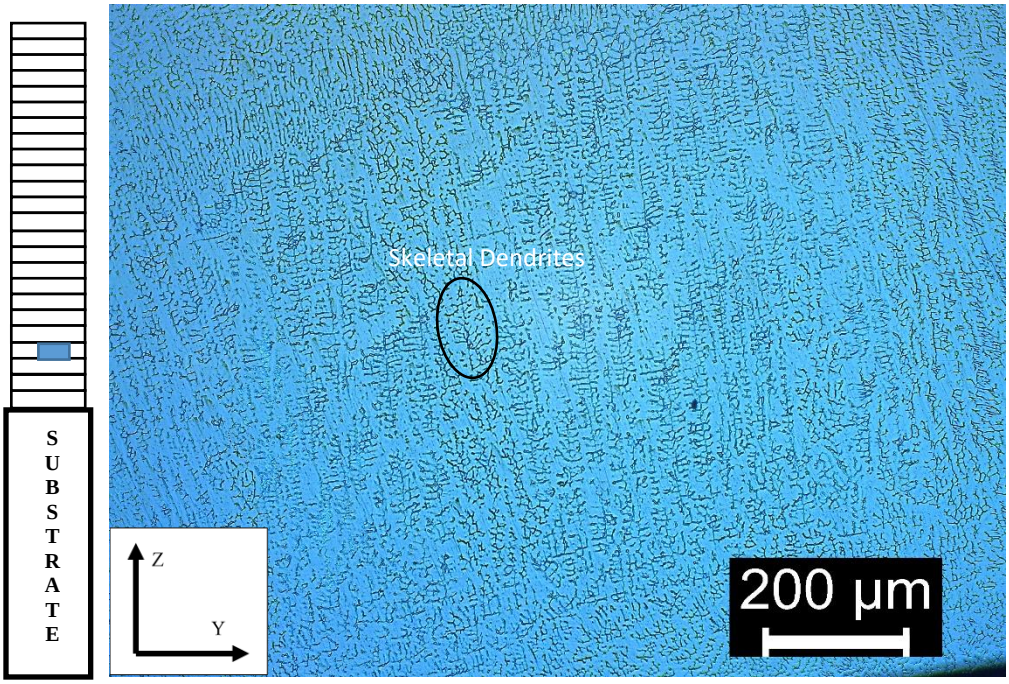

Figure 44: A high-power input sample containing primary FA solidification type with AF solidification. Scattered skeletal dendrites with orientation trending up and slightly to the left.

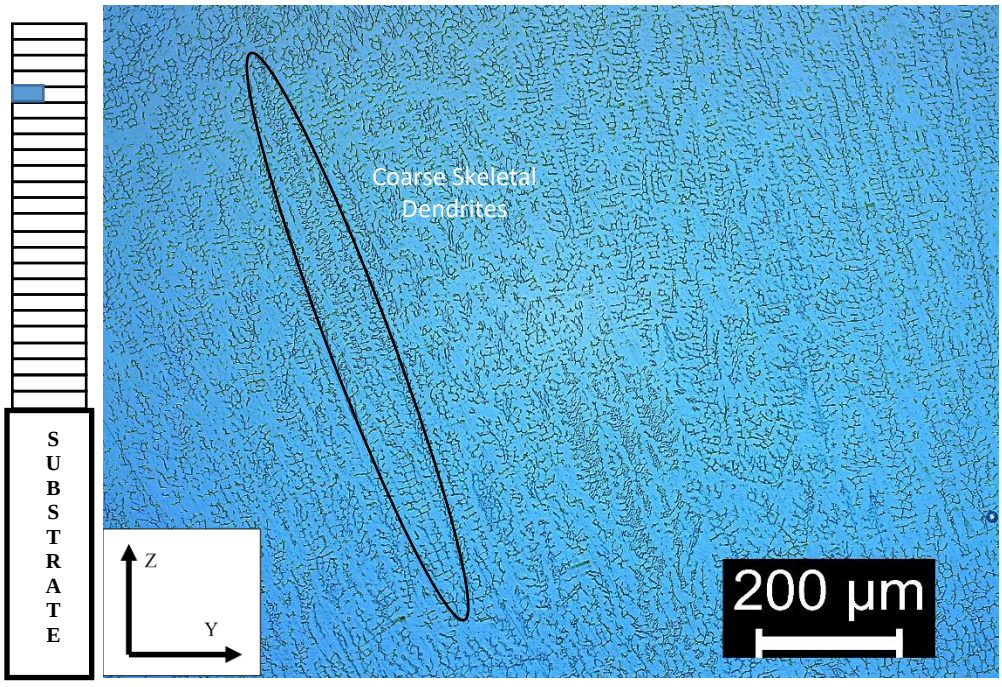

Figure 45: A high-power input sample containing primary FA solidification type with a mixture of long and shorter skeletal dendrites with solidification orientation trending up and to the left.

5.1.2.1.3. XY Orientation

The XY orientation produced relatively fine grain features, containing FA solidification structures with scattered skeletal dendrites with coarse secondary dendrite spacing at most locations with little to no type AF or A solidification structures. This was likely due to samples being examined close to the middle of a layer. Figure 46 is an example of the representative features typically seen in the XY orientation.

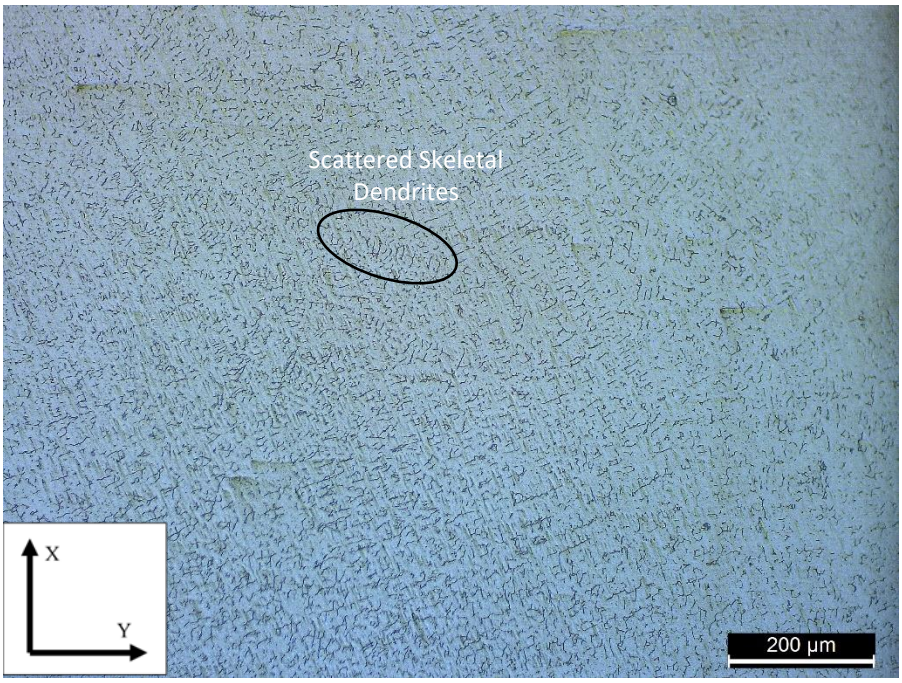

Figure 46: A high-power input XY sample containing primary FA solidification type features with scattered coarse skeletal dendrites.

5.1.2.2. Medium Power Input

Medium power input samples overall had relatively coarse average dendrite feature sizes, producing a mixture of coarse lathy dendrite and skeletal dendrite features in the specimens.

5.1.2.2.1. XZ Orientation

The XZ orientation overall produced somewhat finer dendrite feature sizes than the YZ orientation, containing predominant FA solidification structures such as lathy and skeletal dendrites at most locations, with little type A and AF solidification structures such as planar and

cellular structures located near a weld layer boundary. Figures 47 through 49 below are representative samples for the XZ orientation.

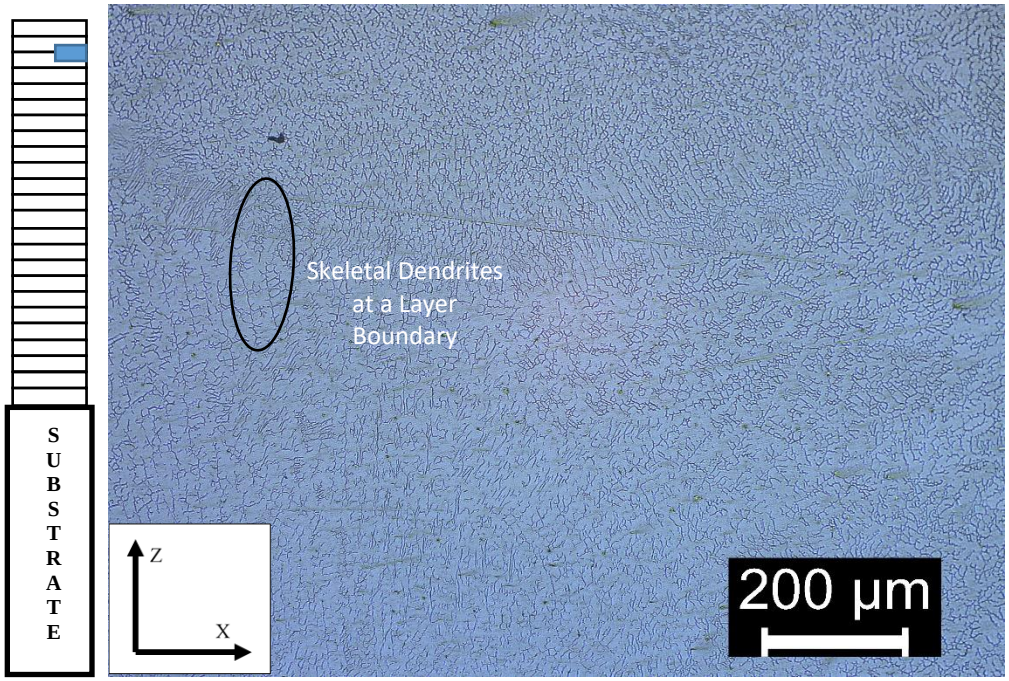

Figure 47: A medium power input sample containing primary FA solidification type features at a layer boundary. A mixture of long, coarse equiaxed skeletal dendrites below the boundary and fine, equiaxed dendrites at and above the layer boundary.

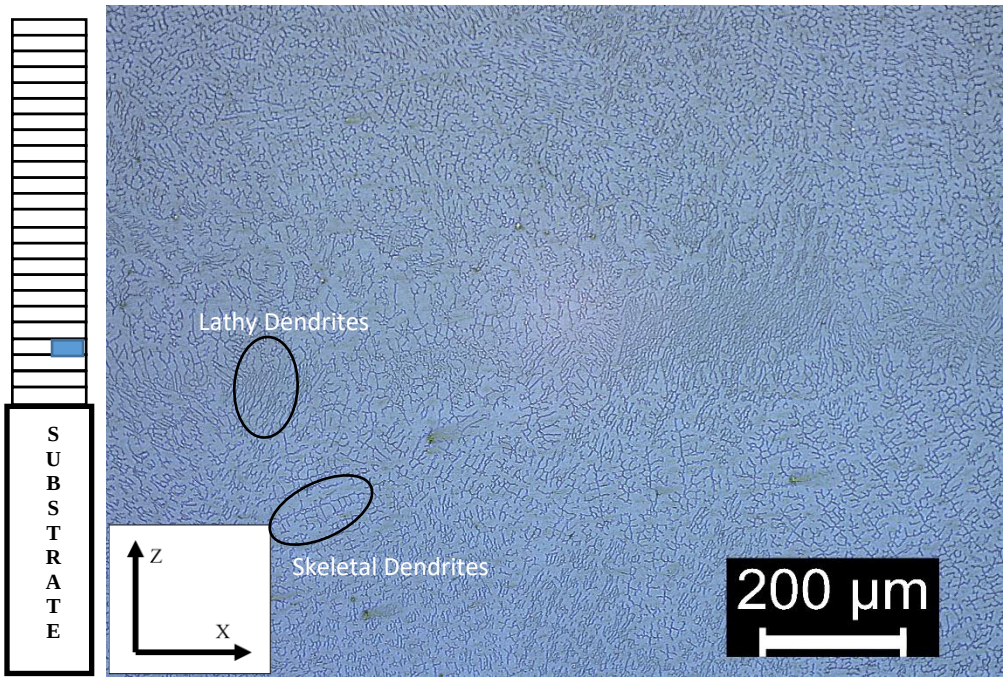

Figure 48: A medium power input sample containing primary FA solidification type features at a layer boundary. A mixture of coarse skeletal dendrites below the boundary lathy dendrites at layer boundary and small equiaxed features above the layer boundary. Orientation trends upwards.

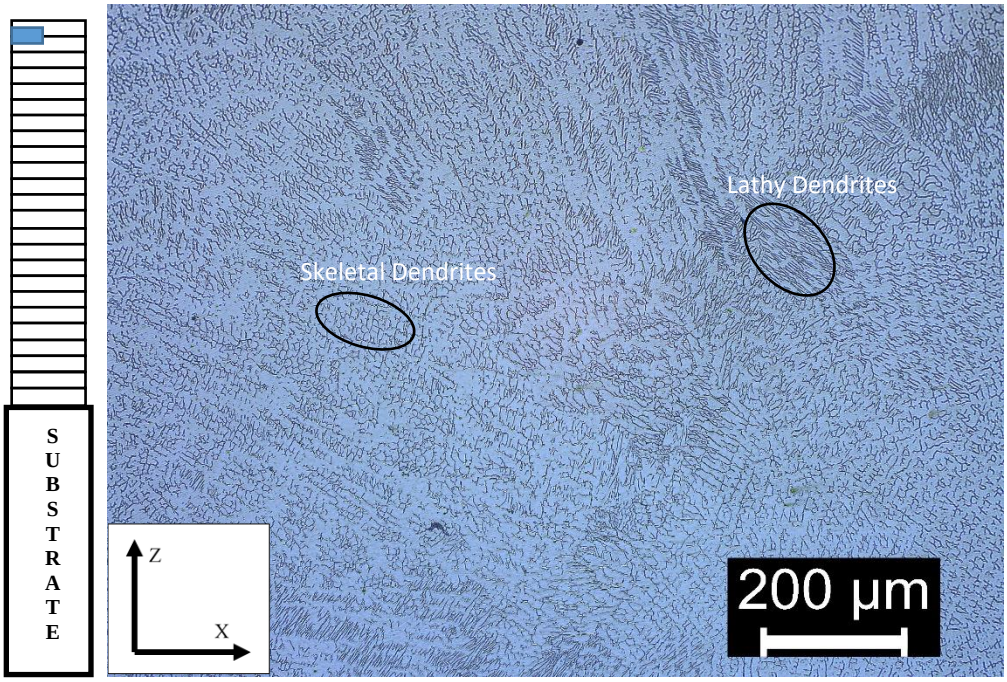

Figure 49: A medium power input sample containing primary FA solidification type features at a layer boundary. A mixture of skeletal dendrites below the boundary, lathy dendrites at layer boundary, and lathy and skeletal features above the layer boundary. Orientation trends upwards.

5.1.2.2.2. YZ Orientation

The YZ orientation produced coarser grain features compared to the XZ orientation. Like the XZ orientation, YZ samples contain predominant FA solidification structures with primarily skeletal dendrites with varying lengths that have coarse secondary dendrite spacing. A mixture of both lathy type FA features, and types A, and AF solidification structures such as planar, cellular, and equiaxed structures were located near a weld layer boundary. Figures 50 through 52 display the representative features seen in the YZ orientation.

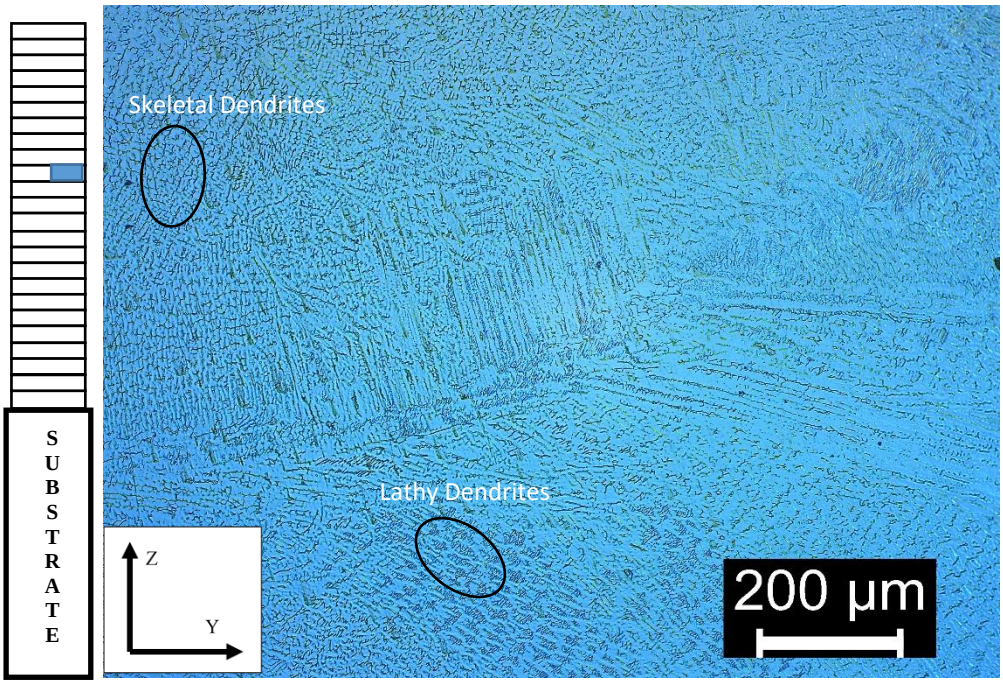

Figure 50: A medium power input sample containing primary FA solidification type features at a layer boundary. A mixture of skeletal and lathy dendrites below the boundary, lathy dendrites at layer boundary, and lathy and skeletal features above the layer boundary. Orientation trends upwards and to the left below the boundary and generally upwards.

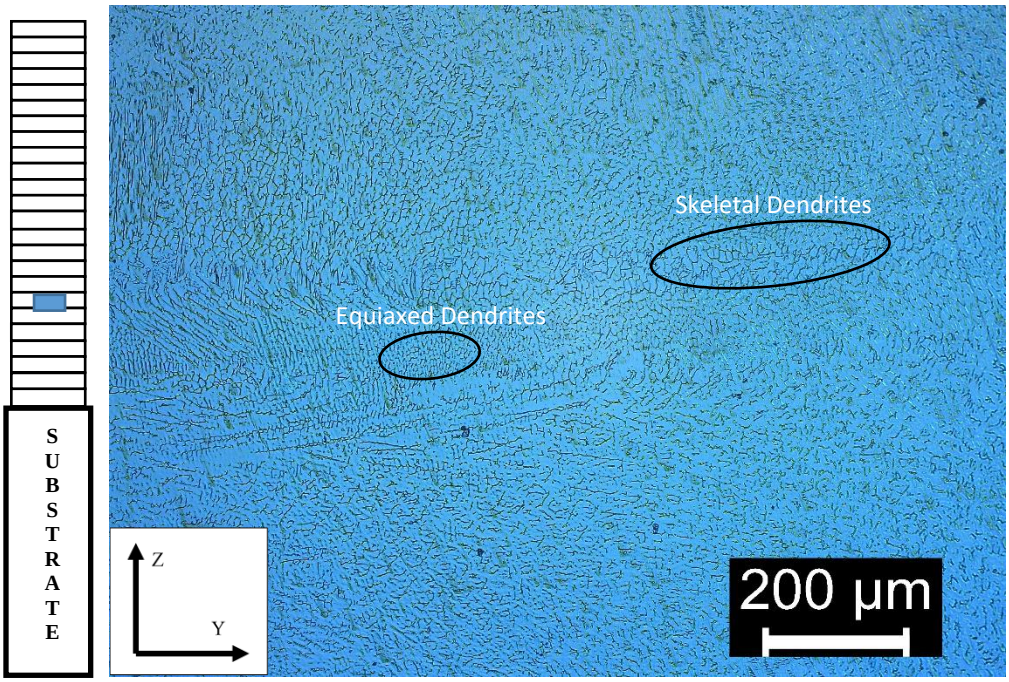

Figure 51: A medium power input sample containing primary FA solidification type features at a layer boundary. A mixture of skeletal dendrites below the boundary, lathy and equiaxed dendrites at the layer boundary, and skeletal and equiaxed features above the layer boundary. Orientation trends generally upwards, but no definitive solidification direction.

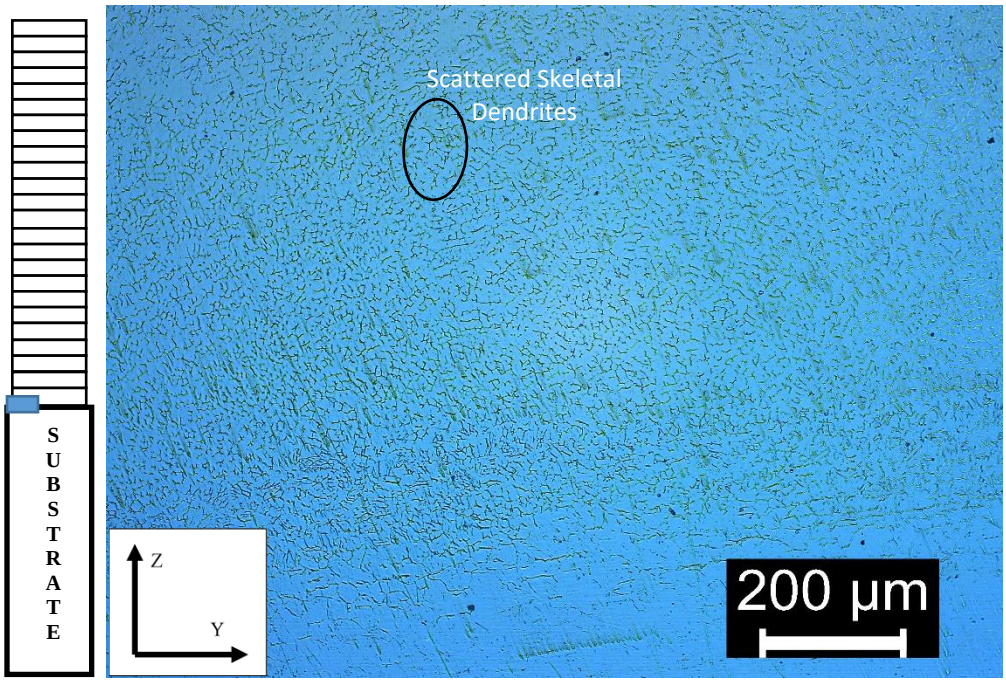

Figure 52: A medium power input sample containing primary AF solidification type features at a layer boundary between the bottom layer and the HAZ base metal. Features are fine and a mixture of equiaxed and some lathy features. Orientation trends generally upwards and to the left.

5.1.2.2.3. XY Orientation

The XY orientation produced relatively fine grain features, containing FA solidification structures with scattered skeletal dendrites with coarse secondary dendrite spacing at most locations with little to no type AF or A solidification structures as samples were examined close to the middle of a layer. Figure 46 is an example of the representative features typically seen in the XY orientation.

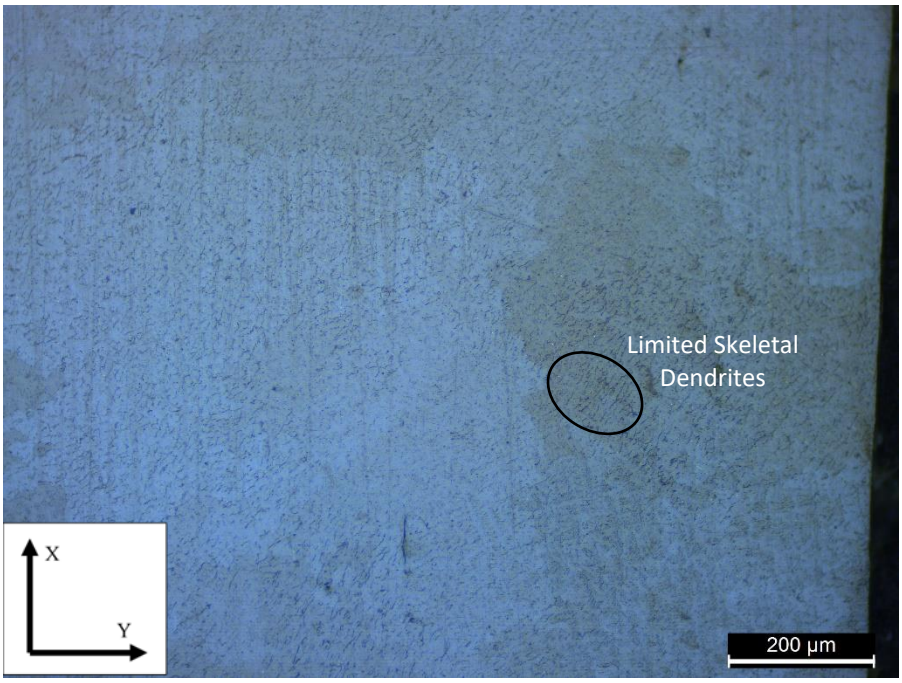

Figure 53: A medium power input XY sample containing primary FA solidification type features such as lathy and skeletal dendrites.

5.1.2.3. Low Power Input

Low power input samples overall had the coarsest average dendrite feature sizes of both the dabber and continuous modes, producing a mixture of coarse lathy dendrite and skeletal dendrite features in the specimens.

5.1.2.3.1. XZ Orientation

The XZ orientation overall produced the coarsest dendrite feature sizes of all power inputs, containing predominant FA solidification structures such as lathy and skeletal dendrites at most locations, with little type A and AF solidification structures such as planar and cellular structures located near a weld layer boundary. Figures 54 through 56 below are representative samples for the XZ orientation.

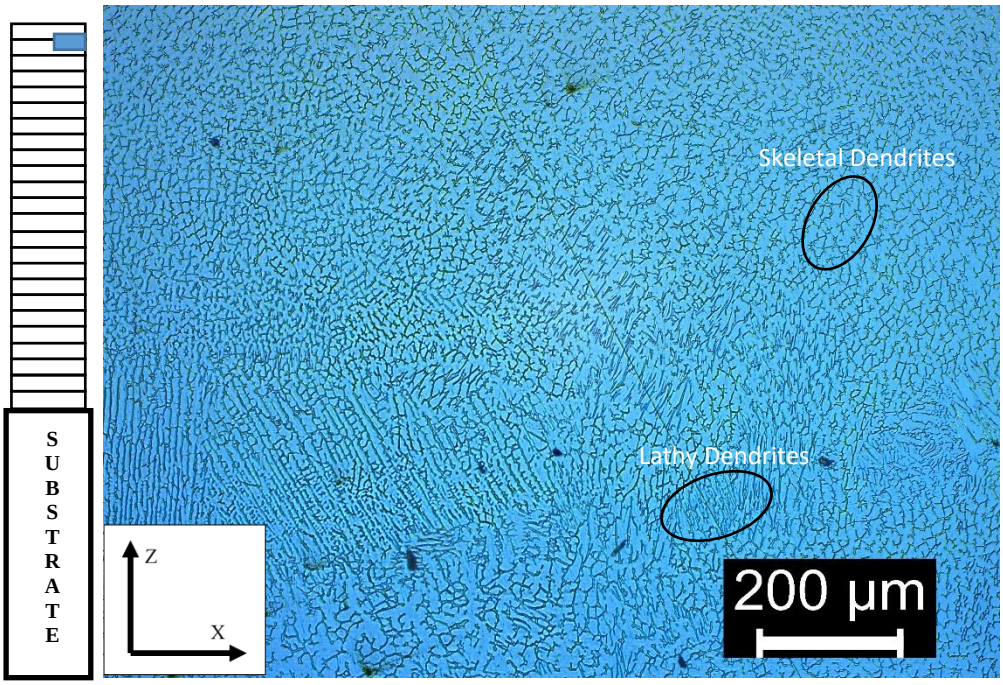

Figure 54: A low power input sample containing primary FA solidification type features at a layer boundary. A mixture of skeletal and limited lathy dendrites below the boundary, lathy and skeletal dendrites at the layer boundary, and skeletal and equiaxed features above the layer boundary. Orientation trends generally upwards, but no definitive solidification direction between layers.

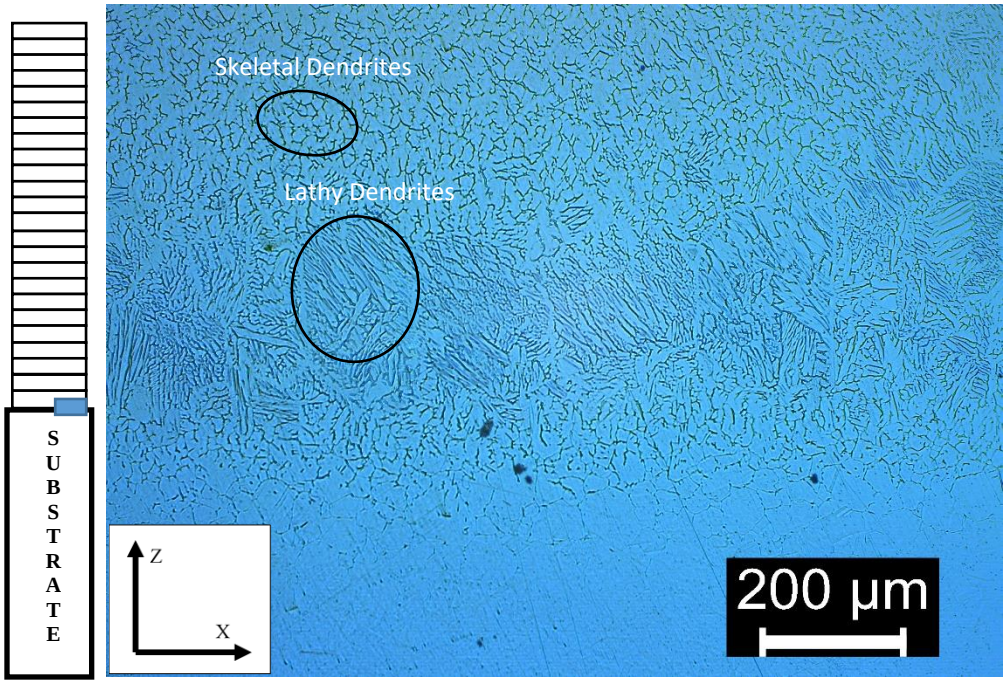

Figure 55: A medium power input sample containing primary AF solidification type features at a layer boundary between the bottom layer and the HAZ base metal. Features are fine and a mixture of equiaxed and lathy features with skeletal dendrites above the interface of the base metal and weld layer. Orientation trends generally upwards.

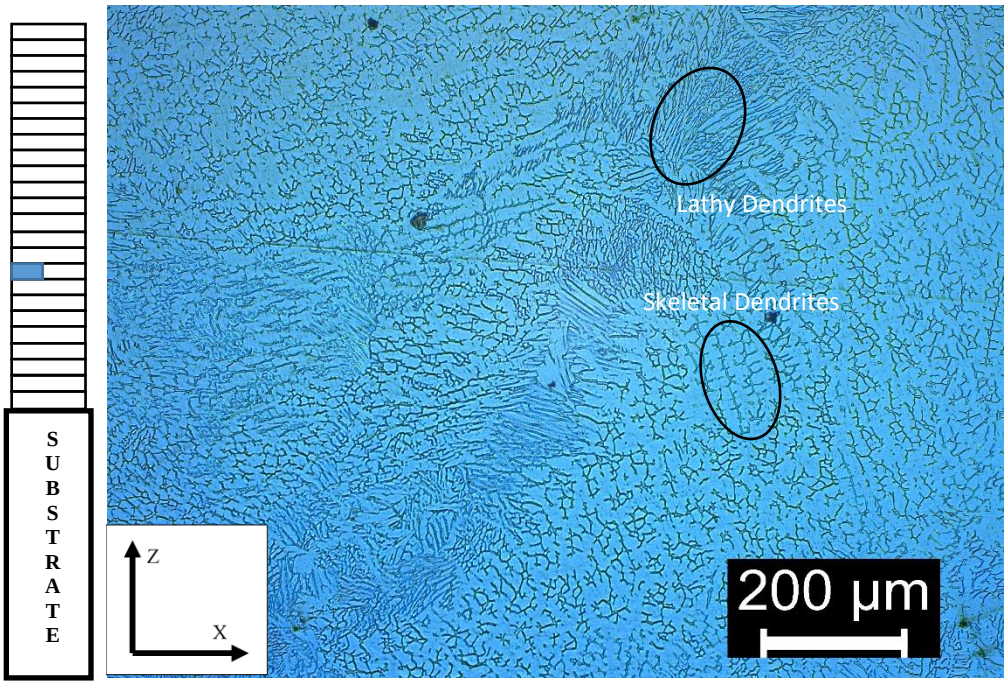

Figure 56: A low power input sample containing primary FA solidification type features at a layer boundary. A mixture of skeletal dendrite sizes below the boundary, lathy and skeletal dendrites at the layer boundary, and skeletal and lathy features above the layer boundary. Weld layer is heavily angled

5.1.2.3.2. YZ Orientation

The YZ orientation produced comparatively finer grain features compared to the XZ orientation. Like the XZ orientation, YZ samples contain predominant FA solidification structures with primarily skeletal dendrites with varying lengths that have coarse secondary dendrite spacing. A mixture of both lathy type FA features, and types A, and AF solidification structures such as planar, cellular, and equiaxed structures were located near a weld layer boundary. Figures 57 through 59 display the representative features seen in the YZ orientation.

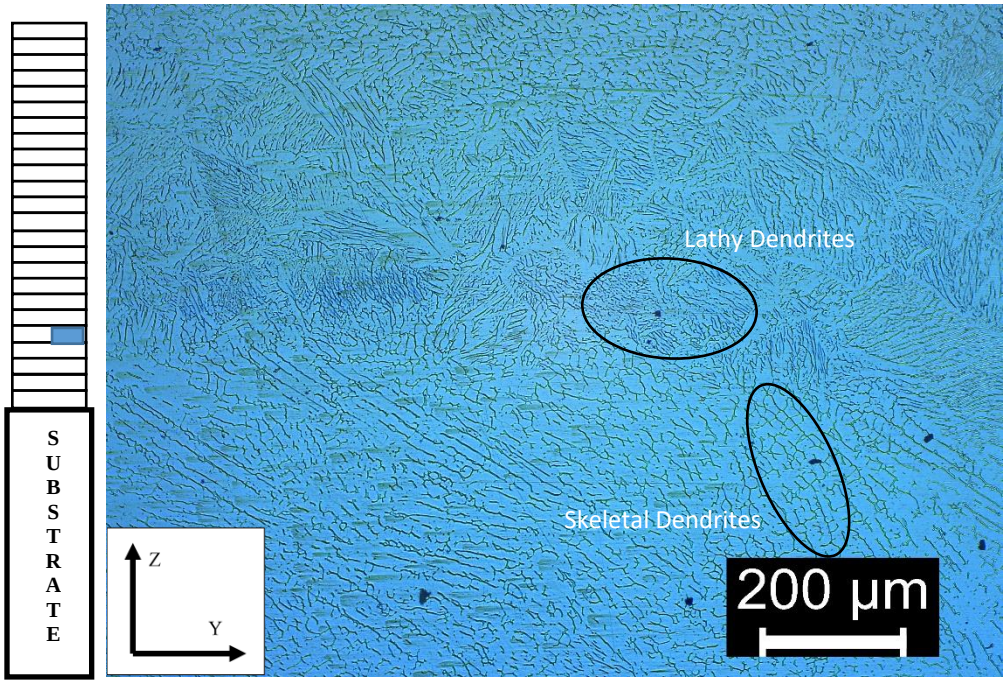

Figure 57: A low power input sample containing primary FA solidification type features at a layer boundary. A mixture of skeletal dendrite sizes below the boundary, lathy and skeletal dendrites at the layer boundary, and skeletal and lathy features above the layer boundary.

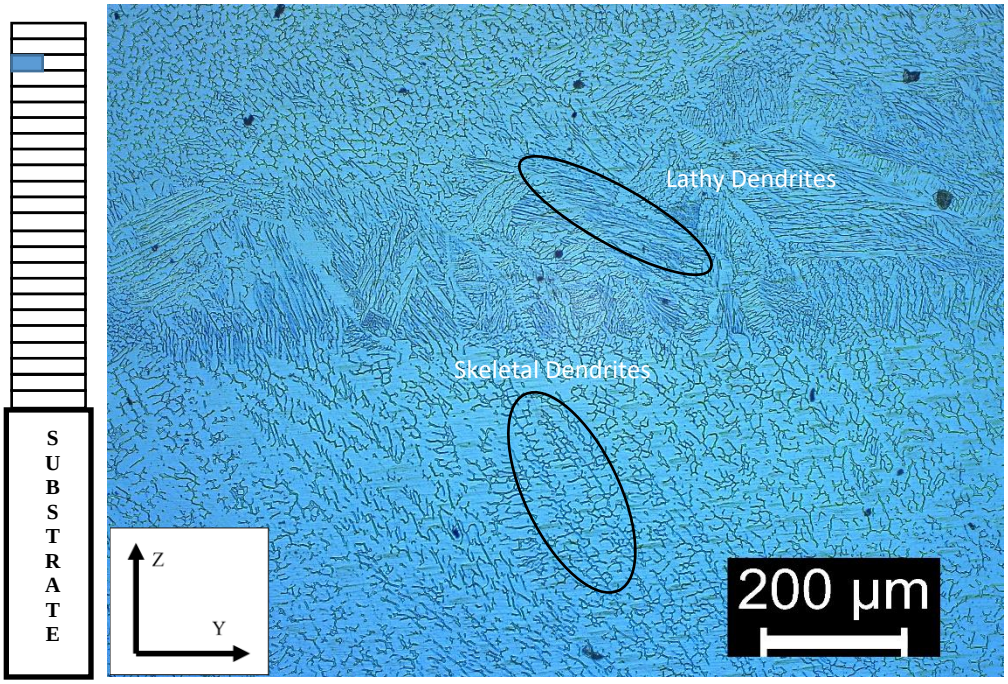

Figure 58: A low power input sample containing primary FA solidification type features at a layer boundary. A mixture of skeletal dendrite sizes below the boundary, lathy and skeletal dendrites at the layer boundary, and skeletal features above the layer boundary.

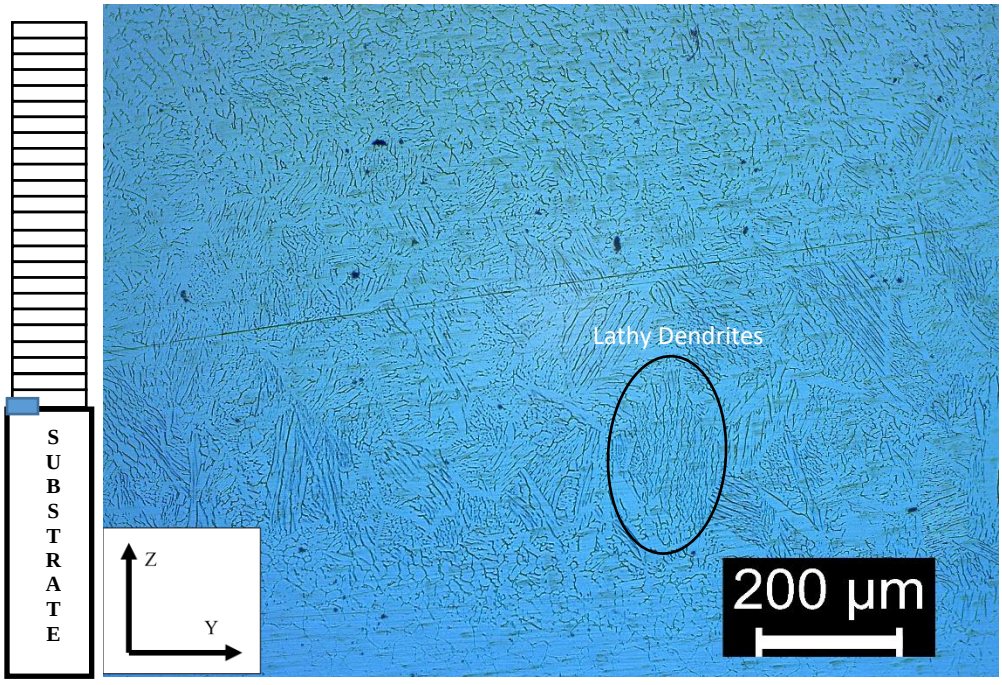

Figure 59: A low power input sample containing primary AF solidification type features at a layer boundary between the bottom layer and the HAZ base metal. Mainly coarse lathy features at the weld boundary and right above layer with some fine skeletal features. Orientation trends generally upwards.

5.1.2.3.3. XY Orientation

The XY orientation produced relatively fine grain features, containing FA solidification structures with scattered skeletal dendrites with coarse secondary dendrite spacing at most locations with little to no type AF or A solidification structures as samples were examined close to the middle of a layer. Figure 60 is an example of the representative features typically seen in the XY orientation

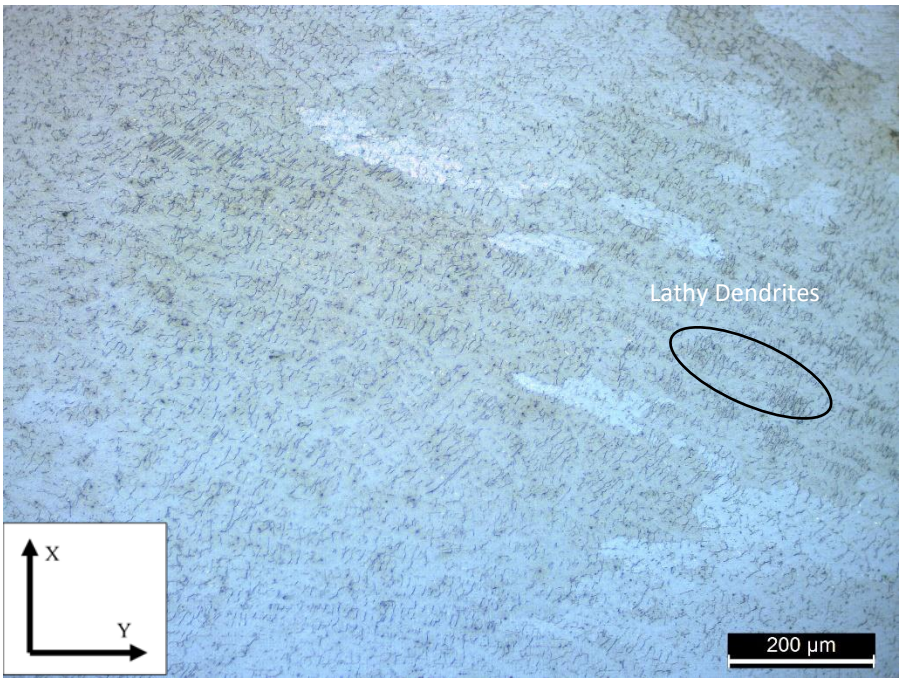

Figure 60: A low power input continuous XY image. Primary FA solidification with scattered coarse skeletal and lathy dendrite features

5.1.2.3.4. Dendrite Spacing

Dendrite spacing analysis was performed using the Leica Application Suite Dendrite Expert Analysis package. Figure 61 below is the result of analyzing at least 4 images that contained enough skeletal or lathy dendrite features to perform between 8 and 50 separate measurements per image using the software. The full list of images used for this software with their measurement spots visible can be found in Appendix A.

The continuous samples all contained relatively coarse features with primary FA skeletal and lathy dendrites. Dendrite spacing for the XZ orientation was seen to continuously increase with decreasing power input with averages increasing from 8.4 to 9.9, and finally and 12.3 microns in length. The YZ orientation followed a similar trend, with dendrite spacing increasing from 9.5 to 10.4, and finally to 11.5 microns in length. The high and medium power inputs also both had the XZ orientation as the orientation that produced finer structures while the XZ orientation was coarser in the low power input. The YZ continuously increased as power input was lowered.

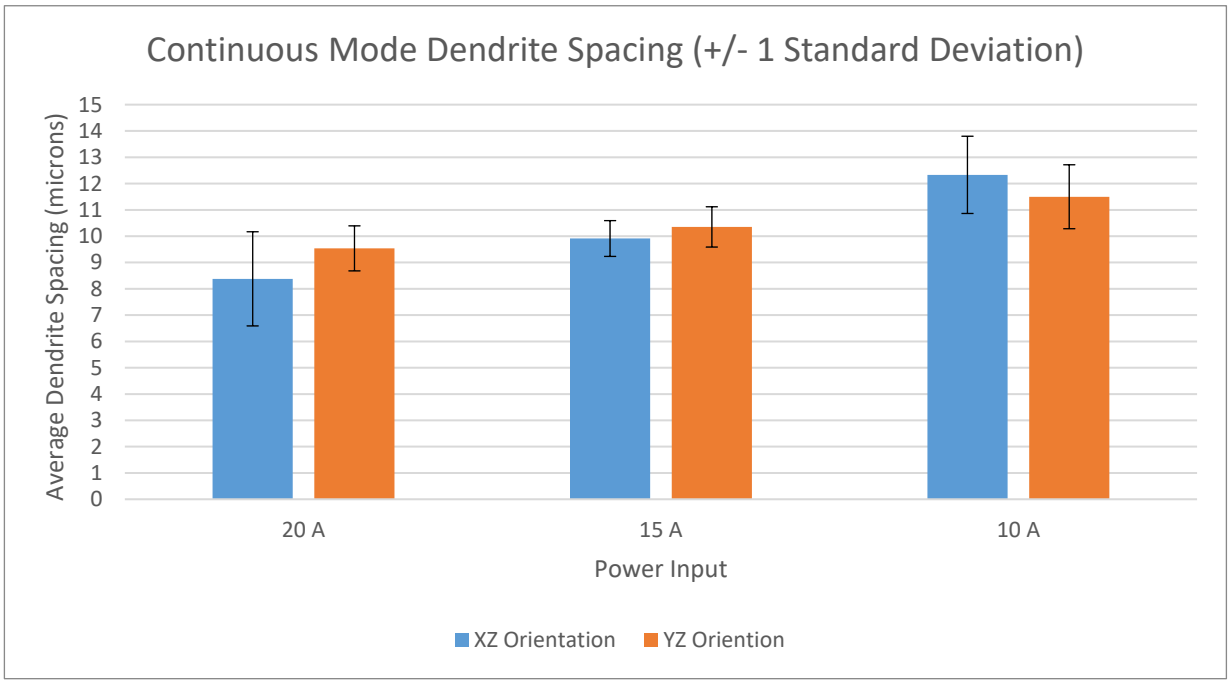

Figure 61: Average Dendrite Spacing for Continuous Mode XZ and YZ samples

5.2. Macrostructure Imaging

Macrostructure imaging was performed for the XZ and YZ orientations for both the dabber and continuous modes and for each power input. Examining samples in the XZ and YZ plains are especially useful as these orientations provide a clear view of grain features that can pass through multiple layers and gives a view on layer structures. Large, multi-layer grain

features are indicators of a structure susceptible to crack propagation and premature failure, especially if multiple large features are similarly orientated, as this can provide an easier path of failure for a final peace. Concerns of mechanical weakness are concerns for most applications, but especially in applications where pieces are subjected to fatigue conditions.

5.2.1. Dabber Mode

Dabber mode overall was highly susceptible to producing large inter-layer grain features in both the XZ and YZ orientations at all power inputs, most of which trend vertically in orientation. The medium power input XZ orientation was particularly susceptible with large grain features present in many of the layers while other power inputs had a higher density of features in the upper half of the XZ samples.

5.2.1.1. High Power Input

High power input samples were highly susceptible to larger grain features and was the only dabber mode power input to display significant amounts of large, orientated grain features with growth between multiple layers in both the XZ and YZ orientations.

5.2.1.1.1. XZ Orientation

Figure 62 below is the XZ orientation sample for the high power input deposition condition and features many large columnar grain features measuring between 1 and 2 mm, oriented with a vertical skew on the far left and right sides of the sample, close to the edge of the sample wall where many of the weld bead pool edges would be formed. Examples of these features are shown in the red circles below.

Figure 62: High power input dabber sample. Several grain features can be seen persistent between 2 or 3 layers with vertical tendencies.

5.2.1.1.2. YZ Orientation

Figure 63 below is a YZ orientation sample for the high-power input deposition condition containing many large granular features seen in the lighter etching phase. The features are relatively large and while many remain within an individual layer or weld bead, some features have growth between two layers. Some of the larger features have a vertical growth direction. Examples of these features are show in the red circles below.

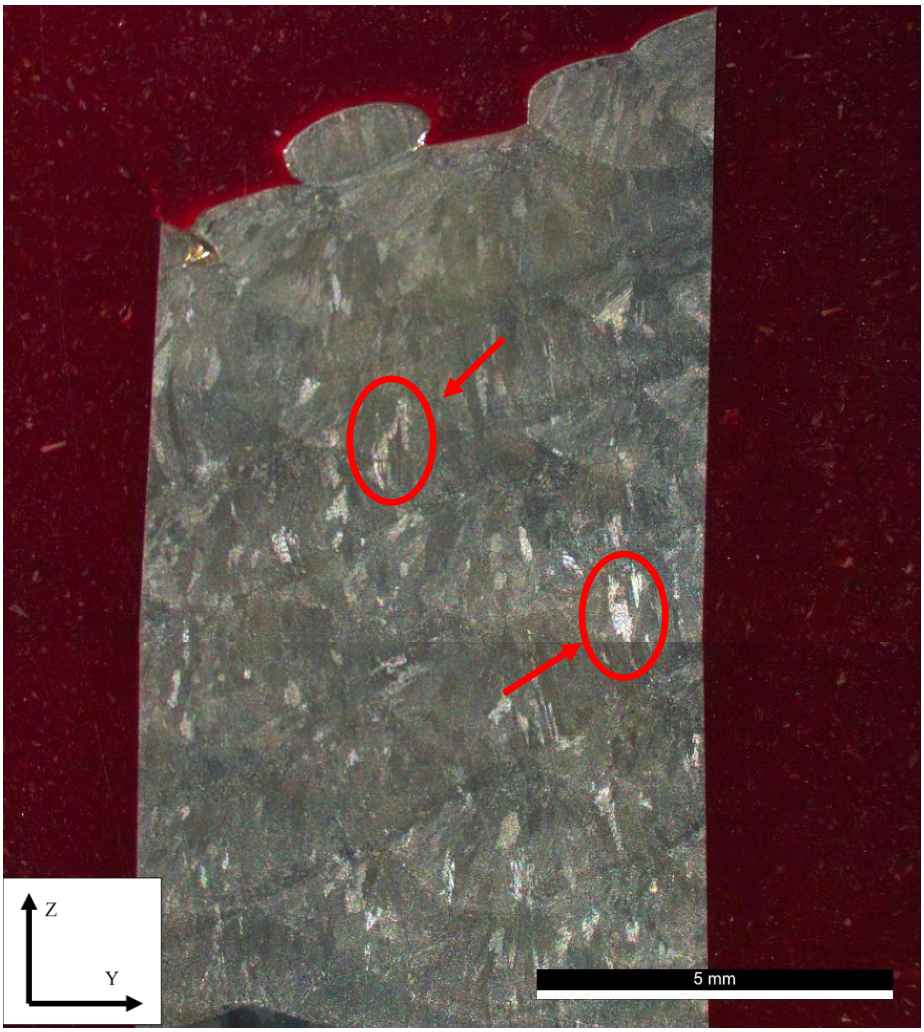

Figure 63: High power input dabber sample. Scattered coarse grain features can be seen persistent between 2 layers with vertical tendencies.

5.2.1.2. Medium Power Input

Medium power input samples appeared to have substantial amounts of columnar grain growth from the middle of the sample through the top of the sample in the XZ direction but had comparatively few large grain features visible in the YZ orientation.

5.2.1.2.1. XZ Orientation

Figure 64 below is the XZ orientation sample for the medium power input deposition condition featuring high levels of columnar grain features with examples of these features

marked by red circles. These features are relatively large as many features are approximately 1-2mm in length and have a vertical skew in the sample.

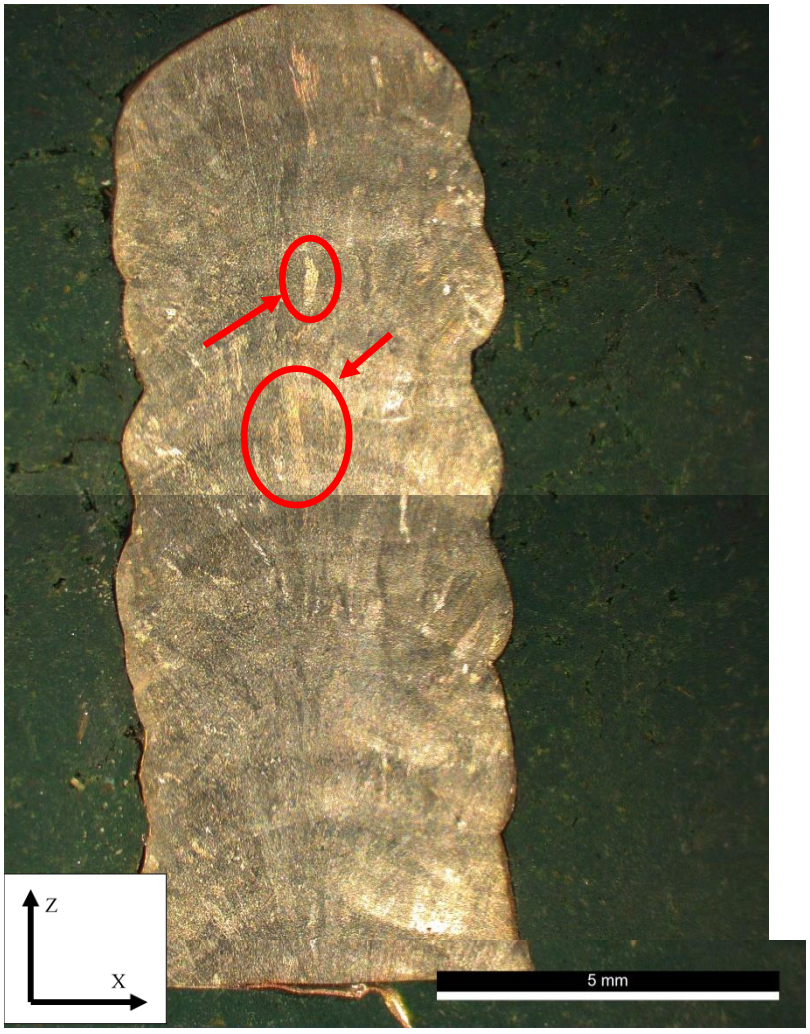

Figure 64: Medium power input dabber sample. Scattered coarse grain features can be seen persistent between 2-3 layers with vertical orientation tendencies.

5.2.1.2.2. YZ Orientation

Figure 65 below is a YZ orientation sample for the medium power input deposition condition containing many several large, but comparative fine grain features that remain within an individual layer or weld bead. The medium power input sample also etched darker than most other samples and had difficulties producing acceptable levels of contrast compared to other

orientations and deposition modes. Examples of the lighter etching phase grain features are shown in the red circles below.

Figure 65: Medium power input dabber sample. Scattered coarse grain features but not growing between multiple layers.

5.2.1.3. Low Power Input

Low power input samples had some of the largest grain features seen on the dabber mode samples, but not quite as many as the medium power input XZ sample. The sample grain features also displayed strong vertical tendencies.

5.2.1.3.1. XZ Orientation

The XZ orientation features some of the coarsest grain features as seen in figure 66. Several grain features extend cross three weld layer boundaries. Examples of these large grain features can be seen marked inside the red circles.

Figure 66: Low power input dabber sample. Scattered coarse grain features can be seen persistent between 2-3 layers with vertical orientation tendencies.

5.2.1.3.2. YZ Orientation

Figure 67 below is a YZ orientation sample for the low power input deposition condition containing many several coarse features that persist through two layers of weld beads, but most coarse features remain within an individual layer or weld bead.

Figure 67: Low power input dabber sample. Scattered coarse grain features but not growing between multiple layers.

5.2.2. Continuous Mode

Continuous mode overall was less susceptible to producing large inter-layer grain features in both the XZ and YZ orientations at all power inputs, with only high-power input samples showing coarse inter-layer features that trend vertically in orientation. The low power input sample is especially notable as the coarse features seemingly have no distinct directionality, nor do they cross weld layers

5.2.2.1.1. High Power Input

High power input samples were the most likely to develop coarser grain features and was the only continuous mode power input to display significant amounts of coarse, orientated grain features with growth between multiple layers in the XZ orientation.

5.2.2.1.1.1. XZ Orientation

Figure 68 below is the XZ orientation sample for the high-power input deposition condition and features several coarse columnar grain features measuring approximately 1 to 2 mm in length, oriented with a primary vertical skew. Examples of these features are shown in the red circles below.

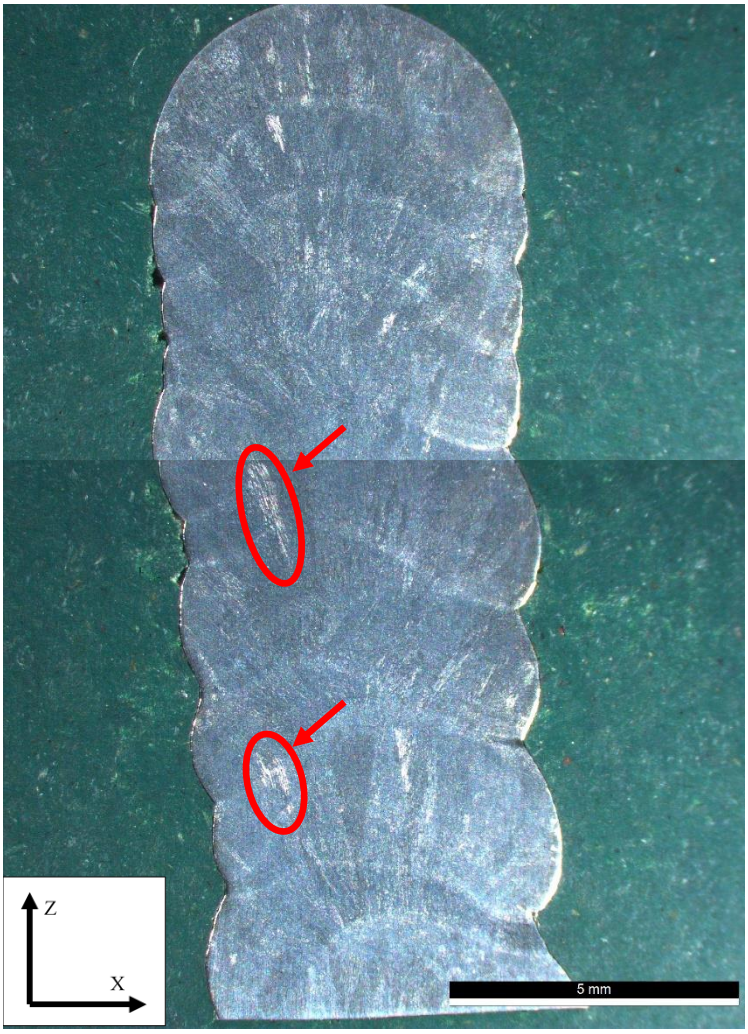

Figure 68: High power input continuous sample. Scattered coarse grain features can be seen persistent between 2-3 layers with vertical orientation tendencies.

5.2.2.1.2. YZ Orientation

Figure 69 below is a YZ orientation sample for the high-power input deposition condition containing scattered coarse features that persist through two layers of weld beads, but most coarse features remain within an individual layer or weld bead and have relatively little directionality in their orientation. The largest feature is shown in a red circle below.

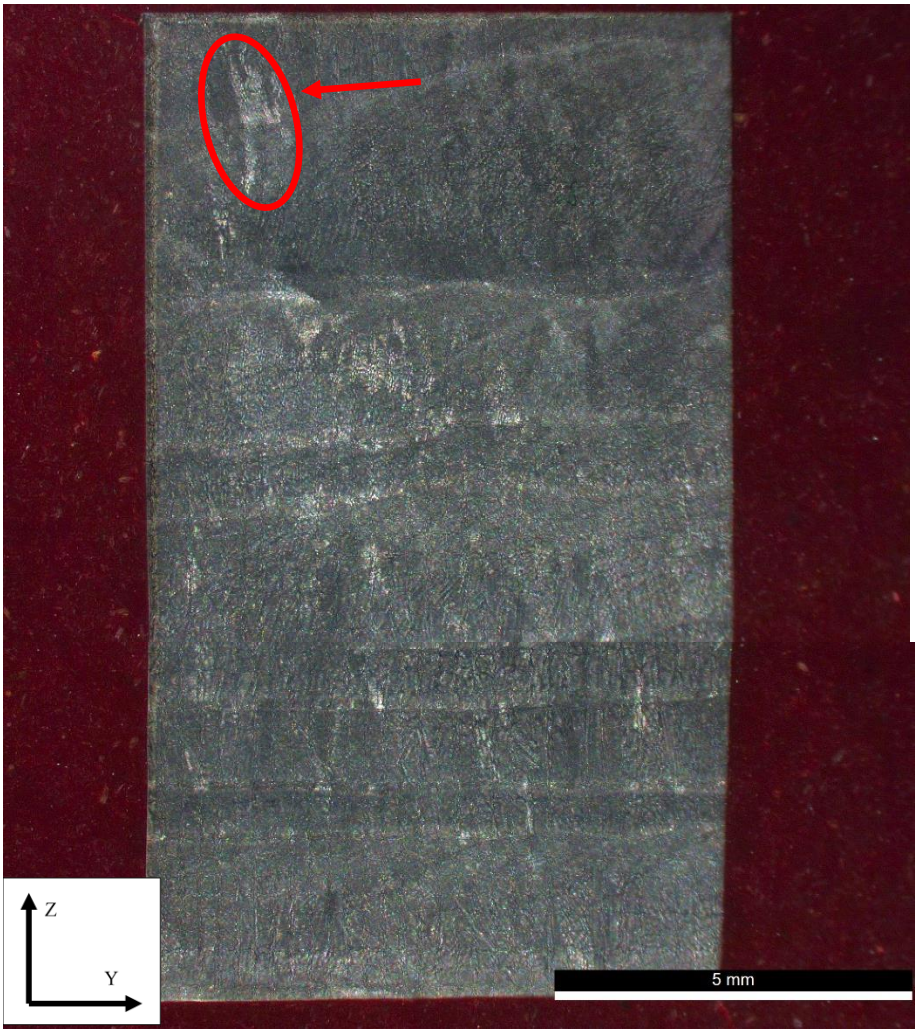

Figure 69: High power input continuous sample. Scattered coarse grain features but not growing between multiple layers.

5.2.2.2. Medium Power Input

The medium power input samples developed coarse grain features, but only saw these grain features grow across multiple layers in the YZ orientation. This was the only continuous mode power input to display significant amounts of coarse, orientated grain features with growth between multiple layers in the YZ orientation. Additionally, the medium power input sample only has 10 layers of weld metal rather than the typical 25 layers, and as a result, has some base in the images. The base metal, other than the HAZ, does not etch with features relevant to the

weld metal above and the weld line that begins the HAZ of the base metal will be marked with a black arrow and text.

5.2.2.2.1. XZ Orientation

Figure 70 below is the XZ orientation sample for the medium power input deposition condition and features several coarse grain features with few crossing weld layers. Examples of these features are shown in the red circles below.

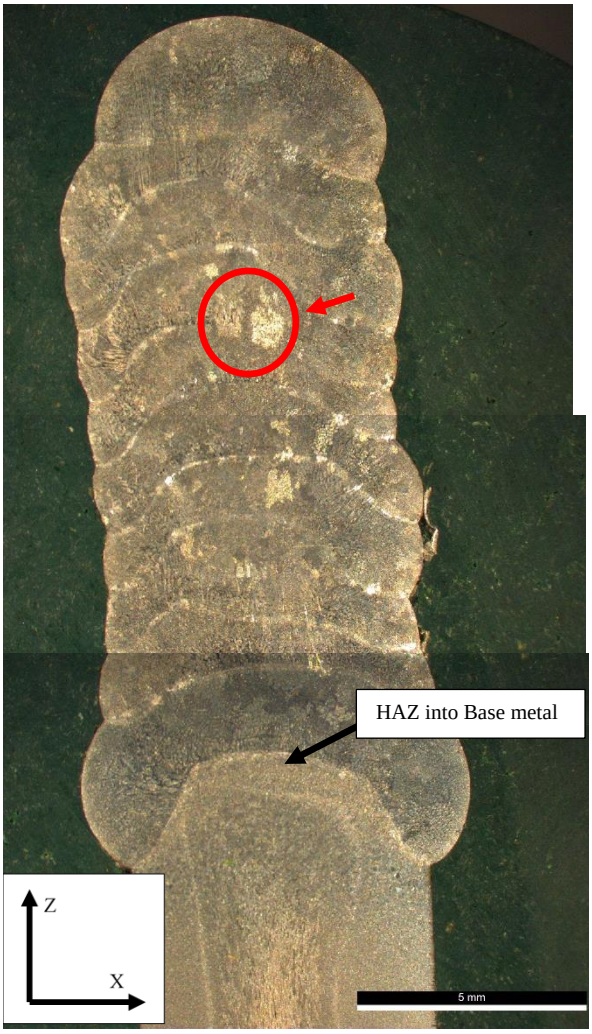

Figure 70: Medium power input continuous sample. Scattered coarse grain features can be seen but are not persistent between weld layers.

5.2.2.2.2. YZ Orientation

Figure 71 below is a YZ orientation sample for the medium power input deposition condition containing scattered coarse features that has only a few especially coarse grains that persist through two or three layers of weld beads, but most coarse features remain within an individual layer or weld bead and have relatively little directionality in their orientation. The largest feature is shown in a red circle below.

Figure 71: Medium power input continuous sample. Scattered coarse grain features with some solidification features between multiple layers.

5.2.2.3. Low Power Input

The low power input samples developed few especially coarse grain features. Additionally, the low power input sample only has 6 layers of weld metal rather than the typical 25 layers, and as a result, has some base in the images. The base metal, other than the HAZ, does not etch with features relevant to the weld metal above and the weld line that begins the HAZ of the base metal will be marked with a black arrow and text.

5.2.2.3.1. XZ Orientation

Figure 72 below is the XZ orientation sample for the low power input deposition condition and features minimal coarse grain features with none crossing weld layers on this sample. Examples of the largest feature that does not cross a grain boundary is shown in the red circle below.

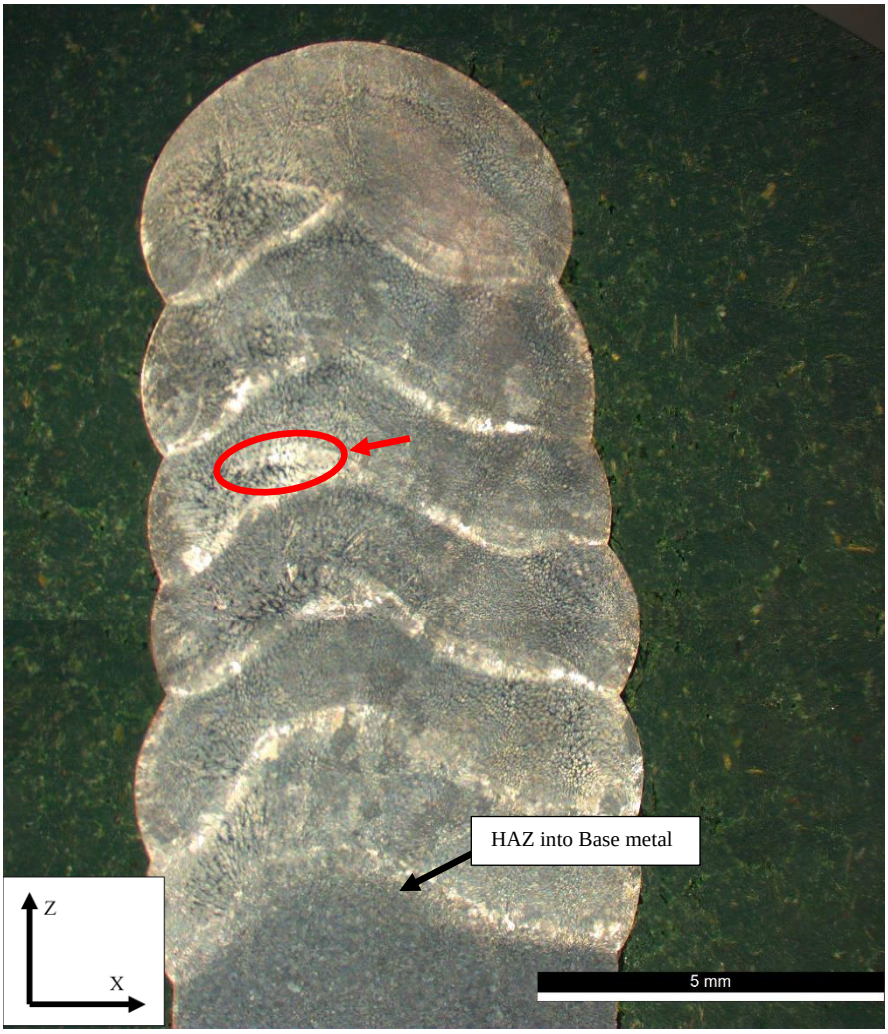

Figure 72. Low power input continuous sample. Scattered coarse grain features can be seen but are not persistent between weld layers.

5.2.2.3.2. YZ Orientation

Figure 73 below is a YZ orientation sample for the low power input deposition condition containing minimal coarse features that remain within an individual layer and have relatively little directionality in their orientation.

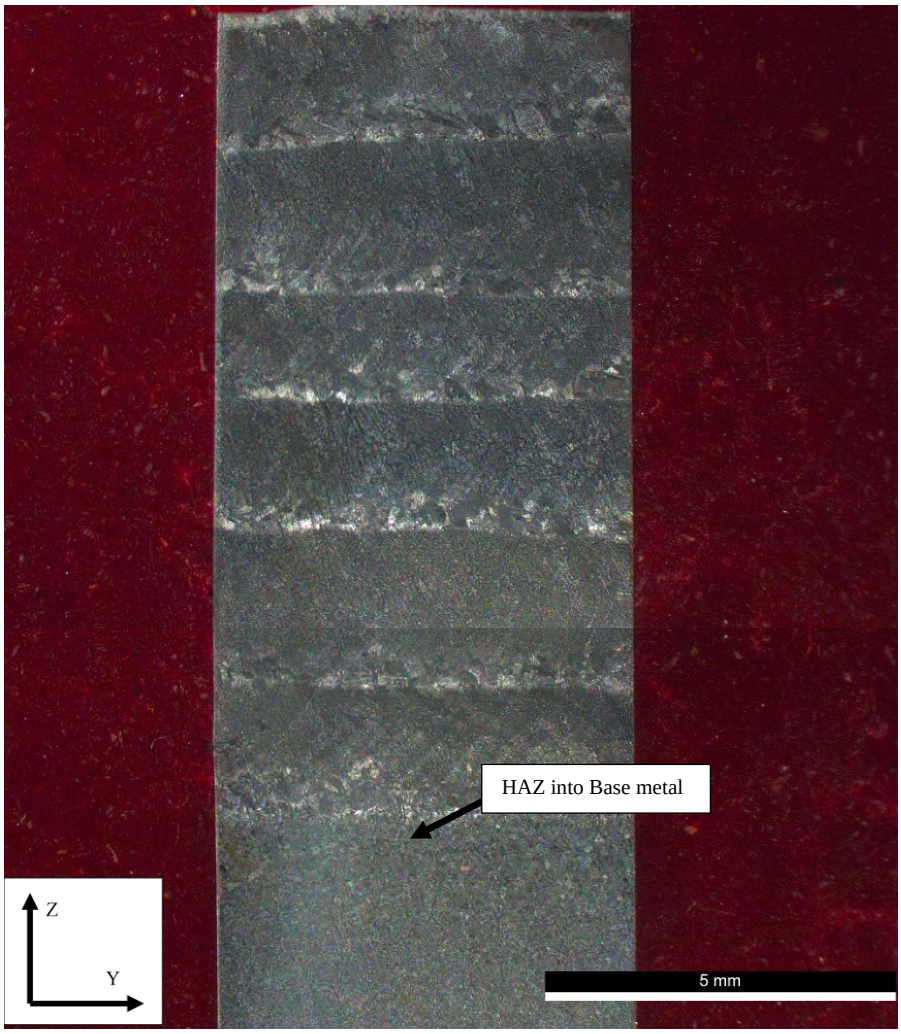

Figure 73. Low power input continuous sample. No coarse grain features that cross layers.

5.3. Fracture Surface Analysis

Only samples from the high-power input and medium power input dabber deposition modes underwent tensile testing, so samples seen in this section are results only from those dabber power inputs. Samples that underwent tensile testing were examined for fracture surface analysis. Samples overwhelmingly displayed ductile fracture modes with EDS analysis displaying nominal composition of the samples being comparable to the original 304L welding wire.

The compositional analysis of the fracture surface was done by EDS point and line scans on areas of interest to determine overall composition, and find locations of possible crack propagation areas due to heterogeneous composition relative to the composition of the overall stainless steel. Figure 74 is an area examined for compositional analysis with EDS spot composition performed on different visible phases in the sample.

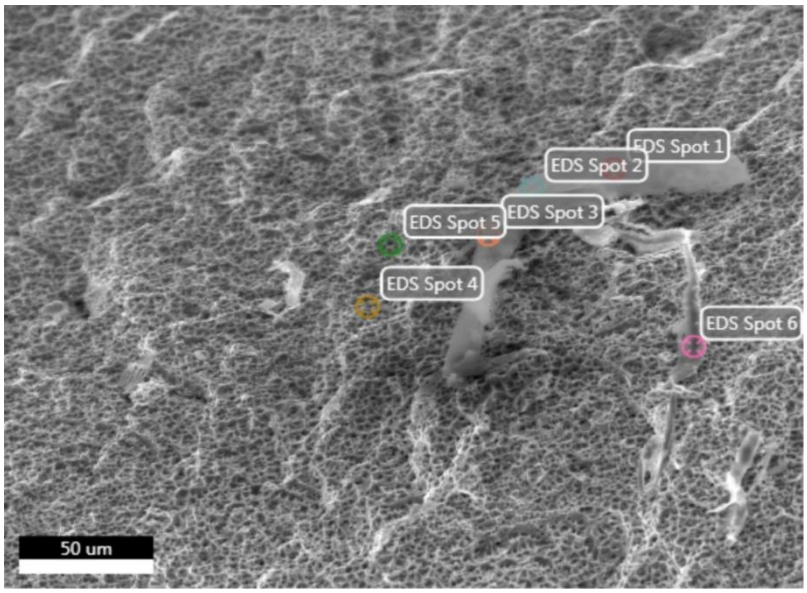

Figure 74. Area used to conduct EDS spot scan of several points of interest for their chemical composition for a high-power dabber mode tensile sample. Points 3 and 4 are marked by red arrows.

Figure 75 below represents the EDS point scan results for points 3 and 4 marked in figure 69 above. Primary components in spots 1-3 are iron carbides that represent a feature that acts as an inclusion in the overall stainless-steel structure seen in spots 4-5.

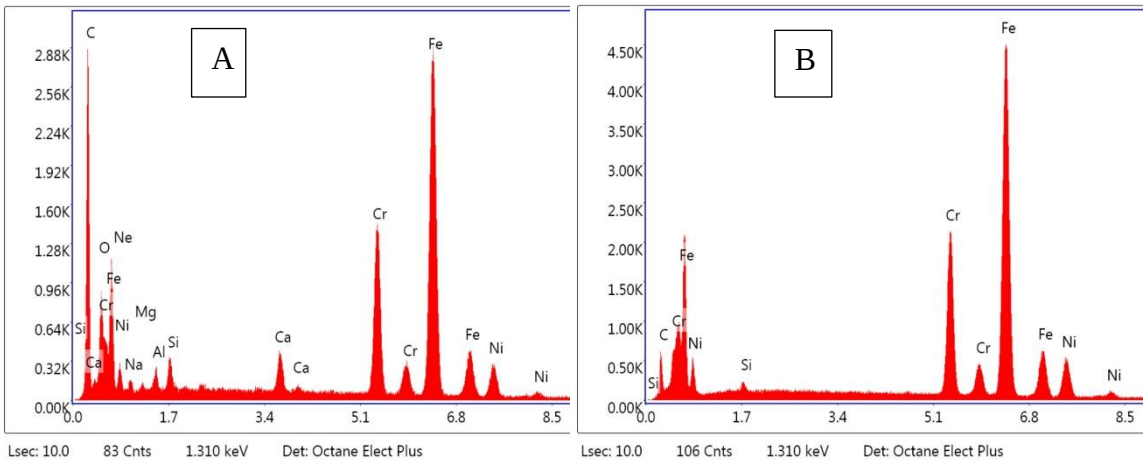

Figure 75. EDAX compositional analysis of EDS spot 3 (left graph, "A") and spot 4 (right graph, "B") from figure 74. Both graphs had areas right of the last nickel peak as no further peaks occurred. The x-axis represents peak location while the y-axis represents the number of counts for a phase.

Table 2 below is an examination of weight percent and the percent error of each component found in spots 3 and 4. In spot 3, carbon and iron are relatively equal in composition, indicating a formation of a type of iron carbide type structure while spot 4 is representative of the 308L stainless composition found throughout the remaining samples.

Table II. Combined Results for the Elemental Composition of Points 3 and 4

Element	Weight %		% Error	
	Spot 3	Spot 4	Spot 3	Spot 4
Carbon	39.88	13.29	8.73	10.58
Chromium	11.57	19.17	2.49	2.24
Nickel	3.78	8.64	5.53	4.37
Iron	32.89	58.39	1.89	1.91
Oxygen	6.06	N/A	11.63	N/A

Figures 76 and 77 are locations displaying typical fracture surface morphologies where the red box labeled "A" in figure 76 is the photographed area for figure 77. Crack propagation for the samples likely occurred internally at points where high levels of carbon formed in grain boundaries that acted as an inclusion in the overall structure, leading to overall failure in void

spaces. Overall, the images below are a representative spectrum of structures seen on all samples, with a predominant ductile failure mode. Some brittle fracture or moderate ductility failure modes are also present in the samples, but in much smaller quantities of the predominant ductile feature set.

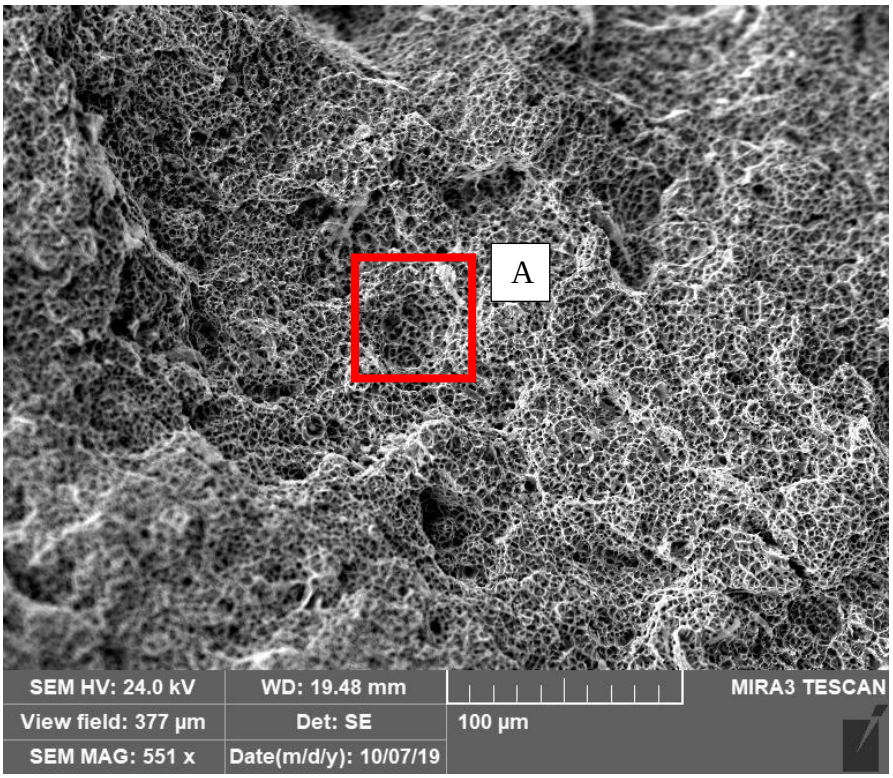

Figure 76. A tensile fracture sample with high levels of ductile failure denoted by the high levels of dimpling features also known as "Honey-comb" type failure surfaces.

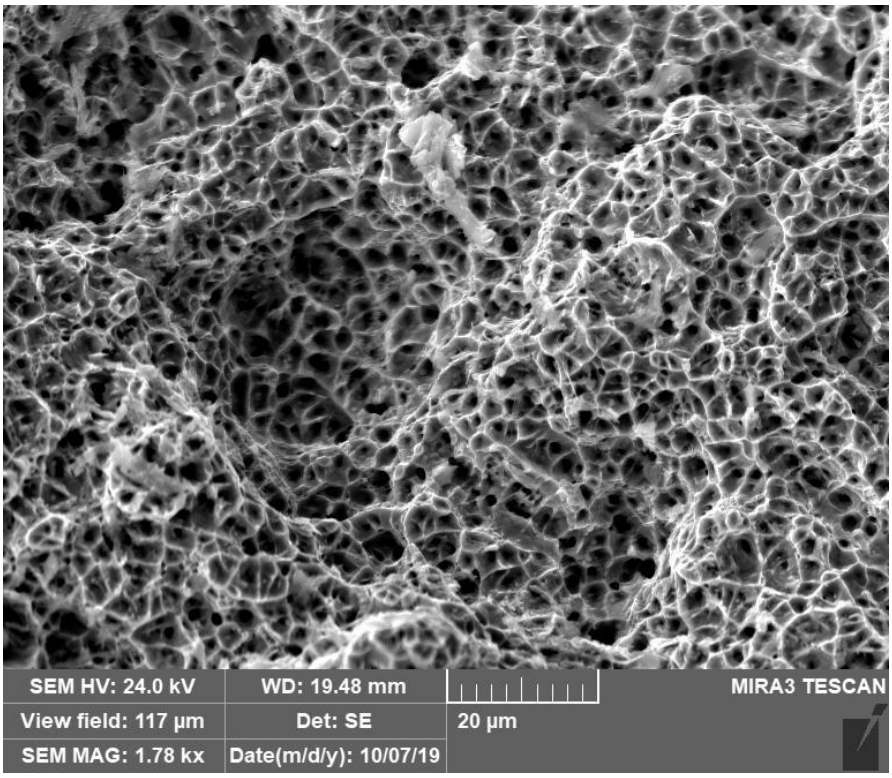

Figure 77. A higher magnification image of area A from figure 76. The dimpling as occurred is predominant and very fine, with most features smaller than 10 µm in diameter.

5.4. Hardness Testing

Collected information on the hardness values when compared to structures seen in the imagery of the micrographs and macrographs shown previously, can provide approximations of bulk material properties such as tensile strength wear resistance.

5.4.1. Microindentation

Microindentation was carried out to determine differences in hardness over the welding layers as microindentation can measure changes over small distances. When combined with macroindentation results, an overall hardness profile for a material can be inferred to estimate the physical properties of a material.

5.4.1.1. Dabber Mode

For the dabber mode, levels of variation were relatively low with values for all power inputs showing similar levels of hardness at the micro-level. Figures 78-79 are the XZ and YZ orientation results for all power inputs.

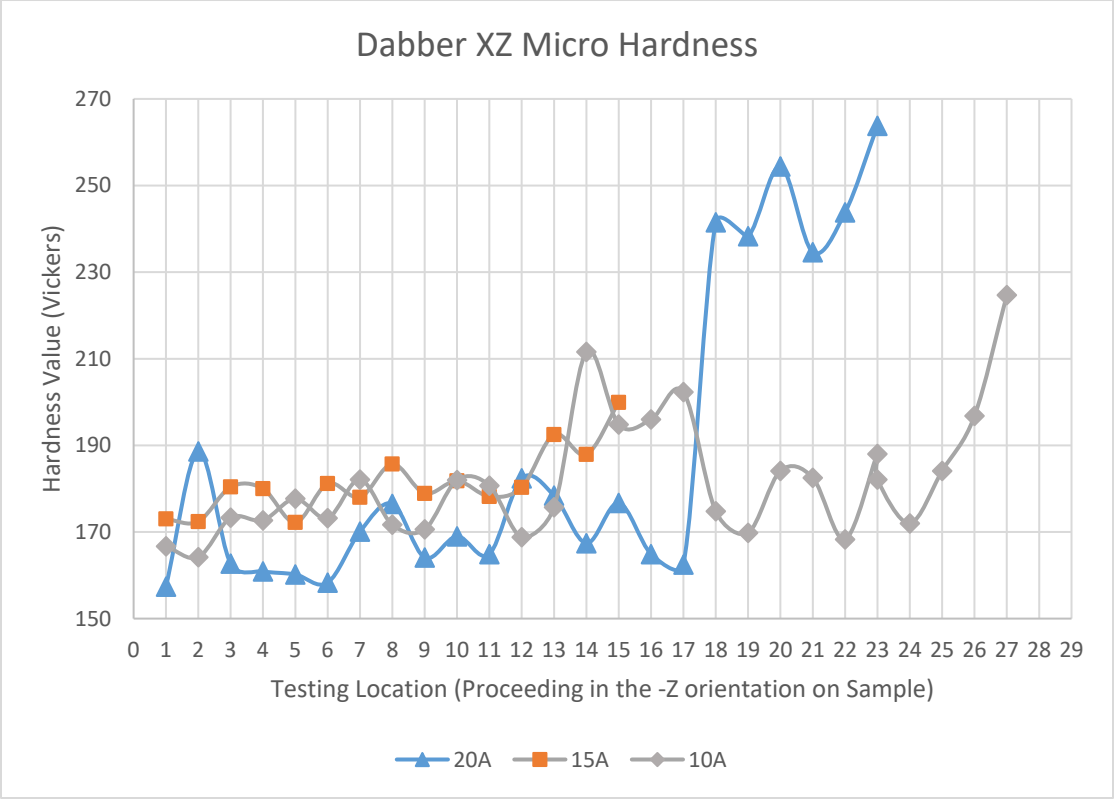

Figure 78. Dabber XZ orientation microindentation results.
Base metal start locations for the power inputs are as follows: High at test location 18, Low at test location 20.

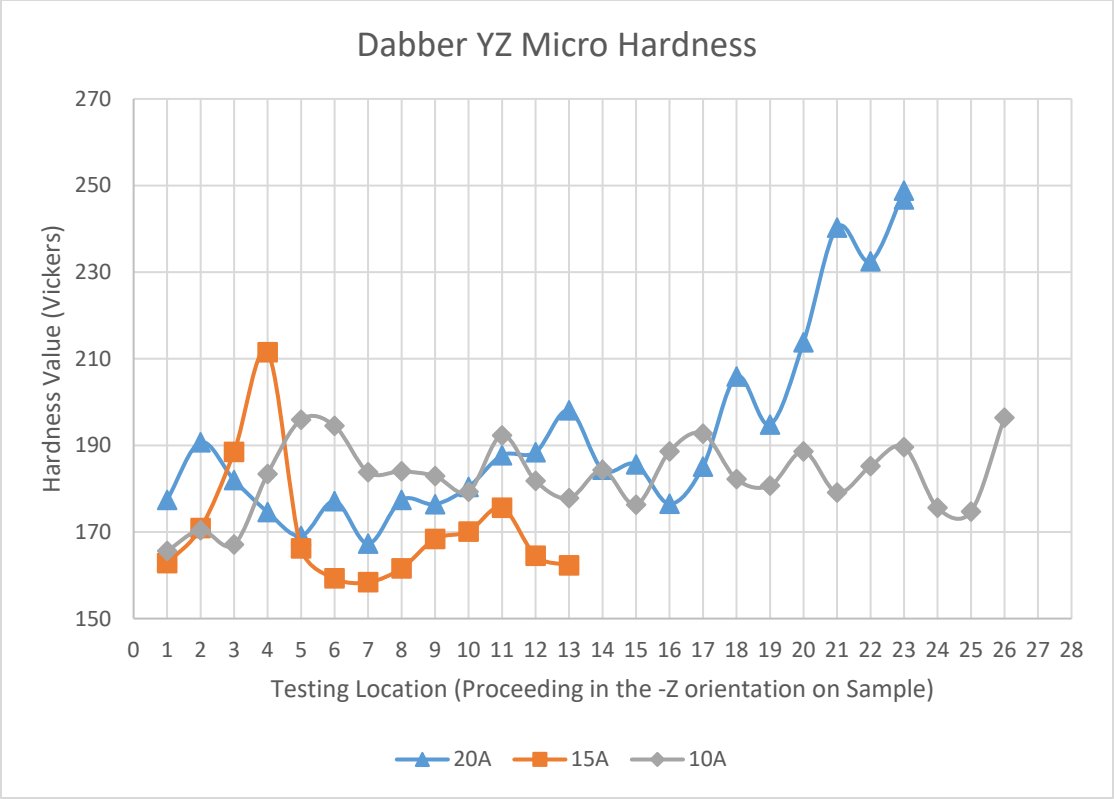

Figure 79. Dabber YZ orientation microindentation results for the high, medium, and low power input. Base metal start locations for the power inputs are as follows: High at test location 20, Low at test location 21.

Figure 80 below is the average hardness and standard deviation for all the dabber samples. The high-power input XZ sample had the overall lowest results when compared to other power inputs or orientations with the medium power input YZ sample also registering results with a nearly identical level of microhardness.

All samples had over 4% coefficient of variation, with the medium YZ in the microhardness testing results having over an 8% coefficient of variation, which translates to the widest variance being approximately ±14 Vickers hardness for the medium power input YZ and lower for the remaining samples.

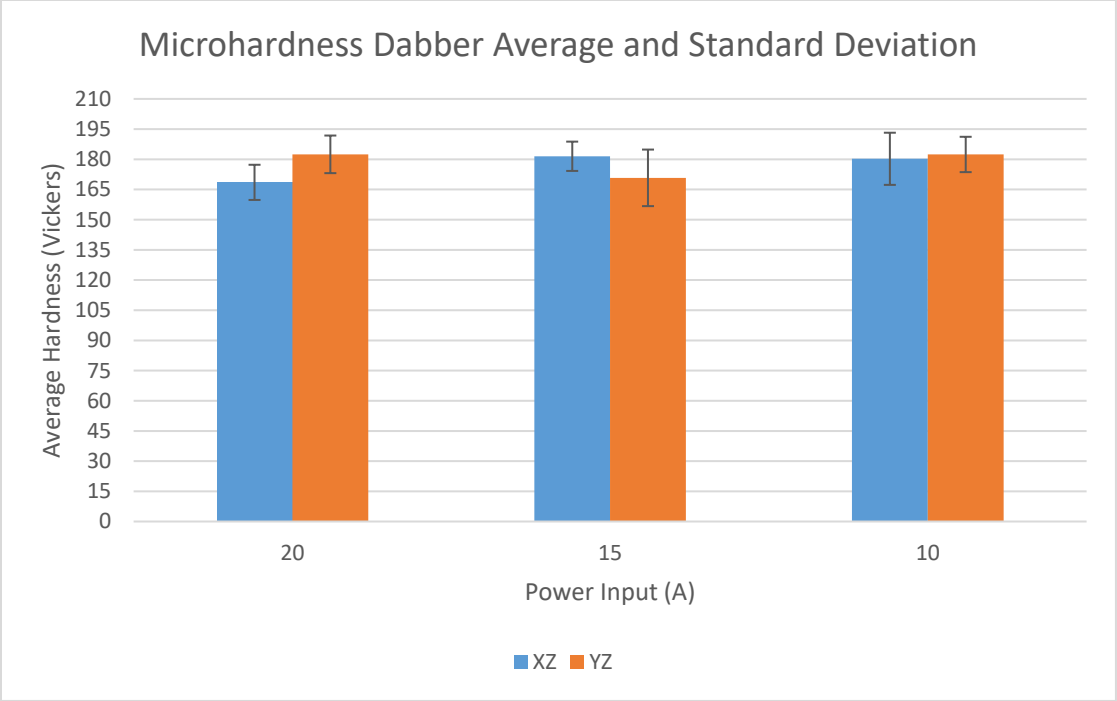

Figure 80. Dabber microindentation average results and standard deviation for the high, medium, and low power inputs.

5.4.1.2. Continuous Mode

For the continuous mode, hardness decreased with the power input for both the XZ and YZ power inputs. Coefficient of variations are comparatively lower than the dabber samples. Figures 81-82 below include the hardness values with the data points taken with samples from the base metal denoted in the caption.

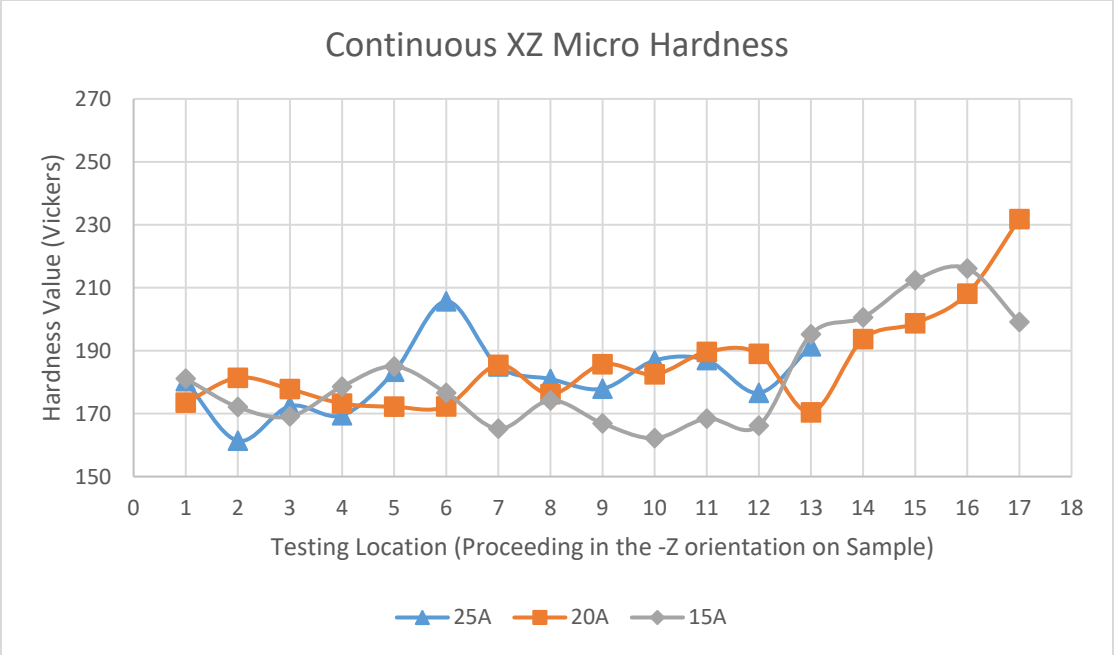

Figure 81. Continuous XZ orientation microindentation results for the high, medium, and low power input. Base metal start locations for the power inputs are as follows: High not shown, Medium at location 14, and Low at test location 13.

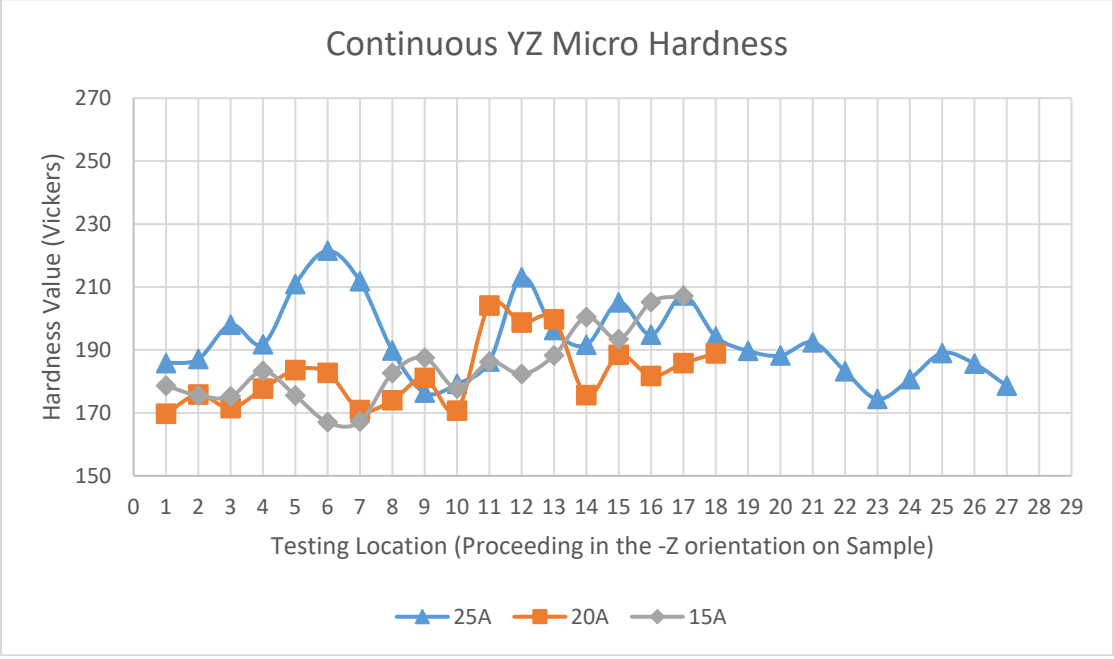

Figure 82. Continuous YZ orientation microindentation results for the high, medium, and low power input. Base metal start locations for the power inputs are as follows: High location 24, Medium at location 15, and Low at test location 13.

Figure 83 below is the average hardness and standard deviation for all the continuous samples. The general trend of hardness decreasing as power input decreases can be seen for both orientations, though the difference between the high and medium power input samples for the XZ orientation is slight.

Almost all samples had over 4% coefficient of variation, apart from the low power input samples. The highest coefficient of variation was the medium YZ again with a 6.17% coefficient of variation, which translates to the widest variance being approximately ±11-12 Vickers hardness for the high and medium power input YZ and lower for the remaining samples.

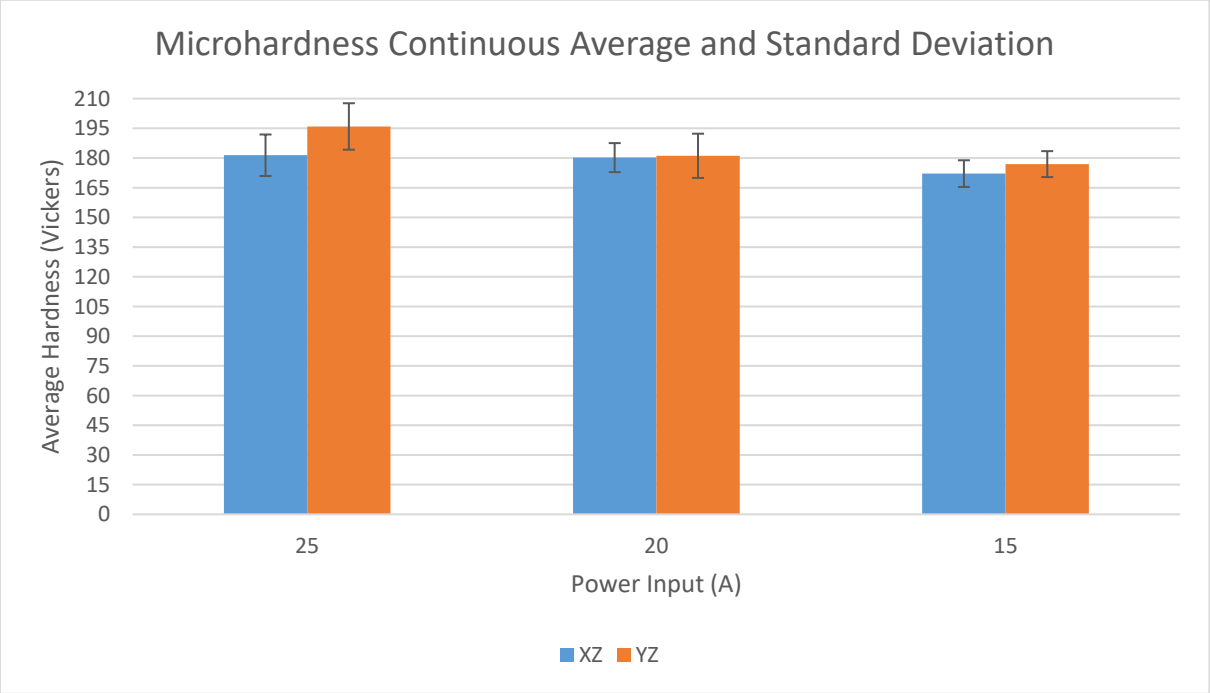

Figure 83. Dabber microindentation average results and standard deviation for the high, medium, and low power inputs.

5.4.2. Macroindentation

Macroindentation was performed to determine the bulk hardness of the material using the Rockwell B scale. Rockwell scales are highly empirical in their results but can be used to read trends of the material without results being sensitive to minor changes in sub-grain structures compared to microindentation testing.

5.4.2.1. Dabber Mode

For the dabber mode, the XZ orientation is higher in both the high and medium power inputs while the opposite is true for the low power input. Figures 84 and 85 below are the results of macroindentation testing including results from the HAZ and base metal. The starting points for the base metal are denoted in the captions.

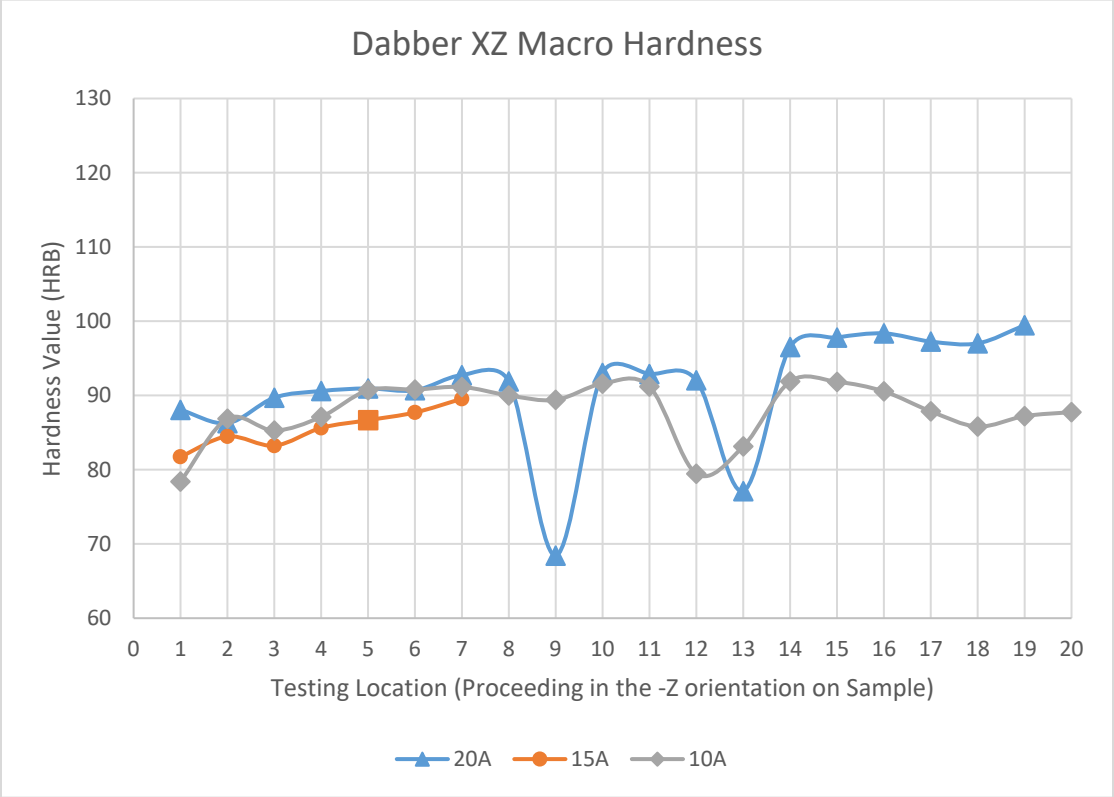

Figure 84. Dabber XZ orientation macroindentation results.
Base metal start locations for high and low power input both begin at location 14.

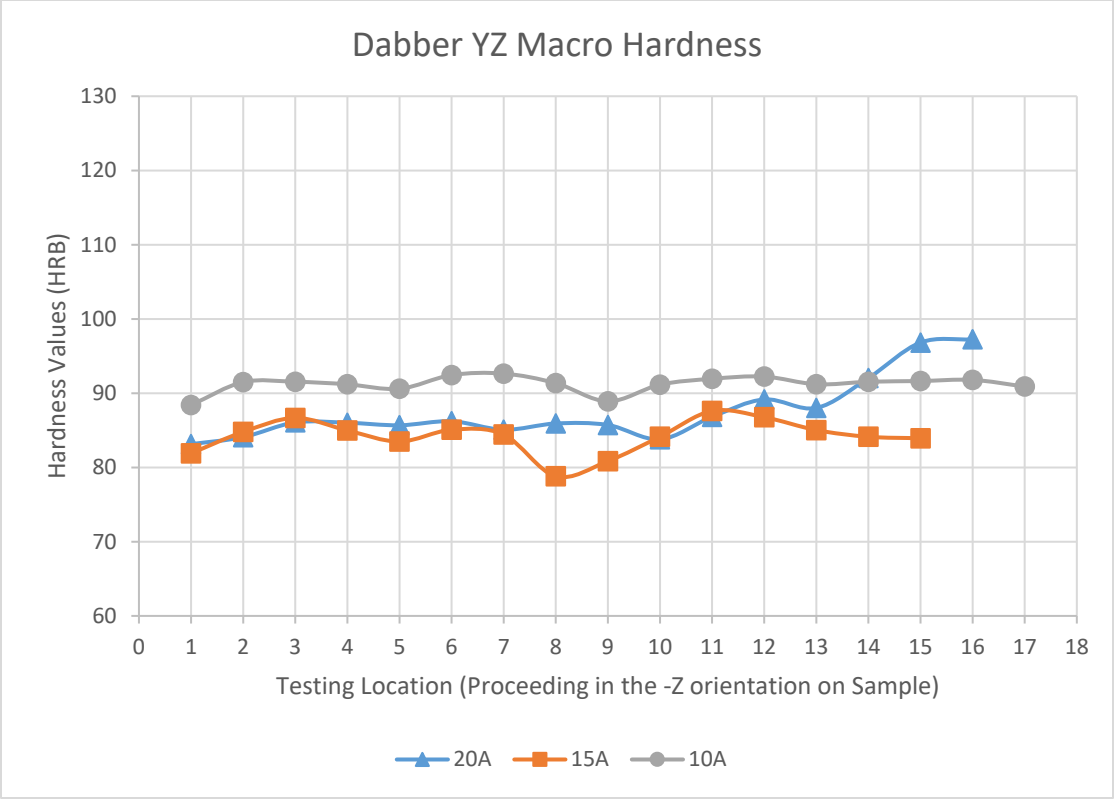

Figure 85. Dabber YZ orientation macroindentation results.
Base metal start locations for high power input begins at location 15, medium at location 13, and low at location 14.

Figure 86 is the average of the results from figures 84 and 85 excluding measurements from the base metal. Averages have a relatively low coefficient of deviation with the XZ high power input sample having the highest at 5.61%. Full table of values for the dabber and continuous results can be found in Appendix C.

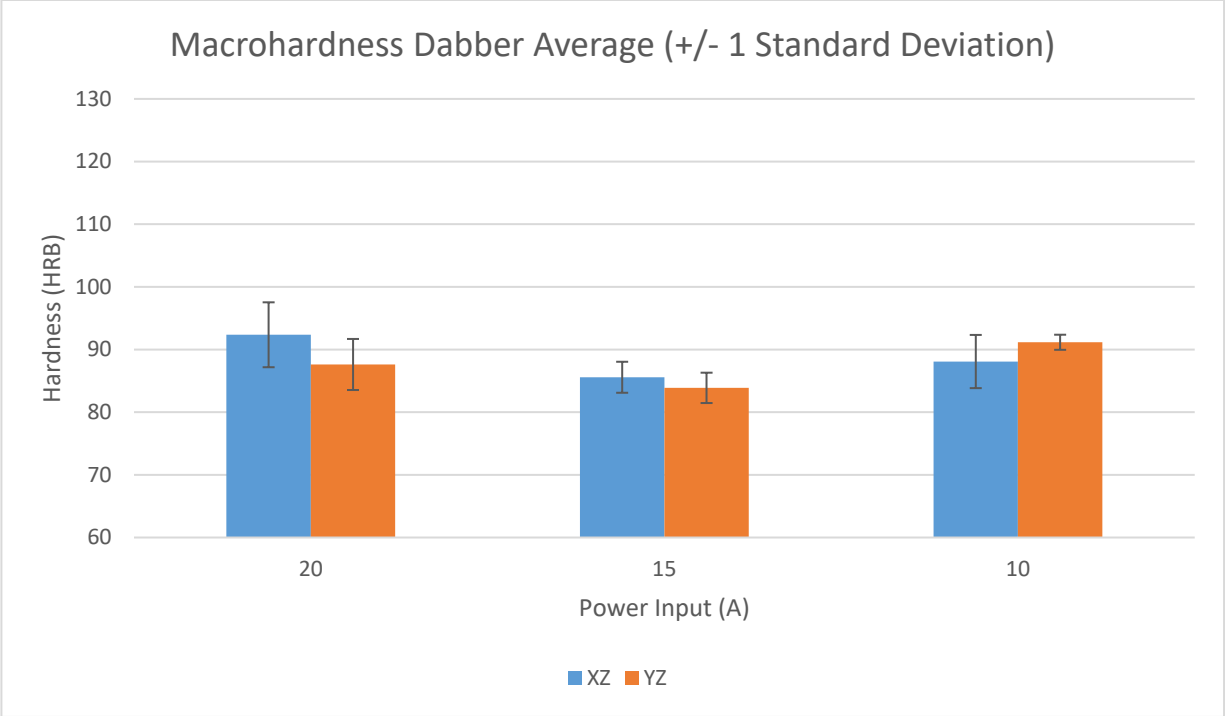

Figure 86. Dabber macroindentation average results and standard deviation for the high, medium, and low power input.

5.4.2.2. Continuous Mode

For the continuous mode, the XZ orientation is higher in all power inputs while the YZ high power input is significantly lower than the all other continuous mode samples. Figures 87 and 88 below are the results of macroindentation testing including results from the HAZ and base metal. The starting points for the base metal are denoted in the captions.

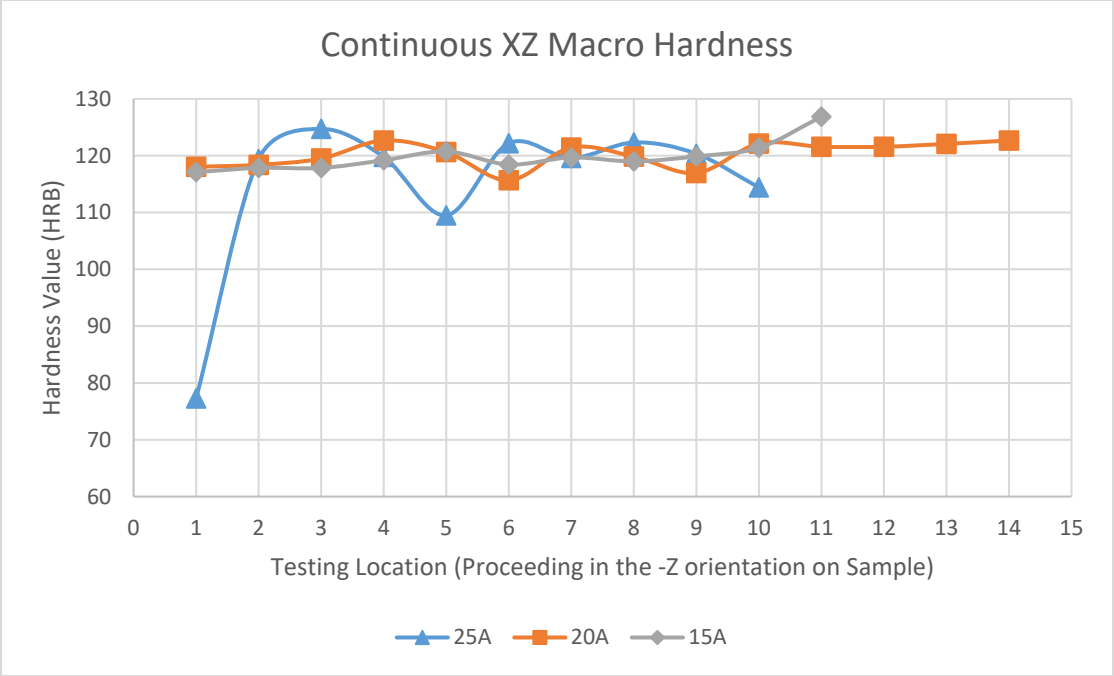

Figure 87. Dabber XZ orientation macroindentation results.
Base metal start locations for high and low power input both begin at location 14.

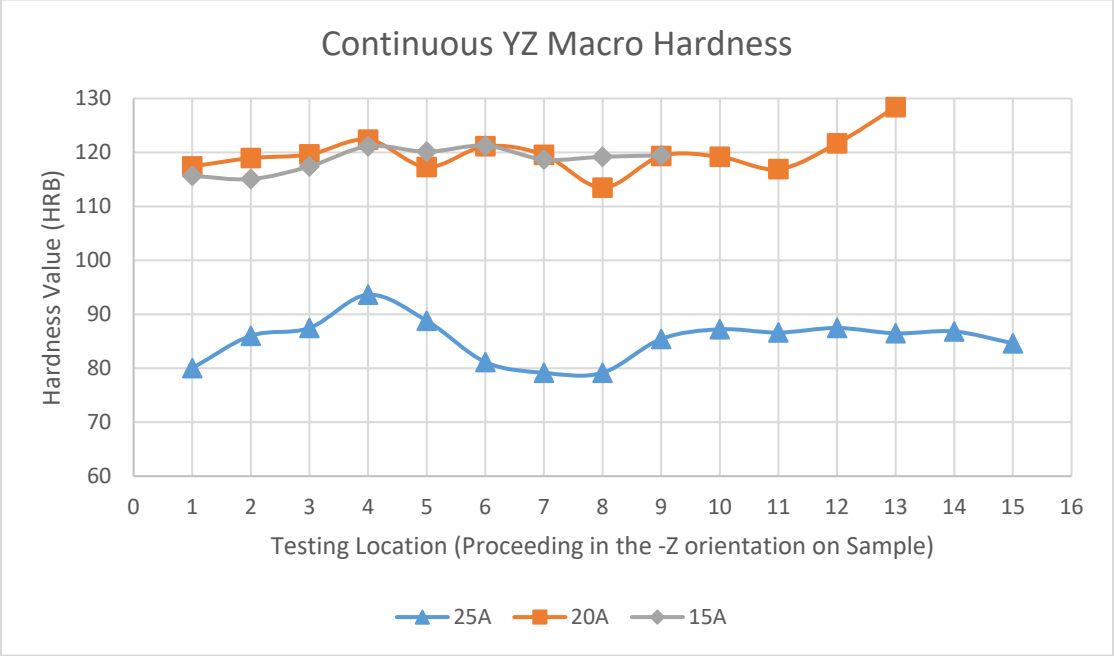

Figure 88. Dabber YZ orientation macroindentation results.
Base metal start locations for high power input begins at location 15, medium at location 13, and low at location 14.

Figure 89 is the average of the results from figures 87 and 88 excluding measurements from the base metal. Averages typically had a low coefficient of deviation with the YZ high power input sample having the highest at 5.29%. Full table of values for the dabber and continuous results can be found in Appendix C.

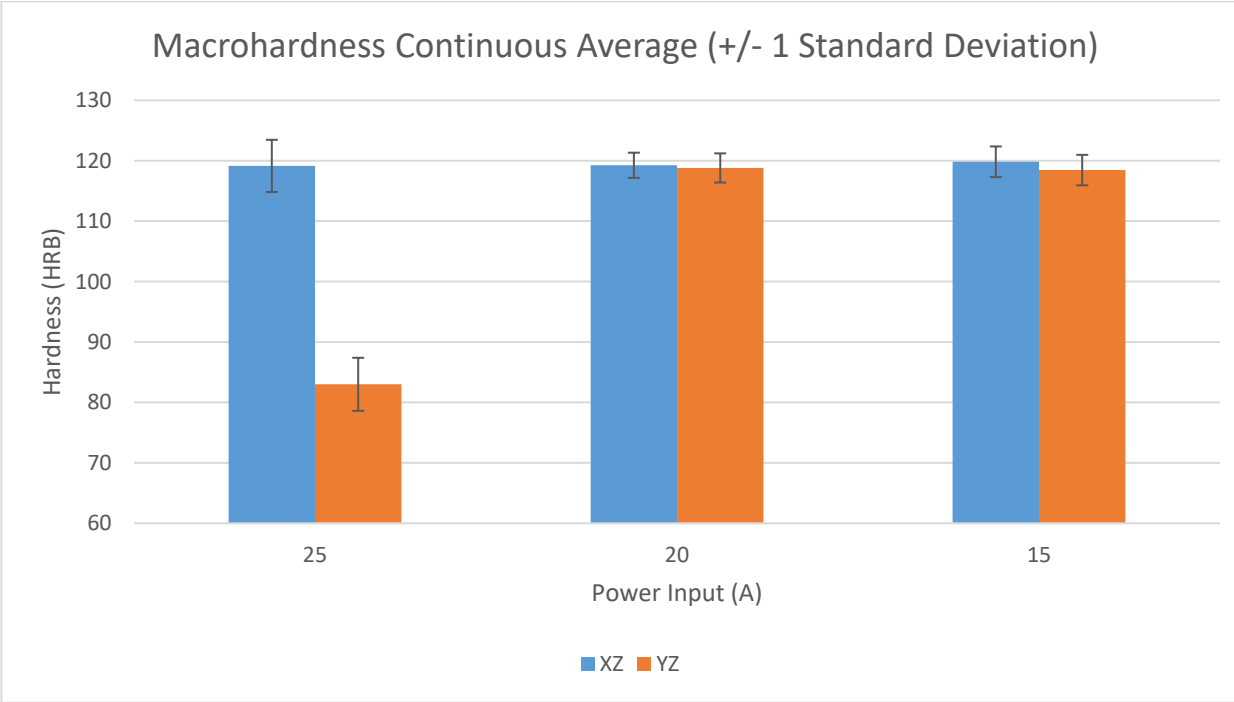

Figure 89. Dabber macroindentation average results and standard deviation for the high, medium, and low power input.

6. Discussion

6.1. Microstructure Imaging

Solidification principles state that initial growth occurring at a fusion boundary is thermodynamically favored to grow epitaxially, but heat transfer mechanics disrupt the equilibrium solidification to become the dominant force as the solidification boundary moves rapidly in a welding environment. In welding, grains tend to grow normal to the solidification boundary, but when grain growth begins, not all grains are oriented favorably relative to the solidification interface. The rapidly moving interface causes grain features that have crystal orientations favorable to the direction of the solidifying metal to grow rapidly. In a continuous weld deposition, the shape and speed of welding affects the temperature gradient *G* and growth rate *R*, which determines the morphology and feature size. However, assuming the welding conditions remain constant at a steady state, microstructure features morphology and general orientation can be predicted for most sections of the weld [20]. Applying these concepts to the dabber deposition mode in PP3D, placing individual weld beads forgoes the steady state solidification due to each deposit in the dabber mode being discreet and nominally round with complete solidification between deposits. Additionally, the deposits overlap with previous deposits both adjacent and in previous layers relative to the current deposit. Under these conditions, the solidification grain growth directions becomes highly varied and have very high rates of growth [14].

Dabber mode had primary type FA solidification that produced significantly finer sub-grain features than continuous mode at every power input and orientation, with the average increase in secondary dendrite spacing being 1 to 4 microns when comparing continuous mode to the dabber mode. Dabber mode high variation in morphology and orientation, with limited

common structures between layers and even within layers can be attributed to the lack of steady state solidification across the welded piece. Variations to this degree are common when the rate of solidification is not done during steady-state welding conditions and during frequent and likely uneven heating cycles as a result of welds that are overlapped repeatedly [20], [29].

Continuous deposition mode also had type FA solidification as the dominant solidification mode and high levels of skeletal and lathy dendrite morphologies occurring throughout the samples. The continuous mode samples were taken to be deposited at a constant or near constant speed, which from a heat flow standpoint, keeps weld pool geometry and solidification rates at temperature gradients highly similar [20]. Additionally, assuming the weld reached the steady state at approximately the halfway point as hypothesized in Huft [14], then solidification conditions would have a higher variability as the process would not have reached the weld's steady state conditions in the first half of the welding conditions.

The medium and low power inputs experienced difficulties in maintaining a constant weld pool that led to these power inputs capable of creating samples that were only 10 and 6 layers, respectively. Under those conditions, steady-state conditions would be more difficult to achieve and exist in fewer areas of the sample. Optimization of these power inputs to create larger 25-layer samples would be an area to explore in future work for comparison on microstructure and mechanical properties.

When comparing to other works, both dabber and continuous modes display similar morphologies and size ranges of the features. While direct comparisons to the dabber mode were not found, work from *Unnikrishnan et al.* [30] provided the closest comparison looking at an individual weld bead at three levels of heat input for a shielded metal arc welding process seen below in figure 90. While the heat inputs were not directly comparable to the heat inputs for the

PP3D system, but the trends can be compared. The results found by *Unnikrishnan et al.* have an opposing relationship to what was seen in the current work where the overall dendrite sizes tended to increase with increasing power input. However, the feature types seen each weld bead are very similar to what can be seen at a fusion boundary between layers of the PP3D system with higher formations of lathy and longer skeletal dendrite formations occurring at or near the boundary.

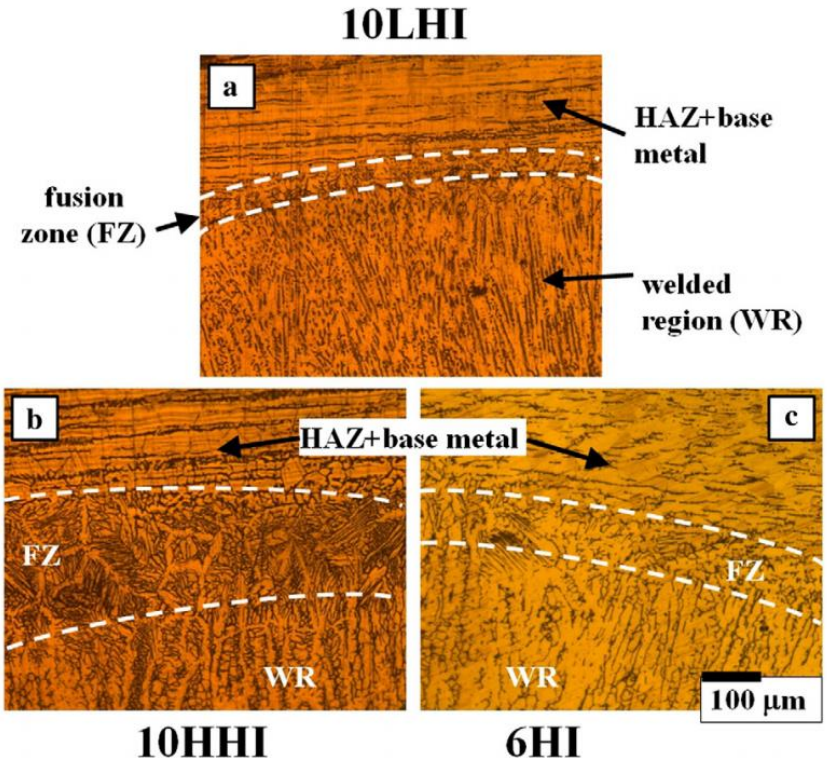

Figure 90. 304L SS Microstructure features seen in *Unnikrishnan et al.* [30] produced by shielded metal arc welding

Most previous works were best compared to the continuous mode of the PP3D system such as the work performed by *Li et al.* [31] and *Ghosh et al.* [32] using wire laser cladding and gas metal arc welding processes, respectively. Results from *Li et al.* [31] can be seen below in figure 91. The wire laser cladding process, which deposits either a metal wire or metal powder onto a compatible substrate. While using different processes, the morphologies and directional

orientations are very similar to those seen in the PP3D system, especially when comparing the orientation of the structures to the continuous mode of deposition. The lathy and skeletal features are all highly oriented in the vertical orientation at the lowest layers and middle of the sample. The sub-grain features become more equiaxed and give way to higher levels of austenite formation near the top of the samples, similar to features seen in the PP3D samples of both deposition modes.

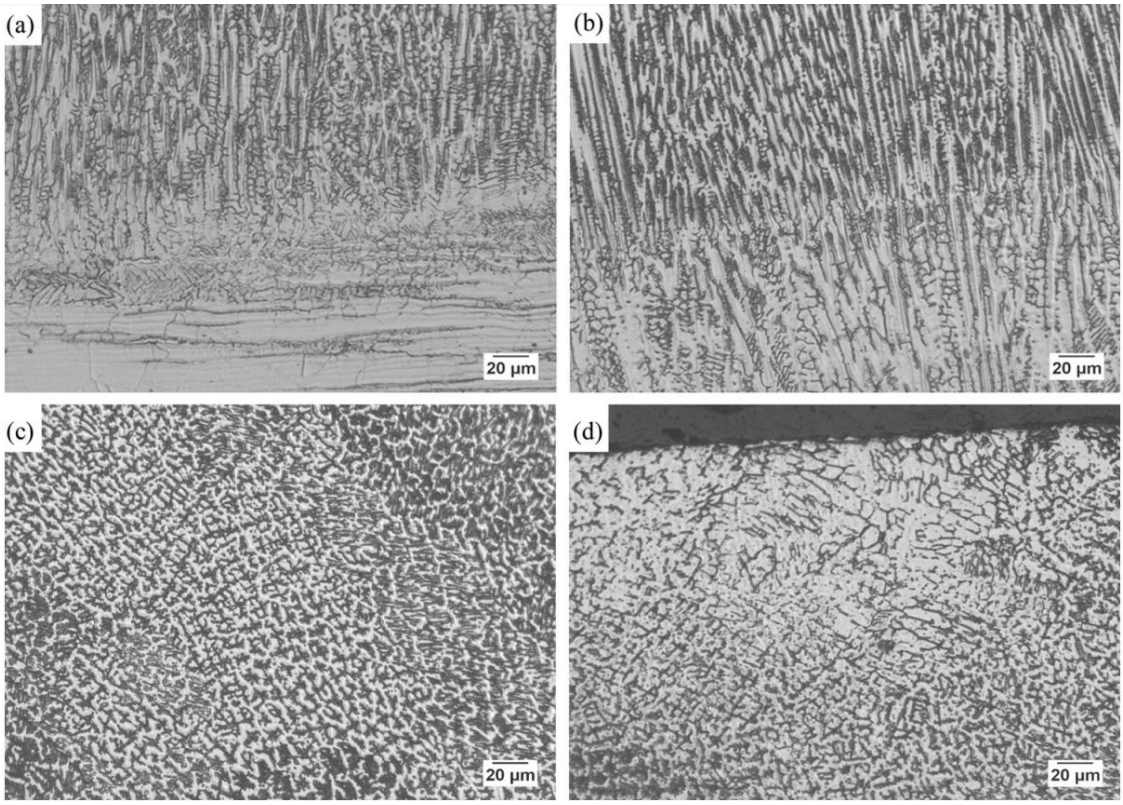

Figure 91. 308L SS Microstructure features seen in *Li et al.* [31] on equivalent YZ orientation at the bottom (a), middle (b), upper third (c), and top (d) from a wire laser cladding process.

Looking next to results seen in *Ghosh et al.* [32], the gas metal arc deposition methodology was tested using two different heat inputs with results displayed in figure 92 below. The relationship seen in their results showed an increase in overall size of the dendrites and few dendrites occurring in the higher heat input when compared to the lower heat input. PP3D

samples are not in agreement with those findings however, with overall secondary dendrite spacing and thus size of the dendrites to increase with decreasing power inputs.

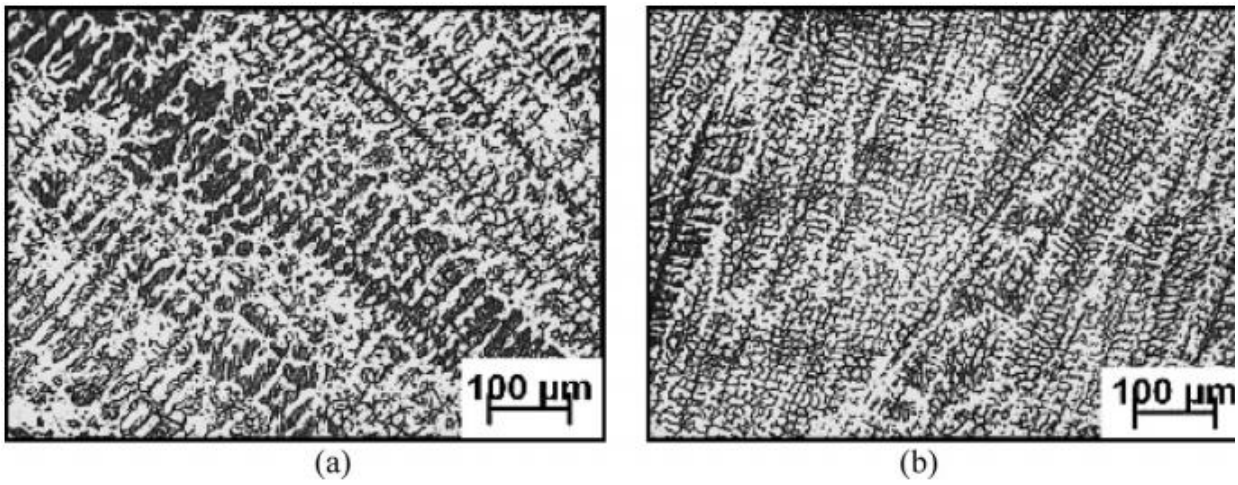

Figure 92. 308L SS microstructures from *Ghosh et al.* [32] produced by gas metal arc welding (GMAW) which had a "high" heat input in image (a) compared to a "Low" heat input in image (b)

Some limitations of measuring secondary dendrite arm spacing using the Dendrite Expert software is a combination of limits on the software when examining the dominant morphology of the sample. The software's manual measuring mode limits dendrite measurements to dendrites no smaller than with 3 arms, which eliminates the measurement of relatively fine equiaxed dendrite structures if that feature is dominant in a section of the sample. Additionally, if the morphology of a sample has features that are predominantly cellular, planar, or dendrite arms that are not easily countable, the software cannot measure these features and becomes guesswork on the operator. These issues are not to exclude the value of that data, but to explain limitations on accurate measurement, and recommended for use in addition to other testing methods.

6.2. Macrostructure Imaging

Dabber mode was highly susceptible to the formation of coarse, columnar grain features, especially in the high and low power input samples. Due to the heat transfer and solidification rates seen in discrete weld beads, solidification would have grain growth orienting towards the solid/liquid interface that solidified from the outside to the inner center of the bead. The center of

the weld pool would cause grains to grow towards the top of the weld bead, likely causing the large columnar grains to grow with a near vertical orientation [18], [20].

Input power setting had a significant effect on the growth of vertical columnar grains. Examining the settings as described in table 1, the high and low power had the highest total heat input into the sample. During the dabber deposition mode, the welding torches are immobile during deposition rather than traveling as seen in a continuous weld environment. While placing discreet weld beads, the overlaps with the previous bead to the side and below the current bead partially melt areas of the previous layer. Where this occurs, solidification that had a vertical growth orientation can potentially cause growth to continue in a similar orientation. The dabber mode's susceptibility to these large inter-layer columnar grains could be caused from the rapid localized heating of the metal to melt or be heated to near melting temperatures and allow for solidification across layer boundaries that were previously solidified [15], [18], [20].

The macroimaging results do not completely agree with the mechanisms seen in the microimages for dabber mode, as the micrographs displayed signs of grain refinement at a sub-grain level but allowing coarse columnar grain features to appear at a macro-level. The likely cause of these columnar, vertical grains is likely due to the intended function of the dabber mode being stationary creation of overlapping weld beads, which during the solidification in the overlapped section allowing growth to occur vertically across layer lines. Further the time that the dabber mode maintains a molten pool is shorter, leading to a rapid cooling of the subgrain structures, which at a micro level creates the fine features seen in the dabber mode and would simultaneously limit grain growth in each weld pool if in isolation. Placing the overlapping weld beads, especially the weld beads in the layer above a previously deposited layer, involved

melting some previously deposited metal or making a HAZ of the nearby metal, leading to more time for sub grain and overall grain growth to occur.

Large columnar grains are common occurrences in many materials beyond stainless steels and is commonly seen in titanium alloys. Many previous works examine reducing the occurrence of these columnar grain structures through manipulation of alloying components [33], or through manipulation of mechanical refinement of the grains such as inter-pass/inter-layer rolling or machine hammer peening [8], [34]. While no work involving plasma arc welding processes was found for comparison, similar work involving wire and arc additive manufacturing were found. Most processes that use austenitic stainless steels using gas-metal arc welding processes (such as gas-tungsten arc welding) using stainless steel achieved similar results as the PP3D system's dabber deposition mode by using a continuous deposition mode[35], [36].

Examples from *Chen et al.* [35] and *Yilmaz and Ugla* [36] can be seen in figures 93 and 94 below, respectively. While both processes used gas-tungsten arc welding processes to create their specimens *Chen et al.* used 316L SS while *Yilmaz and Ugla* used 308 SS, both of which are austenitic stainless steels similar to the 308L SS used by the PP3D system. *Chen et al.* in figure 93 has large columnar grain features occurring throughout the sample with many occurring through two layers with vertical growth directions. This is similar to the coarse grain features seen in the PP3D system. One point to note is the size scale of the sample, which has a much larger sample with more coarse grain features than the current work.

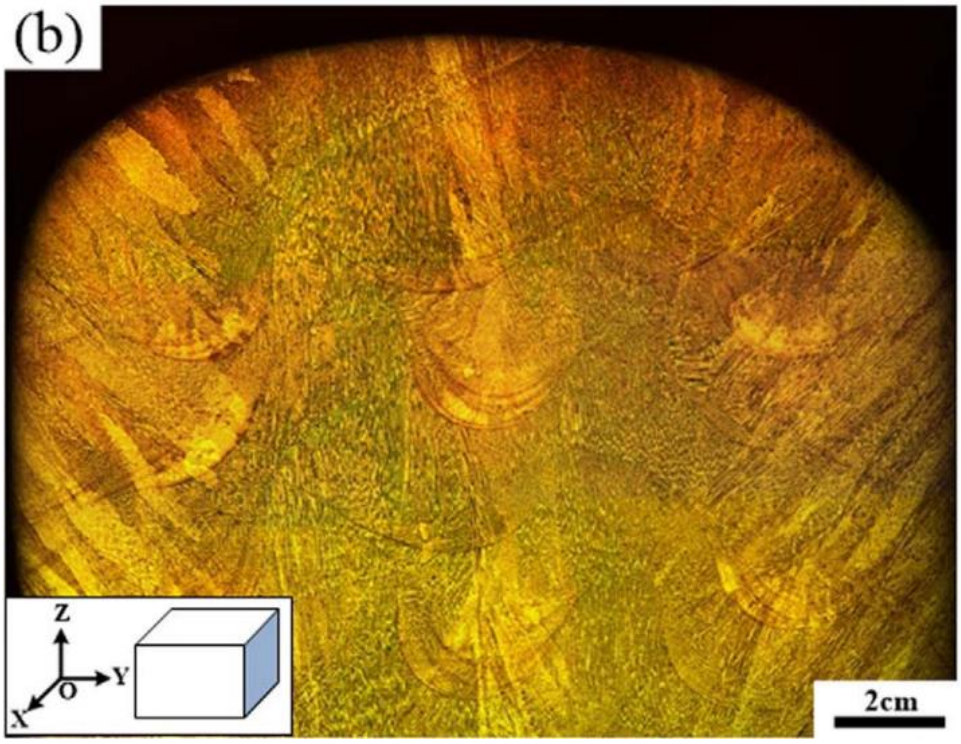

Figure 93. Macrograph from *Chen et al.* [35] displaying large columnar grains in a 316L SS produced from a gas-tungsten arc weld system

Looking next to *Yilmaz and Ugla* [36], the samples made in this work were produced by a gas tungsten arc weld system with the 308 SS alloy system and with a scale more closely related to the current work. The columnar grain features seen in the previous work are of a comparable size to those found in the current work or considerably smaller in some cases. The methodology that was used in both *Chen et al.* and *Yilmaz and Ugla* are more similar to the continuous mode in PP3D system, but with only one arc producing torch. Direct comparisons to the continuous mode yield results that show significant improvement of reducing occurrences of columnar grain features over other methodologies. While not reducing the occurrence of coarse grain features, the continuous mode appears to have reduced the tendency of these features to grow in specific orientations or between weld layers.

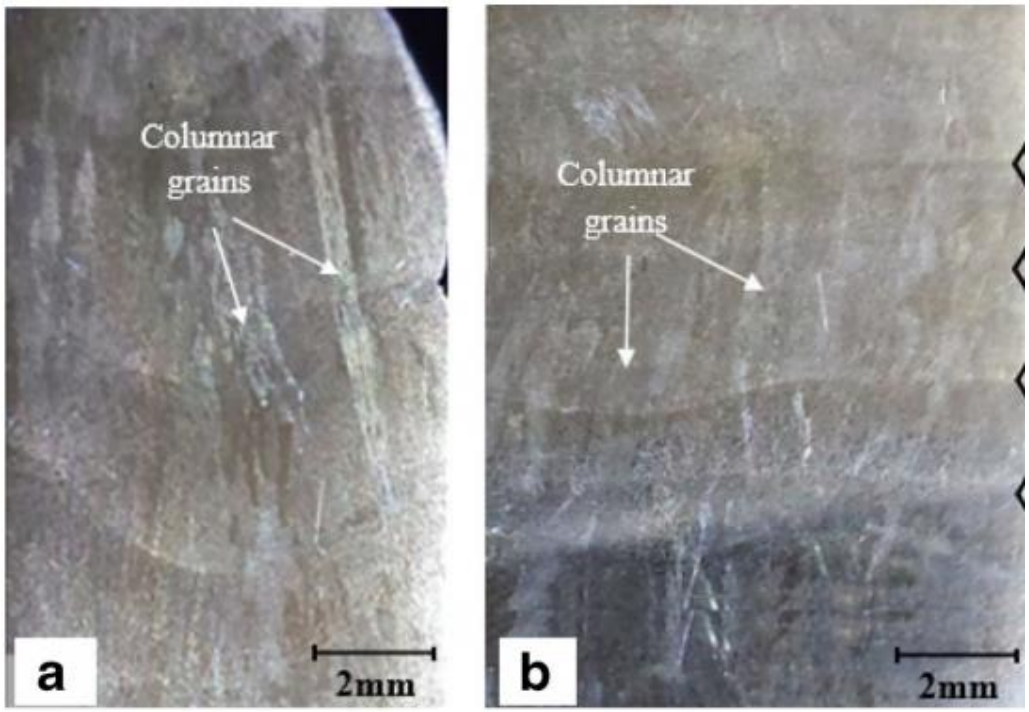

Figure 94. Macrographs from *Yilmaz and Ugla* [36] displaying columnar grain growth from a continuous gas-tungsten arc welding system on 308 SS.

Continuous mode PP3D samples did not display the vertical columnar grains seen in other continuous deposition modes using other welding methods. The lack of vertical columnar grains is not in complete agreement with the large, coarse features seen in the microstructure or with other works that deposited metals with similar methodology [35], [36]. Agreement with microstructure mechanics was reached when observed features on the continuous macroimages were generally very coarse, but grain growth was not oriented in a particular direction on most samples. One hypothesis to explain this occurrence is the orientation of the torches. The orientation kept consistent through all continuous samples was with arc 1 oriented to be heating the weld pool and metal slightly ahead of the weld pool relative to travel direction as seen in figure 90 below. In figure 90, the leading arc would have a preheating affect as the deposition occurred and kept the weld pool cooler, reducing the temperature gradient as compared to if travel direction was reversed. If reversed, it is hypothesized that arc 1 would add additional heat after deposition with possible further melting and allowing coarse grains to continue growth

between layers. If the trends seen in the macrostructures for the medium and low input powers remain after optimization of the PP3D system to deposit full 25 layers, investigation of the change in torch orientation relative to travel direction may yield differing results to those found in the current work.

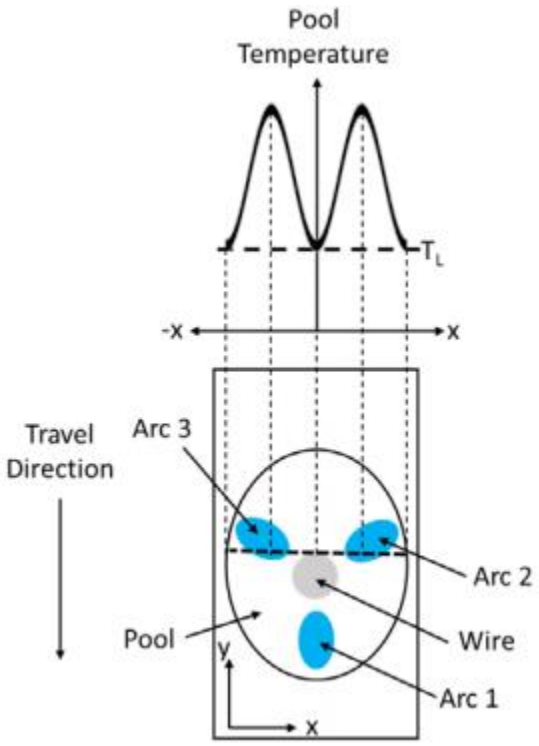

Figure 95. Torch orientation for the continuous deposition mode with arc 1 acting as a leading arc for the creation of the weld pool.

6.3. Fracture Surface Analysis

Samples examined for failure surface analysis were only available for the high and medium power input dabber mode. Discussion regarding results will focus on these power inputs, but the core theory is applicable for approximating failure surfaces of power input and deposition modes. Fracture in nearly all metals and especially FCC structure metals such as stainless steels are likely to exhibit some level of ductile fracture, otherwise known as plastic deformation before final fracture. Circumstances in which metals fail with very little to no plastic

deformation occurs when either the internal structure has extreme levels of internal defects or the physical properties have been manipulated to emulate those typically found in ceramics and glass [37]. These conditions are typically rare in an austenitic stainless steel unless specifically treated to induce these conditions [38].

Ductile fracture is considered the result of the growth of porosity via micro-voids internally during tension that initially stems from an internal defect such as pre-existing porosity in the sample, or an internal defect such as an inclusion. More micro-voids occur in multiple locations throughout a sample until the growth of these voids meet, causing coalescence of the voids that then rapidly lead to final fracture [37]. Initial porosity in the sample is typically a concern resulting from manufacturing methods such as in many powder metallurgy processes that must be optimized to not impede the manufactured piece's mechanical properties [7], [39], [40]. Internal defects are the most common cause of failure in both pure and mixed component systems, where the internal defect is typically a contaminants, an abundance of a brittle alloying agent (such as carbon in steels), or separation of grains within the structures [37].

In tensile testing of ductile materials such as many stainless steels, the crack initiation point(s) are less important than the zone where the coalescence of the voids begins as prior to that point, plastic deformation was occurring and if tension was removed, the plasticity of the material would act to help relieve some of the internal stresses due to the voids. On a stress-strain curve, this would be represented by the plateau region leading to the final fracture. During this plastic deformation in uniaxial tensile testing conditions, the voids tend to elongate in the parallel to the loading axis and shrink in the transverse loading direction, causing a phenomenon known as "necking" in the center of the tested sample [37].

Failure surface observed for the samples at high magnification showed high levels of micro-voids or “dimpling” on the failure surface samples, which correlates to ductile failure common for austenitic stainless steels and has been seen in previous works [41]. In areas examined, few defects relating to inclusions were found, but those that were found included iron carbides and oxides. The iron carbides are likely a result of the solidification conditions from the dabber mode that were too rapid for complete diffusion of the carbon into the grains, forcing an excess of iron to be found in a grain boundary. The oxide formation could be a result of an inconsistency of the welding process allowing oxygen into the weld pool, or a possible outside contaminant that could have made its way onto the surface if proper storage did not occur following testing.

Both the medium and high-power input dabber samples displayed limited necking in the samples and displayed a clear transition from the ductile behavior to an area of fast fracture as seen in figure 93. The area of fast fracture can be seen as the planar section on the left-hand side of the image with a red arrow highlighting the transition start. Areas prior to the fast fracture zone are areas of highly ductile behavior in the sample.

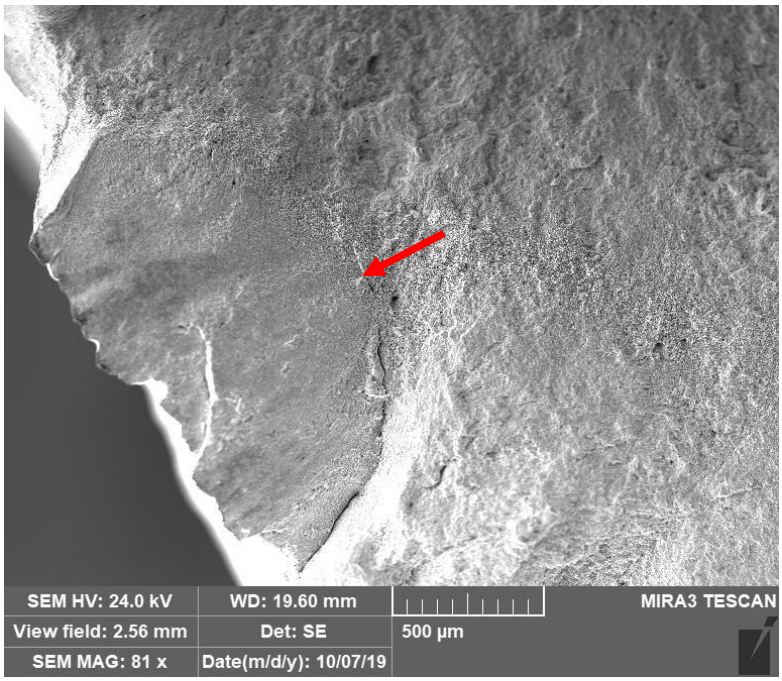

Figure 96. A tensile fracture sample with high levels of ductile failure leading into a shear face at the final fracture surface.

The failure surfaces of all the samples appear to have failed in a ductile fashion with relatively low occurrence of internal defects such as ferrite inclusions to cause the material to fail in a brittle fashion. In locations where defects were observed, the primary constituents of the inclusions were typically an iron carbide or oxides. The source of oxides could be a combination of solidification conditions or welding conditions allowing the presence of oxygen from the atmosphere to enter the weld pool and cause the formation of an oxide inclusion.

Examining behaviors seen in both the high and medium power input dabber samples, behavior can be speculated for the low dabber as well as the continuous deposition mode as a whole when considering hardness and microstructures mechanics. The low power input in terms of both microstructure features and hardness is very similar to both other power inputs for the dabber. The % difference between the average values seen in the hardness is at worst under 7%, indicating that while differences in strength and microstructure exist, the differences are unlikely to change the outcome of the fracture surface morphology. Barring high levels of inclusions

found in the weld structure, the low power input samples are predicted to display features very similar to the existing samples.

Results seen in the current work have high levels of agreement with previous works, especially when examining other austenitic stainless steels. Looking at the failure surface results from *Li et al.* [31] and *Chen et al.* [35], seen in figure 97 below, features from those works show nearly identical sets of features in both 308L and 316L SS. Both works show failure surfaces with elevated levels of dimpling throughout most of the surface, similar to features present in the current work,

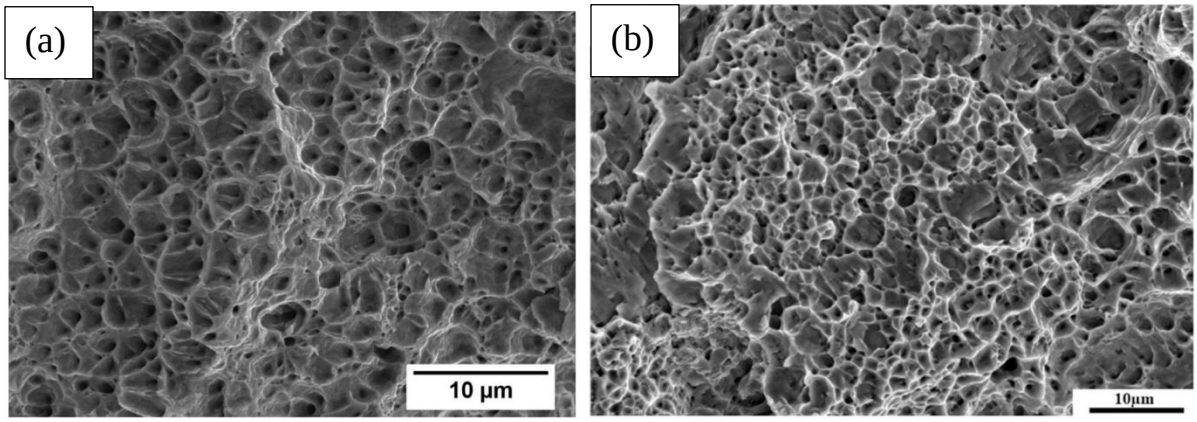

Figure 97. (a) Fracture morphology from *Li et al.* [31] displaying fracture morphology of a 308 SS produced as a multi-layer wire laser clad coating onto 316L SS and (b) Macrographs from *Chen et al.* [35] displaying fracture surface features such as dimpling from a very ductile failure on 316L SS.

The continuous samples registered a significant difference in their measured mechanical properties compared to the dabber samples. The sub-grain feature size is generally more coarse and as will be discussed further in the hardness testing section, the overall results of the continuous deposition mode indicate significantly harder samples are produced by the continuous deposition mode, having a hardness more in line with stainless steels that have undergone cold working or other mechanical strengthening processing [38]. As a result, more brittle fracture patterns are likely to emerge if the hardness data translates to a tensile specimen. Microstructure features indicate that despite hardness data, the primary failure mechanism is

likely to be ductile in nature. The features that indicate ductile fracture are large areas of austenite as the primary microstructure feature amongst the FA solidification. Austenite has an FCC crystal structure, which in many metals such as copper and aluminum indicate a more ductile metal overall [37].

6.4. Hardness Testing

Microhardness values of both the dabber and continuous had a high level of variability between testing sites, but the variance was especially high on the dabber mode samples with no consistent relationship between power input and hardness on either the YZ or XZ orientations. The variance on dabber mode deposition could be expected based on the results seen in the microstructure images as the morphology, orientation, and coarseness of the structures would vary immensely both between and in each layer

The continuous deposition microhardness samples experienced an inverse relationship with the microhardness and microstructure features that is similar to the relationship typically seen with in the Hall-Petch relationship where increasing grain feature size results in lower mechanical properties. The microhardness results of the continuous deposition samples decreased with decreasing power input while the average dendrite size between samples generally increased [42]. This relationship may exist when examining features individually as can be done through micro indentation, results of this nature can become problematic when applying a measurement that is measuring the bulk hardness of the material.

While the Hall-Petch relationship is generally referenced for interpreting the inverse relationship between grain size and mechanical properties whereas grain size decreases, strength of a material increases. However when working with sub-grain features, the features become too small and invalidates the relationship from a calculation standpoint [42]. Some work has been

done to modify the Hall-Petch equation to fit tensile testing data for samples such as those with nano-scale grain features, but this work requires large amounts of representative tensile data to begin forming substantial relationships [43].

All macrohardness results are reported in HRB despite all the continuous samples (with exception to the high-power input YZ sample) registering above the Rockwell B scale upper limit. This was done because direct conversion between Rockwell scales is empirical at best when the conversion ranges are compatible, so the alternative of keeping a consistent scale allows for comparisons to be made on at least an empirical level.

Macrohardness results for the dabber mode contrasts with the microhardness as it tended to contain less variance in the results. Rockwell hardness testing is a larger, bulk hardness testing method and is less susceptible to sensitivity as a result of small changes in microstructure when compared to microindentation [27], [28]. The primary pattern was that both the high and low power input samples had overall higher hardness in both orientations than the medium power input samples, but all dabber samples were within 10 HRB or less.

The continuous samples microhardness resulted in almost universally higher levels of hardness when compared to the dabber samples with almost every power input and orientation registering hardness levels at approximately 118-119 HRB with low levels of variation in the samples. The one exception is the continuous high-power input YZ orientation sample. That particular orientation had the lowest average hardness of all other samples, falling well into the range of the dabber mode samples. A second round of testing using a piece cut from the opposite end of the sample from the first yielded nearly identical results to the first round of testing. A possible explanation to this behavior might be due to a higher level of primary austenite forming at a macro level close to the weld pool edge in the high-power input. This would be a possible

result of the slower cooling seen in the full-sized high-power input continuous sample. Specific examination of the YZ orientation should be done in future work if the medium and low power inputs can produce stable 25-layer samples.

Finally, relating the hardness back to previous results, the hardness results are most useful when put into the context of the microstructure and fractographic results. Secondary dendrite spacing in a welding specimen can indicate average feature size, which when examining the growth direction of the subgrain features can be related to overall solidification patterns. Comparing the results of microstructure and hardness or other mechanical testing to results seen in well documented sources such as the ASTM standards or ASM handbook, can indicate how a process affected the end result of a produced sample.

Looking to the hardness values from the current work, the microindentation results and the entirety of the dabber macroindentation results are in relative agreement with typical hardness values seen for an austenitic stainless steel in the annealed condition. The macrohardness testing for majority of the continuous samples had hardness values that would be much closer to austenitic stainless steel that has undergone cold working or other processes that would increase strength.

7. Conclusions

Several key findings were made in the characterization of specimens produced by the PP3D technique. These finds are summarized below.

1. Dabber deposition mode overall resulted in very fine microstructure features with highly varied morphology and growth orientations, appearing to refine microstructure features at the sub-grain scale in all orientations. This is attributed to discreet, overlapping weld beads during deposition.
2. Dabber deposition mode in the macro scale still produced large, vertically oriented grain structures that could serve as points of structural weakness in fatigue loading. This is due to the long columnar grains having a common grain boundary that would act as the path of easiest fracture in mechanical testing.
3. Continuous mode produced a more conventional welding morphology at the sub-grain level with grain features that were highly consistent in morphology and directional orientation. These features are due to the steady-state welding conditions that occur during the continuous deposition mode.
4. At the macro scale, continuous deposition mode produced overall more coarse grain features that did not tend to have vertical orientations in the grain growth. The current hypothesis is the orientation the torches did not allow the weld pool to sufficiently melt previous layers to allow for coarse, columnar grains to grow across weld layers.
5. Fracture surfaces from the dabber mode samples appear to be highly ductile, with large interconnected dimple features that are strong indicators of a very ductile failure. This can be attributed to the significant amount of austenite's FCC crystal structure.
6. EDS scanning revealed the compositional makeup of the failure surface was within normal ranges for 304L stainless steel and had few contaminants.
7. Hardness testing revealed high levels of variability in the dabber deposition modes, especially with the microindentation as hardness between XZ and YZ orientations differ significantly on the high and medium input power. Similar to the variability in morphology, this can be attributed to the varied thermals experienced by discreet overlapping weld beads.
8. Continuous hardness testing was more consistent with a drop in hardness as the input power decreased for the microhardness that corresponds to the Hall-Petch relationship. Macrohardness revealed a more consistent level of hardness which is not in complete agreement with either the Hall-Petch relationship and microstructure feature sizes.

8. Recommendations for Future Work

The work presented previously is a microstructural examination of 308L SS specimens produced by the PP3D system, but further characterization that can apply to 308L and theoretically to other materials are listed below:

1. A full mechanical suite of tensile and fatigue testing for more 308L samples oriented vertically and transversely is recommended to test for anisotropy in the samples.
2. Following mechanical testing, samples should undergo fracture surface analysis to determine common failure modes and compare crack propagation methods between dabber and continuous modes
3. The continuous mode for 308L SS requires optimization to properly produce samples in the range of the medium and low power inputs as both samples did not have the full 25 layers whereas all dabber samples and the high-power input continuous had a complete 25 layers.

9. References Cited

[1] ASTM INTERNATIONAL, "ASTM F2792-12a," *Rapid Manuf. Assoc.*, pp. 1–3, 2013.

[2] B. Wu *et al.*, "Effects of heat accumulation on the arc characteristics and metal transfer behavior in Wire Arc Additive Manufacturing of Ti6Al4V," *J. Mater. Process. Technol.*, vol. 250, no. August, pp. 304–312, 2017.

[3] S. W. Williams, F. Martina, A. C. Addison, J. Ding, G. Pardal, and P. Colegrove, "Wire + Arc additive manufacturing," *Mater. Sci. Technol. (United Kingdom)*, vol. 32, no. 7, pp. 641–647, 2016.

[4] J. C. Lippold and W. F. Savage, "Solidification of Austenitic Stainless Steel Weldments : Part I — A Proposed Mechanism The distribution and morphology of delta ferrite is dependent," *Weld. Res. Suppl.*, no. December, pp. 362s-374s, 1979.

[5] J. C. Lippold and W. F. Savage, "Solidification of Austenitic Stainless Steel Weldments - 2. the Effect of Alloy Composition on Ferrite Morphology.," *Weld. J. (Miami, Fla)*, vol. 59, no. 2, 1980.

[6] J. C. Lippold and W. F. Savage, "Solidification of Austenitic Stainless Steel Weldments - 3. the Effect of Solidification Behavior on Hot Cracking Susceptibility.," *Weld. J. (Miami, Fla)*, vol. 61, no. 12, pp. 388–396, 1982.

[7] X. Shi *et al.*, "Selective laser melting-wire arc additive manufacturing hybrid fabrication of Ti-6Al-4V alloy: Microstructure and mechanical properties," *Mater. Sci. Eng. A*, vol. 684, no. November 2016, pp. 196–204, 2017.

[8] J. R. Hönnige, P. Colegrove, and S. Williams, "Improvement of microstructure and mechanical properties in Wire + Arc Additively Manufactured Ti-6Al-4V with Machine Hammer Peening," *Procedia Eng.*, vol. 216, no. 2017, pp. 8–17, 2017.

[9] S. Trigwell and G. Selvaduray, "Effects of welding on the passive oxide film of electropolished 316L stainless steel," *J. Mater. Process. Technol.*, vol. 166, no. 1, pp. 30–43, 2005.

[10] E. Brandl, B. Baufeld, C. Leyens, and R. Gault, "Additive manufactured Ti-6A1-4V using welding wire: Comparison of laser and arc beam deposition and evaluation with respect to aerospace material specifications," *Phys. Procedia*, vol. 5, no. PART 2, pp. 595–606, 2010.

[11] B. Baufeld, O. Van der Biest, and R. Gault, "Additive manufacturing of Ti-6Al-4V components by shaped metal deposition: Microstructure and mechanical properties," *Mater. Des.*, vol. 31, no. SUPPL. 1, pp. S106–S111, 2010.

[12] F. Martina, J. Mehnen, S. W. Williams, P. Colegrove, and F. Wang, "Investigation of the benefits of plasma deposition for the additive layer manufacture of Ti-6Al-4V," *J. Mater. Process. Technol.*, vol. 212, no. 6, pp. 1377–1386, 2012.

[13] J. J. Lin *et al.*, "Microstructural evolution and mechanical properties of Ti-6Al-4V wall deposited by pulsed plasma arc additive manufacturing," *Mater. Des.*, vol. 102, pp. 30–40, 2016.

[14] N. J. Huft, "INVESTIGATION OF MULTIPLE TORCH PAW-BASED ADDITIVE MANUFACTURING," Montana Technological University, 2019.

[15] R. W. Messler, *Principles of Welding*. 1999.

[16] Q. Wu *et al.*, "Obtaining uniform deposition with variable wire feeding direction during wire-feed additive manufacturing," *Mater. Manuf. Process.*, vol. 32, no. 16, pp. 1881–1886, 2017.

[17] J. Fu *et al.*, “Microstructure and mechanical properties of Ti-6Al-4V fabricated by verticalwire feeding with axisymmetric multi-laser source,” *Appl. Sci.*, vol. 7, no. 3, 2017.
[18] C. L. Jenney and A. O’Brien, “Welding Handbook_Volume 1_WELDING SCIENCE AND TECHNOLOGY,” *Am. Weld. Soc.*, vol. 1, p. 982, 1991.
[19] C. R. Cunningham, J. M. Flynn, A. Shokrani, V. Dhokia, and S. T. Newman, “Invited review article: Strategies and processes for high quality wire arc additive manufacturing,” *Addit. Manuf.*, vol. 22, no. June, pp. 672–686, 2018.
[20] S. Kou, *Welding Metallurgy*, vol. 2. 2003.
[21] S. Kou and Y. Le, “Effect of Quenching on the Solidification Structure and Transformation Behavior of Stainless Steel Welds.,” *Metall. Trans. A, Phys. Metall. Mater. Sci.*, vol. 13 A, no. 7, pp. 1141–1152, 1982.
[22] J. C. Lippold and D. J. Kotecki, *Welding Metallurgy and Weldability of Stainless Steel*. Hoboken, NJ: John Wiley & Sons, Inc., 2005.
[23] J. C. Lippold, “Solidification Behavior and Cracking Susceptibility of Pulsed-Laser Welds in Austenitic Stainless Steels,” *Weld. J. (Miami, Fla)*, vol. 73, no. 6, pp. 129s-139s, 1994.
[24] S. A. David, “Ferrite Morphology and Variations in Ferrite Content in Austenitic Stainless Steel Welds.,” *Weld. J. (Miami, Fla)*, vol. 60, no. 4, pp. 63–71, 1981.
[25] S. Katayama, T. Fujimoto, and A. Matsunawa, “Correlation among solidication process, microstructure,” vol. 14, no. 1, 1983.
[26] S. A. David and J. M. Vitek, “Correlation between solidification parameters and weld microstructures,” *Int. Metall. Rev.*, no. 20, pp. 80–105, 1975.
[27] “ASTM E384-16 Standard Test Method for Microindentation,” *Am. Soc. Test. Mater.*, 2016.
[28] G. Require- *et al.*, “ASTM E18 − 16 Standard Test Methods for Rockwell Hardness of Metallic Materials,” *Am. Soc. Test. Mater.*, no. X, pp. 1–38, 2016.
[29] Y. Feng, B. Zhan, J. He, and K. Wang, “The double-wire feed and plasma arc additive manufacturing process for deposition in Cr-Ni stainless steel,” *J. Mater. Process. Technol.*, vol. 259, no. August 2017, pp. 206–215, 2018.
[30] R. Unnikrishnan *et al.*, “Effect of heat input on the microstructure, residual stresses and corrosion resistance of 304L austenitic stainless steel weldments,” *Mater. Charact.*, no. 93, pp. 10–23, 2014.
[31] K. Li, D. Li, D. Liu, G. Pei, and L. Sun, “Microstructure evolution and mechanical properties of multiple-layer laser cladding coating of 308L stainless steel,” *Appl. Surf. Sci.*, vol. 340, pp. 143–150, 2015.
[32] P. K. Ghosh, S. G. Kulkarni, M. Kumar, and H. K. Dhiman, “Pulsed current GMAW for superior weld quality of austenitic steinless steel sheett,” *ISIJ Int.*, vol. 47, no. 1, pp. 138–145, 2007.
[33] S. Mereddy, M. J. Bermingham, D. H. StJohn, and M. S. Dargusch, “Grain refinement of wire arc additively manufactured titanium by the addition of silicon,” *J. Alloys Compd.*, vol. 695, pp. 2097–2103, 2017.
[34] A. R. Mcandrew *et al.*, “Interpass rolling of Ti-6Al-4V wire + arc additively manufactured features for microstructural refinement,” *Addit. Manuf.*, vol. 21, pp. 340–349, 2018.
[35] X. Chen, J. Li, X. Cheng, B. He, H. Wang, and Z. Huang, “Microstructure and mechanical properties of the austenitic stainless steel 316L fabricated by gas metal arc additive manufacturing,” *Mater. Sci. Eng. A*, vol. 703, no. January, pp. 567–577, 2017.
[36] O. Yilmaz and A. A. Ugla, “Microstructure characterization of SS308LSi components

manufactured by GTAW-based additive manufacturing: shaped metal deposition using pulsed current arc," *Int. J. Adv. Manuf. Technol.*, vol. 89, no. 1–4, pp. 13–25, 2017.
[37] N. P. Suh and A. Turner, "Fracture," in *Elements of the Mechanical Behavior of Materials*, Washington D.C.: McGraw Hill, 1975, pp. 408–455.
[38] R. S. D. Washko, C. Aggen, A. L. Steel, and A. Ludlum, "Wrought Stainless Steels," *Prop. Sel. Irons, Steels, High-Performance Alloy.*, pp. 841–907, 2018.
[39] M. Ma, Z. Wang, and X. Zeng, "A comparison on metallurgical behaviors of 316L stainless steel by selective laser melting and laser cladding deposition," *Mater. Sci. Eng. A*, vol. 685, no. October 2016, pp. 265–273, 2017.
[40] S. Keckler, "Material Properties of Laser Powder Bed Fusion Processed 316L Stainless Steel," 2018.
[41] T. Matsuo, J. Yamabe, and S. Matsuoka, "Effects of hydrogen on tensile properties and fracture surface morphologies of Type 316L stainless steel," *Int. J. Hydrogen Energy*, vol. 39, no. 7, pp. 3542–3551, 2014.
[42] "ASTM E112-13 Standard Test Methods for Determining Average Grain Size," *Am. Soc. Test. Mater.*, 2013.
[43] F. Yin *et al.*, "Ultrastrong nanocrystalline stainless steel and its Hall-Petch relationship in the nanoscale." pp. 26–31, 2018.

10. Appendix A: Dendrite Analysis Results Tables

Table III. Dabber High Power Input XZ Samples

Image #	Dendrites		Arms	
	Count	Length	Count	Spacing
4	8	603.637	60	10.061
7	11	948.023	159	5.962
8	12	1362.136	224	6.081
10	16	1027.695	186	5.525
24	20	1479.337	153	9.669
			Average:	7.4596

Table IV. High Power Input YZ Samples

Image #	Dendrites		Arms	
	Count	Length	Count	Spacing
1	35	1888.645	260	7.264
2	47	2143.067	441	4.86
5	19	968.471	199	4.867
6	15	1104.552	129	8.562
10	25	1719.121	139	12.368
11	20	988.911	76	13.012
13	12	830.659	63	13.185
25	18	1353.111	194	6.975
Sample 2				
9	32	2404.424	397	6.056
			Average:	8.572111

Table V. Dabber Medium Power Input XZ Samples

Image #	Dendrites		Arms	
	Count	Length	Count	Spacing
13	28	1921.487	247	7.779
18	16	1853.324	270	6.864
20	17	1458.588	158	9.232
36	10	819.593	97	8.449
			Average:	8.081

Table VI. Dabber Medium Power Input YZ Samples

Image #	Dendrites		Arms	
	Count	Length	Count	Spacing
1	16	1557.858	199	7.828
10	21	2278.572	306	7.446
15	21	2595.791	324	8.012
25	19	1546.526	233	6.637
30	19	1628.726	227	7.175
			Average:	7.4196

Table VII. Dabber Low Power Input XZ Samples

Image #	Dendrites		Arms	
	Count	Length	Count	Spacing
2	30	1868.448	266	7.024
5	19	3027.631	354	8.553
18	8	1065.557	170	6.268
21	16	1427.87	176	8.113
			Average:	7.4895

Table VIII. Dabber Low Power Input YZ Samples

Image #	Dendrites		Arms	
	Count	Length	Count	Spacing
3	10	1109.277	107	10.367
7	20	3549.182	347	10.228
9	38	5194.47	607	8.558
47	9	1488.544	132	11.277
			Average:	10.1075

Table IX. Continuous High Power Input XZ Samples

Image #	Dendrites		Arms	
	Count	Length	Count	Spacing
8	22	1604.87	216	7.43
14	12	1205.674	115	10.484
18	13	2101.355	211	9.959
Sample 2				
5	22	1931.566	350	5.519
6	18	1300.136	153	8.498
			Average:	8.378

Table X. Continuous High Power Input YZ Samples

Image #	Dendrites		Arms	
	Count	Length	Count	Spacing
1	20	1860.31	231	8.053
5	18	1935.826	193	10.03
16	18	1935.826	193	10.03
18	18	1935.826	193	10.03
			Average:	9.53575

Table XI. Continuous Medium Power Input XZ Samples

Image #	Dendrites		Arms	
	Count	Length	Count	Spacing
6	15	1336.78	155	8.624
9	16	1942.001	185	10.497
11	12	1227.481	121	10.144
24	16	1667.101	160	10.419
28	18	2093.525	212	9.875
			Average:	9.9118

Table XII. Continuous Medium Power Input YZ Samples

Image #	Dendrites		Arms	
	Count	Length	Count	Spacing
3	9	1410.637	158	8.928
16	13	1492.664	142	10.512
20	13	1492.664	142	10.512
22	11	1743.367	165	10.566
27	13	1180.909	105	11.247
			Average:	10.353

Table XIII. Continuous Low Power Input XZ Samples

Image #	Dendrites		Arms	
	Count	Length	Count	Spacing
1	15	1327.286	121	10.969
7	22	2288.599	207	11.056
14	16	1924.096	135	14.253
17	17	2040.126	179	11.397
23	10	1090.643	78	13.983
			Average:	12.3316

Table XIV. Continuous Low Power Input YZ Samples

Image #	Dendrites		Arms	
	Count	Length	Count	Spacing
1	16	1747.066	155	11.271
13	18	1998.287	148	13.502
16	15	2162.632	197	10.978
21	12	1311.17	128	10.244
			Average:	11.49875

11. Appendix B: Selected Fractography Images

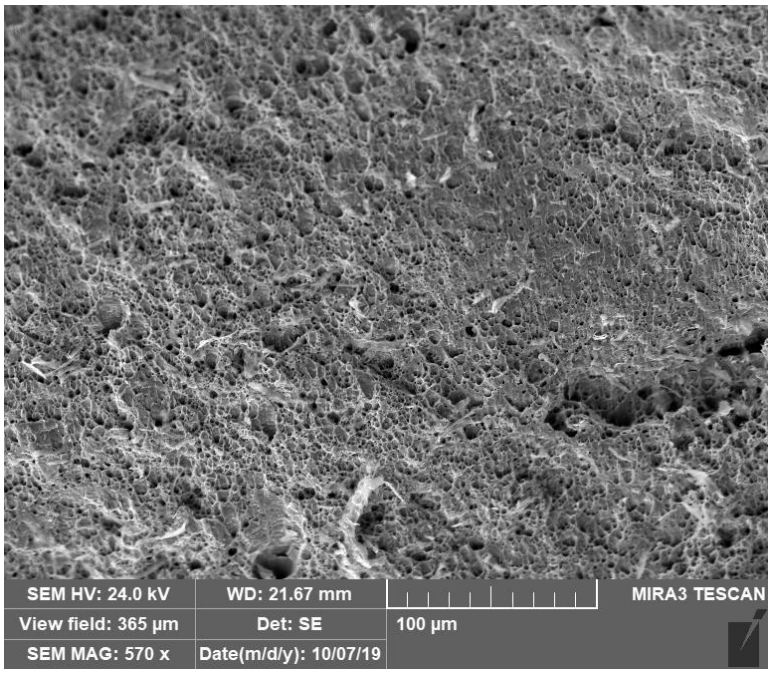

Figure 98. A tensile fracture sample with high levels of ductile failure denoted by dimpling features also known as "Honey-comb" type failure surfaces.

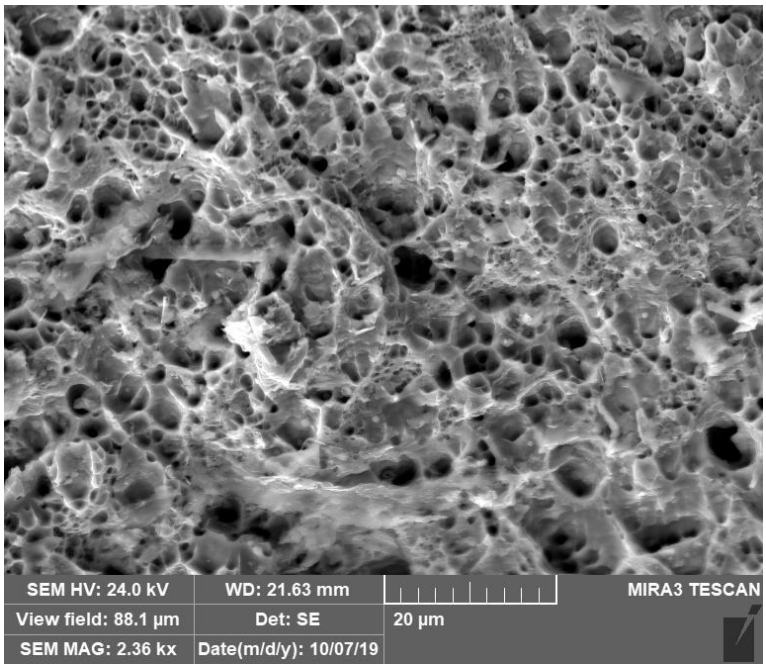

Figure 99. A tensile fracture sample with high levels of ductile failure denoted by dimpling features also known as "Honey-comb" type failure surfaces.

12. Appendix C: Hardness Testing Tables

Table XV. Average Microhardness Values for the Dabber Samples

Not Including Base Metal	High		Medium		Low	
	XZ	YZ	XZ	YZ	XZ	YZ
Average	168.5294	182.45	181.4933	170.7769	180.2412	182.3941
Standard Deviation	8.742376	9.345245	7.278687	14.05162	12.96198	8.7758
Relative Standard Deviation	5.19%	5.12%	4.01%	8.23%	7.19%	4.81%

Table XVI. Average Microhardness Values for the Continuous Samples

Not Including Base Metal	High		Medium		Low	
	XZ	YZ	XZ	YZ	XZ	YZ
Average	181.4154	195.945	180.2143	181.1286	172.1333	176.9333
Standard Deviation	10.48052	11.73292	7.325187	11.17442	6.735891	6.56252
Relative Standard Deviation	5.78%	5.99%	4.06%	6.17%	3.91%	3.71%

Table XVII. Average Macrohardness Values for the Dabber Samples

Not Including Base Metal	High		Medium		Low	
	XZ	YZ	XZ	YZ	XZ	YZ
Average Hardness (HRB)	92.35667	87.61438	85.57571	83.88455	88.08813	91.162308
Standard Deviation	5.179903	4.074233	2.473943	2.421121	4.245539	1.2036748
Coefficient of Variation	5.61%	4.65%	2.89%	2.89%	4.82%	1.32%

Table XVIII. Average Macrohardness Values for the Continuous Samples

Not Including Base Metal	High		Medium		Low	
	XZ	YZ	XZ	YZ	XZ	YZ
Average Hardness (HRB)	119.1422	82.99833	119.2422	118.8011	119.8209	118.445
Standard Deviation	4.319256	4.387964	2.08503	2.411539	2.539404	2.520269
Coefficient of Variation	3.63%	5.29%	1.75%	2.03%	2.12%	2.13%

SIGNATURE PAGE

This is to certify that the thesis prepared by Ryan Foley entitled "MICROSTUCTURAL ANALYSIS OF ADDITIVELY MANUFACTURED 308L STAINLESS STEEL PRODUCED BY PLASMA ARC WELDING" has been examined and approved for acceptance by the Department of Materials Science and Engineering, Montana Technological University, on this 13th day of December, 2019.

Sudhakar Vadiraja, PhD, Professor
Department of Metallurgical and Materials Engineering
Chair, Examination Committee

Bruce Madigan, PhD, Professor
Department of Mechanical Engineering
Member, Examination Committee

Brahmananda Pramanik, PhD, Assistant Professor
Department of Mechanical Engineering
Member, Examination Committee

Lee Richards, PhD, Assistant Professor
Department of Petroleum Engineering
Member, Examination Committee